OPTIMIZATION OF POLYMER CONJUGATION FOR INTERLEUKIN-1 RECEPTOR ANTAGONIST: EFFICIENCY, RESOLUTION, AND FUNCTIONAL ASSESSMENT

by

IŞILAY GÖKTAN

A Dissertation Submitted to the
Graduate School of Sciences and Engineering
in Partial Fulfillment of the Requirements for
the Degree of

Doctor of Philosophy

in

Chemical and Biological Engineering

KOÇ ÜNİVERSİTESİ

September 29, 2025

OPTIMIZATION OF POLYMER CONJUGATION FOR INTERLEUKIN-1 RECEPTOR ANTAGONIST: EFFICIENCY, RESOLUTION, AND FUNCTIONAL ASSESSMENT

Koç University

Graduate School of Sciences and Engineering

This is to certify that I have examined this copy of a doctoral dissertation by

IŞILAY GÖKTAN

and have found that it is complete and satisfactory in all respects,
and that any and all revisions required by the final
examining committee have been made.

Committee Members:

_____
Prof. Seda Kızılel (Advisor)

_____
Prof. Halil Kavaklı

_____
Assist. Prof. Hasan Demirci

_____
Prof. Ahmet Gül

_____
Assist. Prof. Tuğba Bal

Date: _____

To my family, for being my anchor throughout this journey.

ABSTRACT

This thesis builds a controlled, structure-guided comparison of PEGylation strategies for IL-1 receptor antagonist (IL-1Ra). Mapping accessible residues on IL-1Ra, thiol-selective (maleimide) versus lysine-directed (NHS) coupling strategies were evaluated across the same 5/10/20 kDa ladder at matched low stoichiometry, followed by a focused stoichiometry sweep for the preferred route. A near-native IL-1Ra backbone (M143V) was generated and ^{15}N-labeled for HSQC NMR so that structural integrity and the specific impact of PEGylation could be evaluated independently of the marketed sequence.

Across 5, 10, and 20 kDa, the thiol route gave a clean, predominantly di-PEG product, whereas lysine coupling produced heterogeneous mixtures across multiple sites and substitution levels. Increasing thiol stoichiometry above a low window reduced chromatographic separability without improving useful yield, identifying 10 kDa maleimide at low equivalents as a practical operating point. The M143V variant exhibited activity comparable to anakinra; ^{1}H–^{15}N HSQC of the 10 kDa thiol–PEG conjugate indicated preservation of a native-like fold with localized chemical-shift changes, and cell-based assays showed that PEGylation retained maximal inhibition while shifting the dose–response to higher concentrations. Together, the work delivers a reproducible analytical–structural–functional framework for selecting developable IL-1Ra conjugates, establishing a matched head-to-head design (chemistry × size × stoichiometry), and recommending thiol-selective 10 kDa PEG at low feed to obtain a clean di-adduct that purifies readily and preserves a native-like fold.

ÖZETÇE

Bu tez, IL-1 reseptör antagonisti (IL-1Ra) için PEGilasyon stratejilerini yapı temelli ve kontrollü bir karşılaştırma çerçevesinde ele almaktadır. IL-1Ra üzerindeki erişilebilir rezidüler haritalanarak, tiyol-seçici (maleimid) ve lizine yönelik (NHS) konjugasyon yaklaşımları, aynı 5, 10 ve 20 kDa PEG basamakları boyunca düşük stokiyometri koşullarında karşılaştırılmış; ardından tercih edilen yöntem için ayrıntılı bir stokiyometri taraması yürütülmüştür. Klinik diziden yalnızca tek amino asit farklılığı içeren bir IL-1Ra varyantı (M143V) üretilmiş, ^{15}N ile işaretlenmiş ve HSQC NMR analizleri için kullanılmıştır; böylece PEGilasyonun yapısal bütünlük üzerindeki etkisi incelenmiş ve klinikte kullanılan rekombinant IL-1Ra (anakinra) ile karşılaştırmalı olarak değerlendirilmiştir.

5, 10 ve 20 kDa koşullarında tiyol-hedefli yöntem, homojen ve yüksek verimle PEGile edilmiş ürünler verirken; lizin hedefli yöntem farklı PEGilasyon derecelerinde konjugatlar içeren heterojen karışımlar oluşturmuştur. Başlangıçta kullanılan düşük stokiyometri oranının ardından, tiyol konjugat verimini artırmak amacıyla PEG:protein oranı yükseltilmiş; ancak bu artış, hedef konjügat ürün miktarını arttırmamış ve konjügatların kromatografik ayrılabilirliğini azaltmıştır. Bu tablo, düşük stokiyometri aralığında 10 kDa mPEG-maleimid kullanımının rasyonel bir başlangıç seçimi olduğunu göstermiştir.

M143V varyantı, Anakinra ile karşılaştırılabilir biyolojik aktivite sergilemiş olup, ilgili $^{1}H–^{15}N$ HSQC spektrumu doğal IL-1Ra proteinine benzer katlanmanın korunduğunu doğrulamıştır. Yine M143V üzerinde gerçekleştirilen 10 kDa tiyol–PEG konjugatının $^{1}H–^{15}N$ HSQC spektrumunda ise PEGilasyon kaynaklı beklenen yerel kimyasal kayma değişimleri gözlemlenmiş, fakat genel katlanmasının korunduğu görülmüştür. Hücre temelli deneyler, PEGilasyonun maksimum inhibisyonu koruduğunu, ancak doz–yanıt eğrisini daha yüksek konsantrasyonlara kaydırdığını göstermiştir. Bütün olarak bu çalışma, IL-1Ra konjügat çalışmaları için, tekrarlanabilir bir analitik–yapısal–fonksiyonel model ile kimya × boyut × stokiyometri parametrelerini doğrudan karşılaştıran bir tasarım sunmaktadır.

ACKNOWLEDGEMENTS

I would like to express my deepest gratitude to my advisor, **Professor Seda Kızılel**, for her unwavering guidance, encouragement, and mentorship throughout my doctoral journey. Her invaluable insights, scientific expertise, and support have shaped not only this dissertation but also my growth as an independent researcher. Working under her supervision has been both an honor and a privilege.

I am also sincerely grateful to my committee members, **Professor İ. Halil Kavaklı, Assistant Professor Hasan Demirci,** and **Assistant Professor Tuğba Bal**, for their thoughtful input and support at key milestones of my graduate studies.

I am incredibly thankful to **Professor Ahmet Gül** for his leadership of the project and for providing valuable guidance and feedback at every stage.

My sincere thanks to **Dr. Çağdaş Dağ** for his helpful guidance in biophysical characterization.

I would also like to extend my appreciation to all members of the Kızılel Lab for their scientific discussions and friendship. I am especially indebted to **Dr. Esra Yalçın** and **Dr. Ayesha Gulzar** for their generous support—within and beyond the lab—and for the companionship with which we pushed one another forward through this demanding yet joyful journey.

I am deeply grateful to the **Baybalı family**, who so warmly welcomed me into their home during the most difficult times of my PhD journey, providing comfort and kindness when it was most needed.

To my dear friends, **Begüm Baybalı, Ece Eldem**, **İbrahim Akkan, Alara Zindancıoğlu, Naz Akyüzol,** and **Fırat Can Budak,** whose endless support, encouragement, and laughter have lightened the most challenging times, I am truly grateful. Their friendship has been a source of strength and joy, and I feel fortunate to have shared this journey with them.

This thesis would not have been possible without the financial support of **TÜBİTAK**, and I gratefully acknowledge funding through the flagship university–industry program 1004-20AG042. I also thank **Koç University, particularly KUTTAM** and **n²STAR,** for the resources and opportunities provided that have been essential in completing this work.

Finally, my deepest gratitude goes to my family. To my father, **Bahattin Göktan**, a psychologist, for thoughtful counsel that sharpened my research practice—from managing expectations to approaching problems systematically; to my mother, **Çiğdem Kıycı**, an educator, for her steady encouragement, kindness, and unwavering confidence in my work; and to my brother, **Atalay Göktan**, for constant support and for bringing balance and perspective. Their collective love and support have been integral to this thesis. Thank you for always being there for me.

TABLE OF CONTENTS

List of Tables

List of Figures

ABBREVIATIONS

4PL	Four-parameter logistic (model)
A	Anakinra
AP-1	Activator Protein 1
AUC	Area Under the Curve
BL21-AI	Escherichia coli strain BL21-AI
BME	β-mercaptoethanol
CD20	Cluster of Differentiation 20
CSP	Chemical Shift Perturbation
Cys	Cysteine
D_2O	Deuterium Oxide
DMEM	Dulbecco's Modified Eagle Medium
DMSO	Dimethyl Sulfoxide
DNA	Deoxyribonucleic Acid
DoP	Degree of PEGylation
DTT	DL-dithiothreitol
E	Elution
EC	Effective Concentration (e.g., EC_{50})
FDA	Food and Drug Administration
FMF	Familial Mediterranean Fever
FPLC	Fast Protein Liquid Chromatography
FT	Flow-through
HA	Hyaluronic Acid
HEK	Human Embryonic Kidney
HER2	Human Epidermal Growth Factor Receptor 2 (ERBB2)
HES	Hydroxyethyl Starch
His	Histidine
HSQC	Heteronuclear Single Quantum Coherence
IBD	Inflammatory Bowel Disease
IC	Inhibitory Concentration (e.g., IC_{50})
IL-1β	Interleukin-1 Beta
IL-1R1	Interleukin-1 Receptor Type 1
IL-1Ra	Interleukin-1 Receptor Antagonist
IL-1RAcP	Interleukin-1 Receptor Accessory Protein
IMAC	Immobilized Metal Affinity Chromatography
koff	Dissociation rate constant
kon	Association rate constant
L	Load
Lys	Lysine
mal	Maleimide
MALS	Multi-Angle Light Scattering
MEFV	Mediterranean Fever gene
MS	Mass Spectrometry

MTT	3-(4,5-Dimethylthiazol-2-yl)-2,5-Diphenyltetrazolium Bromide (assay)
N	Nonspecific
NaCl	Sodium Chloride
NF-κB	Nuclear Factor kappa-light-chain-enhancer of activated B cells
NHS	N-hydroxysuccinimide
NMR	Nuclear Magnetic Resonance
OD	Optical Density
PAE	Predicted Aligned Error
PAS	Proline–Alanine–Serine peptide polymer (PASylation)
PBAD	Arabinose-inducible PBAD promoter
PDB	Protein Data Bank
pDEST14	Gateway destination vector pDEST14
PEG	Poly(ethylene glycol)
PES	Polyethersulfone
PK	Pharmacokinetic
pLDDT	predicted Local-Distance Difference Test
RA	Rheumatoid Arthritis
SDS-PAGE	Sodium Dodecyl Sulfate–Polyacrylamide Gel Electrophoresis
SEAP	Secreted Embryonic Alkaline Phosphatase
SEC	Size Exclusion Chromatography
SVA	succinimidyl valerate
T	Thiol
T2D	Type 2 Diabetes
TNF	Tumor Necrosis Factor
XTEN	Unstructured hydrophilic polypeptide tag (XTEN)

Figure sample codes

- **N5-0.5** — Example of figure shorthand: “N” denotes Nonspecific PEGylation, the number indicates PEG molecular weight in kDa (here, 5 kDa), and the trailing value indicates the protein-to-PEG molar ratio (here, 0.5:1).
- **T10-3.0**— Example of figure shorthand: “T” denotes thiol-PEGylated, the number indicates PEG molecular weight in kDa (here, 10 kDa), and the trailing value indicates the protein-to-PEG molar ratio (here, 6:2, i.e.: **3.0**).

1. INTRODUCTION

Proteins are among the most versatile and functionally diverse macromolecules in biology, performing important roles such as catalyzing biochemical reactions, mediating signal transduction, transporting molecules, providing structural support, and acting as receptors in cellular communication[1,2]. Owing to their remarkable functional diversity, proteins present exceptional opportunities for therapeutic intervention across a broad spectrum of diseases[2].

When developed as therapeutics, proteins can restore or replace deficient or malfunctioning endogenous counterparts, modulate specific signaling pathways, neutralize pathogenic targets, or provide structural or enzymatic functions to reestablish normal physiology[1-3]. Their inherent molecular specificity allows them to act with minimal off-target effects, and their intricate three-dimensional structures allow them to perform complex biological tasks that are difficult to replicate with simpler molecular entities, such as small-molecule drugs[3]. As a result, more than 200 protein- or peptide-based therapeutics have been approved by the United States Food and Drug Administration (FDA), with many more in clinical development[4].

Despite these advantages, their clinical translation can often be hindered by inherent limitations in pharmacokinetics and stability. Many proteins are susceptible to chemical and physical degradation, such as oxidation, deamidation, unfolding, and aggregation, which can compromise potency and safety[5]. Furthermore, their large size, structural complexity, and hydrophilicity limit membrane permeability[2], while their susceptibility to proteolysis can accelerate clearance. These vulnerabilities necessitate careful design of both the molecule and its formulation to maintain therapeutic integrity throughout manufacturing, storage, and *in vivo* delivery[6]. Addressing these challenges is essential for enhancing therapeutic efficacy, improving patient compliance, and expanding the clinical potential of this important class of drugs — a central focus of the research presented in this thesis.

A central limitation in therapeutic proteins is their short circulation time. Proteins with molecular weights below the renal filtration threshold (~60–70 kDa) are rapidly removed from the bloodstream through glomerular filtration, ranging from minutes to hours. Even larger proteins can experience accelerated clearance through receptor-mediated endocytosis or proteolytic degradation. This rapid elimination frequently necessitates high or frequent dosing, increasing treatment burden and cost. As a result, a major focus

in biologics development is on engineering strategies to extend plasma half-life while maintaining bioactivity. These approaches — including PEGylation, Fc- or albumin-fusion, glycoengineering, lipidation, and alternative polymer conjugation — aim to minimize clearance, enhance stability, and reduce dosing frequency, ultimately broadening the therapeutic potential of protein drugs.

PEGylation, the covalent attachment of polyethylene glycol (PEG) to therapeutic proteins, is widely used to enhance pharmacokinetics, stability, and therapeutic efficacy[7,8]. This conjugation optimizes protein properties by **reducing immunogenicity, shielding antigenic epitopes, and preventing degradation by proteolytic enzymes**, thereby **prolonging circulation time and improving bioavailability**[7,9]. PEGylation also **reduces recognition by the reticuloendothelial system**, allowing the protein to remain in systemic circulation for an **extended period**, which is particularly beneficial for biologics with **short half-lives**[9].

One of the key advantages of PEGylation is its ability to **expand the hydrodynamic size** of a protein, which **decreases renal filtration** and modifies its distribution within the body[10,11]. The extent of these effects is determined by various factors, including the **number of PEG chains attached**[12], the **molecular weight**[13] **and structural properties of PEG**[11], the **specific site of conjugation on the protein**[12], and the **chemical strategy used for PEGylation**[11]. These elements collectively influence the pharmacokinetic behavior and biological activity of the PEGylated conjugate. Additionally, PEG forms a **hydration shell** around the protein, effectively **reducing protein aggregation**[11] **and increasing solubility**[14], a crucial advantage for biologics prone to misfolding or precipitation. Despite these advantages, **achieving optimal PEGylation efficiency while maintaining protein function remains a challenge**. Early PEGylation strategies relied **on random lysine conjugation**, often leading to **heterogeneous mixtures with variable bioactivity**[15-17]. Advances in **site-specific PEGylation** allow for **precise control over PEG attachment**, leading to better-defined pharmacokinetics, increased therapeutic consistency, and improved bioactivity[17].

Given the critical role of PEGylation in biopharmaceutical development, this study systematically examines the efficiency and structural effects of **two distinct PEGylation chemistries—mPEG-mal (cysteine-specific) and mPEG-SVA (lysine-based)**—on **interleukin-1 receptor antagonist (IL-1Ra)**, a therapeutic protein used to inhibit IL-1 signaling. The IL-1Ra variant studied here contains an M143V substitution, though this mutation does not alter the primary PEGylation sites. Due to its **short half-life** and **rapid**

renal clearance, PEGylation is investigated as a strategy to enhance its pharmacokinetic properties. PEGylation occurs at **naturally available cysteine and lysine residues**, with **maleimide** chemistry selectively targeting **thiols** and **succinimidyl ester** chemistry reacting with **primary amines**. By employing **2D NMR** to map conjugation sites alongside **SEC, SDS-PAGE, and mass spectrometry** to assess PEGylation efficiency, this study provides mechanistic insights into how different PEGylation chemistries influence **IL-1Ra structure and function**, ultimately guiding the rational design of next-generation PEGylated therapeutics[7,9,11].

2. LITERATURE REVIEW

2.1. Therapeutic Proteins: Introduction and Historical Overview

The introduction of protein-based therapeutics marks a significant advancement in modern medicine, offering targeted, biologically active agents for the treatment of a wide range of diseases. The therapeutic use of proteins began in earnest with the clinical application of insulin in the 1920s, a treatment that laid the foundation for future protein drugs by demonstrating the potential of biological macromolecules to replace or modulate endogenous proteins involved in disease pathways[18]. This early success was further amplified by the advent of recombinant DNA technology in the 1970s, which enabled the large-scale, controlled production of human proteins in microbial hosts. A major milestone was reached in 1982 when the U.S. FDA approved recombinant human insulin produced in E. coli, the first genetically engineered protein drug approved for clinical use[2,19].

Since then, the field has expanded rapidly. More than 200 therapeutic proteins have been approved by the FDA[18], and many others are currently in clinical development. These include a wide array of biologics, such as monoclonal antibodies, cytokines, clotting factors, enzymes, and fusion proteins. These proteins serve diverse roles, including replacement therapies (e.g., insulin, growth hormone), immune modulation (e.g., TNF-α inhibitors), and targeted oncological therapies (e.g., monoclonal antibodies against HER2 or CD20)[6,20].

Therapeutic proteins possess unique advantages over small-molecule drugs, including high specificity, reduced off-target effects, and the ability to engage complex biological pathways with high affinity[2]. Their endogenous origin also tends to result in lower immunogenicity compared to non-biological therapeutics. Furthermore, protein drugs are now being explored for tissue regeneration and wound healing, where their ability to provide biochemical cues and interact with extracellular matrices is unmatched[21,22].

Despite these benefits, early therapeutic proteins faced major limitations in terms of stability, immunogenicity, and manufacturing scalability. However, the emergence of protein engineering, fermentation optimization, and advanced purification techniques—combined with strategies like PEGylation and controlled drug delivery systems—has mitigated many of these issues and enabled the continued expansion of therapeutic proteins in clinical medicine[23].

2.2. Pharmacokinetic Limitations of Protein-Based Therapeutics

Despite their high specificity and broad therapeutic potential, protein-based drugs suffer from significant pharmacokinetic and physicochemical limitations that restrict their clinical efficacy and dosing convenience. One of the primary challenges is their short plasma half-life, which arises from several clearance mechanisms intrinsic to protein structure and host physiology[8,24]. Unmodified proteins are rapidly eliminated from the circulation through renal filtration, hepatic metabolism, and proteolytic degradation, especially for molecules below the glomerular filtration threshold (~60 kDa)[11,25]. This rapid clearance necessitates frequent dosing to maintain therapeutic levels, which is not only burdensome for patients but also increases the risk of adverse effects due to fluctuating peak concentrations[26].

Beyond rapid elimination, protein therapeutics are often susceptible to instability in biological environments. Many protein drugs exhibit limited conformational stability, leading to aggregation, denaturation, or precipitation under physiological conditions[27]. Aggregation, in particular, is a significant concern as it not only reduces therapeutic potency but can also enhance immunogenicity, potentially eliciting neutralizing antibodies or hypersensitivity reactions[28]. Factors such as pH, ionic strength, temperature fluctuations, mechanical agitation during storage or transport, and repeated freeze–thaw cycles all contribute to such degradation pathways[5].

Furthermore, proteins and peptides are subject to proteolytic degradation by endogenous enzymes such as peptidases and proteases present in the blood, liver, or cellular compartments[29]. This degradation compromises therapeutic bioavailability and complicates the prediction of dose–response relationships. In many cases, proteolytic sensitivity correlates with specific amino acid sequences or regions of intrinsic disorder, underscoring the importance of protein engineering to enhance resistance without altering function.

Together, these pharmacokinetic and biochemical limitations underscore the need for robust strategies to improve the stability, circulation time, and immune compatibility of protein therapeutics. While numerous chemical and genetic approaches have been developed to overcome these challenges, understanding the root causes of instability and rapid clearance remains a crucial first step in the rational design of next-generation biologics.

2.3. Strategies for Half-Life Extension in Biopharmaceuticals

Despite their excellent therapeutic potential, protein-based drugs are often limited by significant pharmacokinetic drawbacks, most notably their rapid clearance from systemic circulation. As previously discussed, short plasma half-life, enzymatic degradation, and renal filtration contribute to the need for frequent dosing, which can lead to reduced patient adherence, increased treatment burden, and unwanted side effects due to peak-and-trough fluctuations in drug concentration. These issues highlight a major gap between the biological efficacy of therapeutic proteins and their clinical practicality.

Numerous half-life extension techniques have been developed in response to these limitations in order to enhance the pharmacological characteristics of protein drugs. These strategies aim to decrease immunogenicity, increase circulation time, improve *in vivo* stability, and ultimately enhance therapeutic results. Through formulation-based, chemical, and genetic modifications, long-acting biologics can now be rationally designed owing to developments in protein engineering and bioconjugation technology over the past few decades.

2.3.1. Site-directed Mutagenesis

Site-directed mutagenesis is a widely used strategy to improve the pharmacokinetic properties of protein therapeutics by introducing targeted amino acid substitutions. These engineered modifications can enhance protein solubility, reduce aggregation, and increase stability in circulation, which leads to enhanced half-life [30].

Using this approach, different insulin variants were developed with different kinetics of action, where specific mutations adjust the isoelectric point or reduce self-association, resulting in the modulation of the absorption rates and prolonging action [31]. Similar principles apply to other therapeutic proteins, where substitution of reactive residues, such as free cysteines, with more stable amino acids like serine has been shown to lower degradation and increase the shelf life and bioavailability [32,33]. This tactic has been employed in clinically approved biologics such as aldesleukin [33] and interferon β1b [32,34].

2.3.2. Fc-Fusion Proteins

Fc-fusion proteins represent one of the most successful approaches developed for prolonging the half-life of biologically active peptides and proteins. This approach involves genetically linking the Fc region of an immunoglobulin (typically human IgG1 or IgG4) to a therapeutic protein or peptide, forming a single recombinant molecule with favorable pharmacokinetic properties. The Fc portion confers extended plasma half-life

primarily through two mechanisms: (i) increased molecular size that reduces renal clearance, and (ii) interaction with the neonatal Fc receptor (FcRn), which facilitates endosomal recycling and prevents lysosomal degradation.

The historical roots of Fc-fusion date back to the late 1980s when Dr. Daniel J. Capon first described an "immunoadhesin" composed of the extracellular region of CD4 fused to the Fc domain of an IgG antibody, designed to block HIV entry by binding the viral envelope protein gp120[35]. By fusing the Fc domain to the CD4 receptor ectodomain, the resulting construct benefited from improved solubility, enhanced avidity due to Fc dimerization, higher expression yields in mammalian systems, and easier purification. Importantly, the fusion also led to a longer pharmacokinetic profile in rodents compared to the standalone CD4 fragment. Since then, the concept has evolved dramatically, leading to the development of more than 50 Fc-fusion constructs, with at least 17 FDA-approved drugs currently on the market[36].

One of the earliest and most impactful examples of Fc-fusion therapeutics is etanercept (Enbrel®), which combines the extracellular domain of the TNF-α receptor with the Fc region of IgG1[37]. Approved in the late 1990s for rheumatoid arthritis, etanercept demonstrated the clinical potential of Fc fusion proteins and paved the way for subsequent biologics. Although it shares structural features with full-length antibodies, etanercept displays a notably shorter half-life. This difference has been linked to suboptimal binding to the neonatal Fc receptor (FcRn), a key player in prolonging antibody circulation through endosomal recycling[38]. Factors such as altered FcRn-binding site conformation or interference from target engagement may contribute to this reduced recycling efficiency, ultimately limiting the duration of systemic exposure compared to conventional IgG1 antibodies[39].

2.3.3. Albumin Fusion and Conjugation

Albumin fusion represents another strategy for extending the half-life of therapeutic proteins. Human serum albumin (HSA), due to its large size and natural recycling via the neonatal Fc receptor (FcRn), exhibits a long plasma half-life (~19 days) and can be genetically or chemically fused to biologics to improve their pharmacokinetics[36,40]. One of the earliest clinical successes was albiglutide, a GLP-1 analogue fused to albumin, which allowed once-weekly dosing for type 2 diabetes[41,42]. However, despite initial promise, it was later withdrawn due to safety concerns and commercial competition. A more successful example is albutrepenonacog alfa (Idelvion®), an albumin-FIX fusion

used in hemophilia B, which significantly extends clotting factor half-life[43].Despite these successes, albumin fusion technology has seen limited clinical translation. Challenges include manufacturing complexity (due to HSA's disulfide-rich structure), loss of bioactivity from steric hindrance, and competition with endogenous albumin for FcRn binding[36].

2.3.4. Polymer-based Conjugation Strategies

2.3.4.1. HESylation

HESylation is a polysaccharide-based strategy for prolonging the circulation half-life of therapeutic proteins through covalent attachment of hydroxyethyl starch (HES), a semi-synthetic derivative of the plant-based polymer amylopectin[44]. To reduce degradation by α-amylase, HES is chemically modified with hydroxyethyl side chains, allowing for increased *in vivo* stability. Conjugation can be achieved through chemical means or enzymatically via bacterial transglutaminase[45]. The resulting hydrophilic shell increases the hydrodynamic radius of the protein and reduces renal clearance—similar to the effects achieved by PEGylation.

Preclinical studies in rodents and rabbits have demonstrated extended half-lives for HESylated biopharmaceuticals such as EPO, IFNα2b, and IL-1Ra[46,47]. Notably, conjugation of IL-1Ra with 85 kDa HES led to a six-fold increase in plasma half-life in rats compared to the unmodified protein, and its hydrodynamic radius was comparable to that of 40 kDa branched PEG. Formulation studies also reported favorable properties for HESylated proteins, including lower viscosity and improved lyophilization behavior compared to PEGylated equivalents[48,49].

Despite these early advantages, enthusiasm for HESylation has waned due to safety concerns stemming from its prior use as a plasma volume expander[50]. Observations of HES accumulation in Kupffer cells and hepatocytes raised toxicological flags, complicating regulatory approval[51]. Additionally, the inherent heterogeneity of starch-derived polymers introduces complexity in synthesis and challenges in ensuring batch-to-batch consistency. While HESylation remains a biodegradable alternative to PEG, its clinical translation has been limited, and PEGylation continues to dominate among approved bioconjugation strategies.

2.3.4.2. Hyaluronic Acid (HA) Conjugation (HAylation)

Hyaluronic acid (HA), a naturally occurring linear polysaccharide composed of repeating disaccharide units, has been investigated as an alternative polymer for therapeutic protein modification. Owing to its biocompatibility, non-immunogenic character, and

biodegradability, HA conjugation—often termed HAylation—has attracted interest for modulating the pharmacokinetic behavior of biologics[52]. HA spans a broad molecular-weight range in native form (up to ~10 MDa), while polymers in the ~100–300 kDa window are typically preferred for conjugation to avoid viscosity and handling issues; this tunability can mimic some of PEG's hydrodynamic volume expansion while retaining the possibility of enzymatic clearance[53].

In the context of half-life extension, HA conjugation can reduce renal filtration and alter biodistribution by increasing hydrodynamic radius and forming a protective hydration environment around the conjugate; however, *in vivo* HA is subject to regulated enzymatic degradation by hyaluronidases and receptor-mediated uptake (e.g., via CD44, RHAMM, and LYVE-1), which distinguishes its fate from the relatively "stealth" behavior of PEG[53]. For illustrative contrast, Elder et al. reported that increasing PEG size (2 → 10 → 30 kDa) progressively reduced the affinity of a TNF-α-binding peptide—consistent with epitope shrouding—whereas conjugation to ~66 kDa HA preserved binding, and a short PEG linker on HA further enhanced the association rate, underscoring distinct structure–function trade-offs between PEGylation and HAylation[54].

Despite these advantages, several limitations differentiate HAylation from PEGylation for systemic exposure. First, HA's biological turnover can be a liability for long plasma residence: HA is actively degraded by hyaluronidases and internalized via HA receptors, processes that can be valuable for targeted delivery but that also promote tissue uptake and systemic clearance, making PEG-like "stealth" exposure harder to achieve without additional design layers (e.g., higher-MW HA, shielding, or hybrid constructs)[55,56]. Second, commonly used HA–protein coupling chemistries are prone to unintended cross-linking and product heterogeneity, complicating scale-up relative to many PEGylation workflows[52]. By comparison, PEG's synthetic, non-biorecognized chains reliably extend circulation through hydration-shell-mediated hydrodynamic shielding[57], reducing renal filtration and proteolysis across many protein classes—explaining why PEGylation remains the benchmark for systemic half-life extension even as HA offers biodegradability and receptor addressability that can be advantageous for localized or targeted delivery.

2.3.4.3. Polysialylation

Polysialylation (attachment of polysialic acid, PSA) employs colominic acid (CA)—the linear α-2,8-linked homopolymer of Neu5Ac—as the human-relevant variant of the sialic-acid family (which comprises Neu5Ac, Neu5Gc, and Kdn)[58]. Mechanistically, PSA

increases hydrodynamic volume and thereby reduces renal filtration[52,59,60]. Its permanent negative charge may further impede glomerular passage by electrostatic repulsion, and surface shielding can lessen proteolysis and antibody recognition[61]. Even though CA is biodegradable to Neu5Ac and is often described as low-immunogenic, in comparison to PEG, the immunological evidence base for PSA is relatively limited[59]. Reports of polymer-induced hypersensitivity in alternative polymers underscore that the immunogenicity of PSA conjugates cannot be excluded and necessitates further investigation[62].

2.3.4.4. PASylation

The PASylation strategy extends the circulation time of the protein by attaching an unstructured Pro/Ala/Ser (PAS) polypeptide to the therapeutic, which enlarges the hydrodynamic size and slows renal clearance[63]. Although half-life gains have been reported across several scaffolds (e.g., Fab fragments, IFN-α2b, hGH), the same unstructured, highly hydrated chains can complicate developability. In particular, PASylated proteins have been reported to show an increased tendency to aggregate, which raises practical concerns for manufacturing, storage, and long-term stability[64]. Because aggregates can heighten immunogenic risk, PAS constructs typically require tighter monitoring of colloidal stability and stress conditions than their unmodified counterparts[64]. Most PASylated candidates remain at preclinical or early clinical stages. Reported exposure increases span a wide range (from a few-fold to ~order-of-magnitude shifts), but outcomes are sequence- and length-dependent, and large PAS appendages can also impact viscosity or target engagement in ways that need case-by-case optimization[6,65].

2.3.4.5. XTENylation

XTENylation uses an unstructured, genetically encoded polypeptide (XTEN) composed only of Ala, Asp, Gly, Pro, Ser, and Thr to increase the hydrodynamic size of proteins and thereby reduce renal filtration, analogous in principle to other polymer–fusion strategies[66]. XTEN was developed as a recombinant, nonrepetitive sequence and has also been supplied in chemically reactive variants for conjugation, providing some flexibility in placement and chain length for pharmacokinetic tuning[52].

Evidence for half-life extension is established at the preclinical level (e.g., XTEN–exenatide increased terminal half-life in primates from ~0.5 h to ~60 h) and through program disclosures for several XTEN-modified therapeutics[66]. Nonetheless, clinical maturation has been limited relative to PEG. Notably, the XTEN-fused rhGH

somavaratan (VRS-317) failed to demonstrate non-inferiority to daily rhGH in the pediatric Phase 3 VELOCITY trial, and associated studies were subsequently terminated[67,68].

2.3.5. PEGylation

PEGylation—the covalent attachment of polyethylene glycol (PEG) to therapeutic proteins—originated with the seminal 1970s work of Davis and Abuchowski[69] showing that methoxy-PEG conjugation to model enzymes reduced immunogenicity and prolonged circulation, a concept that led to the first FDA-approved PEGylated enzymes (pegademase, 1990[70]; pegaspargase, 1994[71]). Mechanistically, PEG increases hydrodynamic volume to slow renal filtration while providing steric shielding that can lessen proteolysis[72] and antigen recognition[73]. As a result, PEGylation has become a cornerstone technology for extending systemic half-life across diverse biologic classes.

Employing PEGylation, the renal clearance of proteins is primarily reduced due to increased hydrodynamic size. This effect is specifically beneficial for therapeutic proteins that are typically rapidly cleared from circulation, such as enzymes, cytokines, peptide hormones, and antibody fragments (Fabs)[36]. Studies have demonstrated that PEGylated proteins can exhibit plasma half-lives that are significantly longer than their non-PEGylated counterparts, with some reports indicating increases of up to 20-fold[74]. This extended half-life allows for less frequent dosage applications, which can improve patient compliance and overall therapeutic outcomes[70,71].

Building on these pharmacokinetic gains, PEGylation also improves biophysical stability through steric shielding[75] and a hydration shell that can diminish protease access and self-association, thereby supporting activity retention for labile proteins and enabling robust injectable formulations[54,62]. Mechanistically, PEG is uncharged and strongly hydrophilic; its principal mode of action is enlargement of hydrodynamic volume (rather than charge effects), with the hydrated layer at the conjugate surface contributing to reduced interactions[62].

The immunogenicity of therapeutic proteins is another critical factor that can be attenuated at the protein level through epitope masking by PEG; however, contemporary evidence shows that anti-PEG antibodies (IgM/IgG/IgE) can arise (pre-existing or treatment-induced), accelerating clearance and contributing to hypersensitivity in some contexts[36,76,77]. Hence, PEGylation reduces antigenicity but does *not* universally minimize immunogenicity.

Despite these concerns, PEGylation remains a clinically validated modality: dozens of PEGylated medicines are approved and in routine use worldwide, reflecting consistent benefit–risk across indications[78]. For example, once-per-cycle pegfilgrastim is as effective as (and in some studies superior to) daily filgrastim in reducing chemotherapy-induced neutropenia, thereby enabling materially reduced dosing burden[79,80]. Certolizumab pegol demonstrates robust randomized-trial efficacy in rheumatoid arthritis[81,82], and pegaspargase maintains prolonged asparaginase activity with favorable treatment completion versus native enzyme—illustrating durable clinical utility despite ADA management needs[83]. Finally, recent reviews note that dozens of PEGylated medicines are approved worldwide and in routine use. Current practice focuses on assessing and mitigating anti-PEG risks (e.g., dedicated ADA assays) rather than abandoning PEGylation[84-86].

2.3.5.1. Non-specific PEGylation: Challenges and Limitations

Non-specific PEGylation (NSP) is a bioconjugation strategy that involves the covalent attachment of PEG to the ε-amino groups of lysine residues on proteins[69,87]. The choice of lysines is primarily due to their abundance in most proteins and their nucleophilic nature[88], which makes them reactive toward amine-selective PEG derivatives[87,89,90] (e.g., NHS esters, succinimidyl carbonates). This reaction can be achieved through well-established chemistries that target these amino groups under mild conditions. Resulting conjugates often show improved proteolytic stability and prolonged circulation by virtue of increased hydrodynamic size and steric shielding—benefits broadly documented across PEGylated proteins and peptides[90,91].

However, it is essential to note that NSP can lead to heterogeneous products, especially when multiple lysine residues are present in a protein[87]. This heterogeneity can result in variations in the degree of PEGylation and the specific sites of modification, which may affect overall bioactivity if residues near binding or active sites are modified[92-94]. By contrast, site-selective approaches (e.g., N-terminal control via pKa differences or engineered cysteine coupling) are used to mitigate these effects. An example of this comparison is carried out on exendin-4, which discusses that non-specific lysine PEGylation produced mixtures with reduced receptor binding relative to site-specific conjugates, despite improved PK[93].

Moreover, the heterogeneity of PEGylated products resulting from NSP can complicate characterization and quality control[17]. Each PEGylated protein may contain a distribution of isoforms with distinct hydrodynamic properties, leading to different clearance

behaviors and, in some cases, shifts in elimination mechanisms as hydrodynamic radius increases—factors that complicate prediction of *in vivo* performance and dosing. These considerations have driven a gradual shift toward site-controlled designs to improve consistency while retaining half-life gains.

2.3.5.2. Site-Specific PEGylation: Cysteine-targeted PEGylation

Cysteine-targeted PEGylation installs PEG at a preselected thiol, which is most commonly an engineered or solvent-exposed cysteine, using thiol-reactive handles to achieve a single, defined conjugation position and thereby overcome the positional heterogeneity typical of lysine-directed labeling[95]. This strategy has been validated clinically with the approval of the drug named certolizumab pegol (Cimzia®) by the FDA. Cimzia® is an anti-TNF Fab bearing a branched 40 kDa PEG linked via maleimide to a C-terminal cysteine, illustrating that thiol-specific, site-defined PEGylation can deliver an approved biologic with durable dosing[23,95].

The principal advantage of cysteine targeting is chemoselectivity in the presence of other nucleophiles[95]. This enables positional control that supports activity preservation when the conjugation site is placed distal to functional epitopes[96]. Under mild aqueous conditions[97], thiol-reactive handles (e.g., maleimides) react preferentially with a single engineered cysteine thiolate and outcompete lysines or serines, yielding one dominant conjugation position[95,98]. By locating that cysteine on a solvent-exposed, epitope-distal loop, the bulky, hydrated PEG is kept away from binding or active sites[95]. In contrast to non-specific PEGylation, which yields distributions of isomers with variable potency and PK[98], site-specific thiol conjugation produces more homogeneous material and facilitates rational structure–activity optimization[98].

In regulatory development, Chemistry, Manufacturing, and Controls (CMC) refers to establishing product identity, defining how it is made, and setting analytical specifications to ensure lot-to-lot consistency, which are essential aspects that are directly impacted by the conjugation strategy for PEGylated proteins. Non-specific (lysine-targeted) PEGylation can modify many surface ε-amines, creating large distributions of positional isomers that can jeopardize bioactivity and complicate purification and characterization[98]. By contrast, installing PEG at cysteine residues reduces positional heterogeneity relative to lysine-based labeling[95,98]. This leverages the relative scarcity and chemoselectivity of free thiols and, when appropriate, re-bridging of native disulfides to preserve connectivity while maintaining site control[23,95]. The resulting definition of the attachment site simplifies analytical control compared with lysine mixtures. When multiple cysteines or

disulfides are present, definition is maintained by strategy (e.g., selective thiol addressing, partial reduction, or disulfide re-bridging) to preserve connectivity and site control. In downstream processing, randomly PEGylated conjugates often require separation of multiple positional isomers, a persistent bottleneck that is mitigated when a defined cysteine site (free thiol or re-bridged disulfide) is used[23,95,98]. The practical value of site-specific modalities is reflected in marketed products, where N-terminal PEGylation (pegfilgrastim/Neulasta®) and cysteine-targeted PEGylation (certolizumab pegol/Cimzia®) exemplify approaches adopted to achieve consistent quality while retaining pharmacokinetic benefit[2,23].

Multiple thiol-addressable chemistries exist. Maleimide–PEG remains the workhorse for cysteine targeting (e.g., Cimzia®), yet maleimide thioethers can be hydrolytically labile and undergo retro-Michael exchange with endogenous thiols (e.g., albumin), which has motivated the development of stabilized thiol-reactive linkers and post-conjugation stabilization protocols to improve *in vivo* persistence while preserving site specificity[23,57,95,96].

Collectively, cysteine-targeted PEGylation combines chemoselective placement, improved homogeneity, and PK tunability—attributes that map directly onto manufacturability and clinical performance—and it stands, alongside N-terminal strategies, as a leading route within the broader, still-dominant PEGylation paradigm for half-life extension of biologics.

2.4. The IL-1β / IL-1Ra Axis in Inflammation

Interleukin-1β (IL-1β) is a master pro-inflammatory cytokine of the IL-1 family that signals through IL-1 receptor type I (IL-1R1) together with the accessory protein IL-1RAcP to activate NF-κB/Myd88 pathways[99,100]. The actions of the protein are physiologically counter-balanced by the endogenous competitive antagonist IL-1 receptor antagonist (IL-1Ra)[100]. IL-1β is produced as an inactive cytosolic pro-form and requires inflammasome/caspase-1 processing to become mature and secreted, whereas IL-1Ra is made as a secreted antagonist that binds IL-1R1 without recruiting IL-1RAcP, thereby preventing signal initiation[99,100]. **Contemporary reviews further detail that NLRP3 licensing/activation and caspase-1 cleavage are rate-limiting steps in IL-1β maturation, reinforcing this axis as a nodal point in innate inflammatory amplification[101,102].**

Homeostatically, IL-1β participates in host defense, febrile responses, leukocyte recruitment, and tissue remodeling across diverse cell types (monocytes/macrophages, neutrophils, epithelial and stromal cells), while IL-1Ra restricts excessive activation to preserve tissue integrity[100,103]. Beyond canonical innate signaling[104-106], IL-1β also shapes adaptive immunity (e.g., Th17 differentiation/maintenance), an effect documented structurally and functionally in IL-1 family syntheses[99,100,107]. Recent work extends IL-1Ra's physiological role to hematopoiesis, where reduced IL1RN expression associates with dysregulated myeloid expansion, underscoring the importance of antagonist tone *in vivo*[108-110].

In rheumatoid arthritis (RA), the synovium exhibits elevated IL-1β in tissue and synovial fluid, with IL-1–driven expression of adhesion molecules and chemokines that sustain leukocyte influx and pannus formation; IL-1β levels correlate with clinical and histologic activity[111,112]. Single-cell and spatial analyses of RA synovium now highlight IL-1–responsive stromal and myeloid niches that propagate local cytokine networks, placing the IL-1β/IL-1Ra balance at the center of joint-resident inflammation and damage pathways[113,114]. Parallel observations in human synovial tissue confirm abundant IL-1β protein in inflamed joints relative to controls, aligning with the axis' pathophysiologic weight in RA[115].

Critically, the local antagonist tone is inadequate. RA synovium contains detectable IL-1Ra, but measured IL-1Ra:IL-1 ratios (~1.2–3.6:1) fall far short of the 10–100-fold molar excess generally required to suppress IL-1 bioactivity, helping explain persistent IL-1 signaling in the joint despite endogenous antagonist production[116-118]. Mechanistically, only a small fraction of IL-1R1 occupancy is needed to trigger activation, so effective antagonism demands high local excess of IL-1Ra[119]. Several studies also suggest synovial IL-1Ra production is relatively suppressed compared to other macrophage populations, further tipping the balance toward net IL-1 activity[119]. Recent reviews also confirm that this quantitative mismatch—high IL-1β supply versus insufficient IL-1Ra—underpins chronic synovitis and tissue injury in RA[114,120].

The axis is likewise central to autoinflammatory disorders. In Familial Mediterranean Fever (FMF), MEFV variants lower the activation threshold of the pyrin inflammasome, augmenting caspase-1 processing of pro-IL-1β and producing episodic bursts of mature IL-1β that drive recurrent serosal and synovial inflammation. Contemporary pediatric and translational syntheses concur that IL-1 is the dominant effector and IL-1Ra the endogenous check[121-123]. Critically, however, the antagonist arm is quantitatively

inadequate in FMF: monocyte/macrophage studies show pyrin activation induces less IL-1Ra (IL1RN) than other inflammasomes, yielding reduced IL-1Ra transcripts/secretion and low local IL-1Ra:IL-1β ratios—even during colchicine therapy[124-126]—a mismatch that helps explain persistent IL-1 signaling during attacks[127-129].

Similar IL-1-inflammasome circuits operate in gout (crystal-induced), type 2 diabetes/metaflammation, and inflammatory bowel disease, where the local balance between IL-1β and IL-1Ra influences tissue injury, epithelial barrier dysfunction, and chronicity[112,130,131]. In the central nervous system and lung, IL-1β contributes to sterile inflammation and neuroimmune crosstalk (e.g., traumatic brain injury) and amplifies cytokine cascades via NF-κB; in these contexts, endogenous IL-1Ra constrains propagation of damage signals[132,133]. In systemic hyperinflammatory states (e.g., severe viral pneumonias), NF-κB–driven induction of IL-1 family cytokines features prominently, again framing the IL-1β/IL-1Ra ratio as a determinant of tissue injury versus resolution[134].

At the molecular level, structural studies show how agonist cytokines (IL-1α/IL-1β) form high-affinity binary complexes with IL-1R1 that recruit IL-1RAcP to assemble the signaling ternary complex, whereas IL-1Ra binds IL-1R1 but sterically prevents co-receptor recruitment, achieving competitive antagonism without signaling[99,100]. These principles have underpinned diverse antagonist designs (including receptor-based "cytokine traps") that exploit the same binding logic to neutralize IL-1 family inputs in chronic inflammatory disease[135].

Taken together, the IL-1β/IL-1Ra axis functions as a programmable rheostat for innate and adaptive inflammation. Inflammasome-dependent IL-1β supply amplifies local and systemic responses, while IL-1Ra constrains receptor-proximal activation to prevent collateral tissue damage. Dysregulated axis activity is implicated in joint-centric disease (RA), serosal/episodic inflammation (FMF), mucosal and metabolic inflammation (IBD, T2D), and neuroinflammation, with recent systems-level and mechanistic studies reinforcing its centrality across these settings[99,112,120,130].

2.5. Anakinra (Recombinant IL-1Ra): Mechanism, Indications and Clinical Use

Anakinra is the recombinant human IL-1 receptor antagonist (IL-1Ra) that competitively blocks IL-1α/β at IL-1R1, thereby suppressing downstream inflammatory signaling. It is FDA-approved for rheumatoid arthritis and for cryopyrin-associated periodic syndromes (CAPS, including NOMID). These approved uses and the dosing framework reflect the

molecule's short systemic persistence and the need for regular administration[136]. In practice, anakinra is also widely used across autoinflammatory indications—e.g., adult-onset Still's disease, difficult gout, and recurrent pericarditis—and was evaluated during COVID-19 hyperinflammation, with reviews summarizing supportive but disease-specific evidence bases[137,138]. From a developability perspective, anakinra's small size (~17 kDa) places it below the renal filtration cut-off, which contributes to rapid clearance and motivates half-life-extension approaches; clinically, daily dosing has been standard for RA[47].

2.5.1. Half-life Extension Strategies for Anakinra

Early structure–activity work on IL-1Ra showed that how and where a polymer is attached matters. Random lysine-directed PEGylation generated heterogeneous mixtures with steep activity losses, whereas thiol-selective strategies (targeting fewer, accessible cysteines) afforded more defined products with substantially higher retained antagonism—illustrated by ~10% residual activity after lysine PEGylation versus ~40% after thiol-specific coupling in matched assays[139]. Beyond activity, PEGylation has repeatedly been used to stabilize IL-1Ra in solution: a 5 kDa mono-PEG conjugate remained homogeneous during 30–60 days at room temperature while preserving bioactivity, whereas the unmodified protein degraded into multiple species with large activity losses[139]. As the field broadened, alternative polymers were compared head-to-head. Hydroxyethyl-starch "HESylation" produced a predominantly mono-adduct that maintained nanomolar affinity but with a slower on-rate, while delivering a ~6.5-fold half-life increase and ~45-fold AUC gain in rats—evidence that increasing hydrodynamic size can extend exposure with acceptable target engagement[48]. More recently, IL-1Ra half-life extension has also been pursued via nanocarriers and other polymer fusions, which again balance increased hydrodynamic size against modest effects on binding kinetics[47,140].

3. MATERIALS AND METHODS

3.1. Materials

All cell culture experiments used Dulbecco's Modified Eagle Medium (DMEM; PAN) supplemented as described in Methods. For IL-1β pathway readouts, QUANTI-Blue™ SEAP detection reagent (InvivoGen) was employed; Normocin and Zeocin (InvivoGen) were used according to the supplier's recommendations. Carrier-free recombinant human IL-1β (BioLegend) served as the stimulant in cell assays. PEGylation reagents comprised methoxy-poly(ethylene glycol) succinimidyl valerate (mPEG-SVA) at nominal 5, 10, and 20 kDa and methoxy-poly(ethylene glycol) maleimide (mPEG-MAL) at 5, 10, and 20 kDa (all Laysan Bio). DL-dithiothreitol (DTT; BioBasic) and analytical-grade buffer components—sodium phosphate dibasic, sodium phosphate monobasic, and sodium chloride (Sigma-Aldrich)—were used as received. The Cell Proliferation Kit I (MTT; Roche) and pre-stained protein molecular weight markers (Bio-Rad) were used for auxiliary assays and SDS-PAGE, respectively. Chromatography was performed on an ÄKTA FPLC system (Cytiva), and plate-based absorbance measurements were acquired on a BioTek microplate reader. Unless stated otherwise, reagents were used without further purification; aqueous solutions were prepared in ≥18 MΩ·cm water and filtered through 0.2 μm polyethersulfone (PES) membrane filters immediately before use.

The initial phase of this work was dedicated to establishing and comparing two distinct PEGylation strategies for interleukin-1 receptor antagonist (IL-1Ra). Thiol-selective PEGylation was performed using maleimide chemistry, while non-specific lysine modification was explored using NHS ester chemistry. Each approach was tested under standardized buffer conditions and across a panel of PEG molecular weights (5, 10, and 20 kDa) and PEG-to-protein molar ratios (from 0.5 to 9). This systematic screening provided a basis for evaluating how PEG size, conjugation chemistry, and reaction stoichiometry influenced product homogeneity and protein recovery.

3.2. Thiol-selective PEGylation (Thiolation)

Thiol-selective PEGylation of IL-1Ra was carried out using maleimide chemistry under defined buffer conditions (**Figure *3.1***). Proteins were transferred into 50 mM sodium phosphate buffer at pH 6.5 by repeated spin-filtration to ensure both protein stability and optimal reactivity of cysteine residues. The final protein concentration was adjusted to 5 mg/mL. Methoxy-PEG-maleimide (mPEG-mal) polymers with nominal molecular weights of 5, 10, or 20 kDa (**Table *3.1***) were freshly prepared by dissolving the

lyophilized reagent in the same phosphate buffer immediately before use to minimize hydrolysis.

Conjugation reactions were initiated by adding PEG to the protein solution at a PEG-to-protein molar ratio of 0.5. Reactions were incubated at 37 °C for 70 min with gentle agitation at 200 rpm to maintain solubility and promote homogeneous mixing of the reactants. After incubation, unreacted maleimide groups were quenched by the addition of dithiothreitol (DTT) to a final concentration of 1 mM, followed by an additional 15 min of incubation under the same conditions.

Following quenching, samples were filtered by passage through 0.22 µm PES syringe filters to remove any particulates. The filtered samples were subsequently stored at 4 °C until purification by SEC or use in downstream analyses.

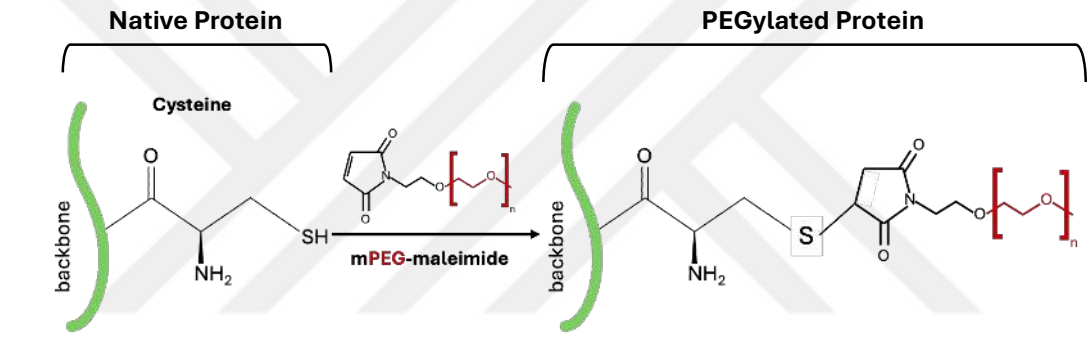

Figure 3.1: Thiol-selective PEGylation of a cysteine residue with mPEG–maleimide.

The protein backbone is indicated in green brackets; PEG is shown in red. A cysteinyl thiol reacts with the maleimide to form a stable thioether succinimide adduct, yielding the PEGylated protein (n reflects PEG chain length).

3.3. Lysine-directed PEGylation (Non-specific PEGylation)

Lysine-directed PEGylation of IL-1Ra was performed using NHS ester chemistry under controlled alkaline conditions (**Figure *3.2***). Prior to conjugation, proteins were buffer-exchanged into 50 mM sodium phosphate buffer at pH 8.0 by repeated spin-filtration to provide an optimal environment for NHS ester reactivity with primary amines. The final protein concentration was adjusted to 5 mg/mL. Methoxy-PEG-succinimidyl valerate (mPEG-SVA) polymers with nominal molecular weights of 5, 10, or 20 kDa (**Table *3.1***) were freshly dissolved in the same phosphate buffer. Stocks were prepared immediately before use to minimize hydrolysis of the active ester.

Conjugation reactions were initiated by adding PEG to the protein solution at a molar ratio of 0.5. Reactions were incubated at 37 °C for 70 min with gentle agitation at 200 rpm to maintain solubility and promote uniform mixing. After the conjugation reaction, unreacted NHS groups were quenched by the addition of glycine from a sterile 2 M stock solution to achieve a final concentration of 0.1 M. Quenching was carried out for an additional 15 min under the same temperature and mixing conditions to ensure full inactivation of reactive esters.

Following quenching, samples were passed through 0.22 µm PES syringe filters to remove any particulates. The filtered samples were subsequently stored at 4 °C until purification by SEC.

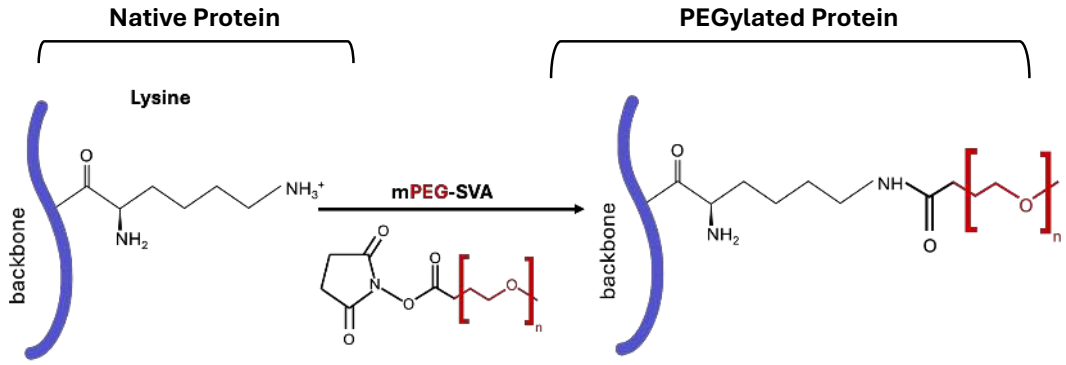

Figure 3.2: Lysine-targeted PEGylation with mPEG–SVA (NHS-activated ester).

The ε-amine of a lysine reacts to form a stable amide linkage, yielding the PEGylated protein (blue brackets = protein backbone; red = PEG; n = chain length).

Table 3.1: Experimental matrix for the head-to-head PEGylation screen.

IL-1Ra was modified either by thiol-selective (maleimide) or lysine-directed (SVA/NHS) chemistry using linear mPEG of 5, 10, or 20 kDa, all run at a fixed PEG:protein molar feed = 0.5.

Sample No	Sample Key	Type of Reaction	MW of PEG (kDa)	PEG : IL-1Ra Molar Ratio
1	**T5-0.5**	Thiolation	5	0.5
2	**T10-0.5**		10	
3	**T20-0.5**		20	
4	**N5-0.5**	Nonspecific	5	0.5
5	**N10-0.5**		10	
6	**N20-0.5**		20	

3.4. Size-Exclusion Chromatography (SEC)

Size-exclusion chromatography was employed both for polishing of purified proteins and for separation of PEGylated species from unmodified protein and excess polymer (**Figure *3.3***). All chromatographic runs were carried out on an ÄKTA FPLC system equipped with a Superdex 75 pg 16/600 column (column volume ~120 mL) and a UV280 detector with a 2 mm path length. Prior to use, the column was washed with one column volume of distilled water at a flow rate of 1.2 mL/min until the conductivity reached baseline and was then equilibrated under the same flow conditions with 20 mM sodium phosphate, 20 mM NaCl, and 2 mM DTT at pH 7.4. This buffer was used both for native protein separations and for PEGylated conjugates, as reactions had already been completed and quenched with 1 mM DTT prior to loading. All buffers were 0.22 µm-filtered and degassed before application to the system.

Protein or PEGylation reaction mixtures were filtered through 0.22 µm PES syringe filters before loading. Sample volumes did not exceed 5% of the column volume (~6 mL per run) in order to maintain resolution. Elution was carried out at a flow rate of 0.7 mL/min at room temperature, and fractions were collected across the elution profile. Peaks

corresponding to different oligomeric states or PEGylated forms were identified by elution position and subsequently confirmed by SDS-PAGE. Fractions of interest were pooled and stored at 4 °C for downstream applications. For quantitative analyses, peak areas (mL·mAU) were integrated and quantified using GraphPad Prism (GraphPad Software, San Diego, CA).

After each run, the column was washed with distilled water and stored in 20% ethanol according to the manufacturer's guidelines.

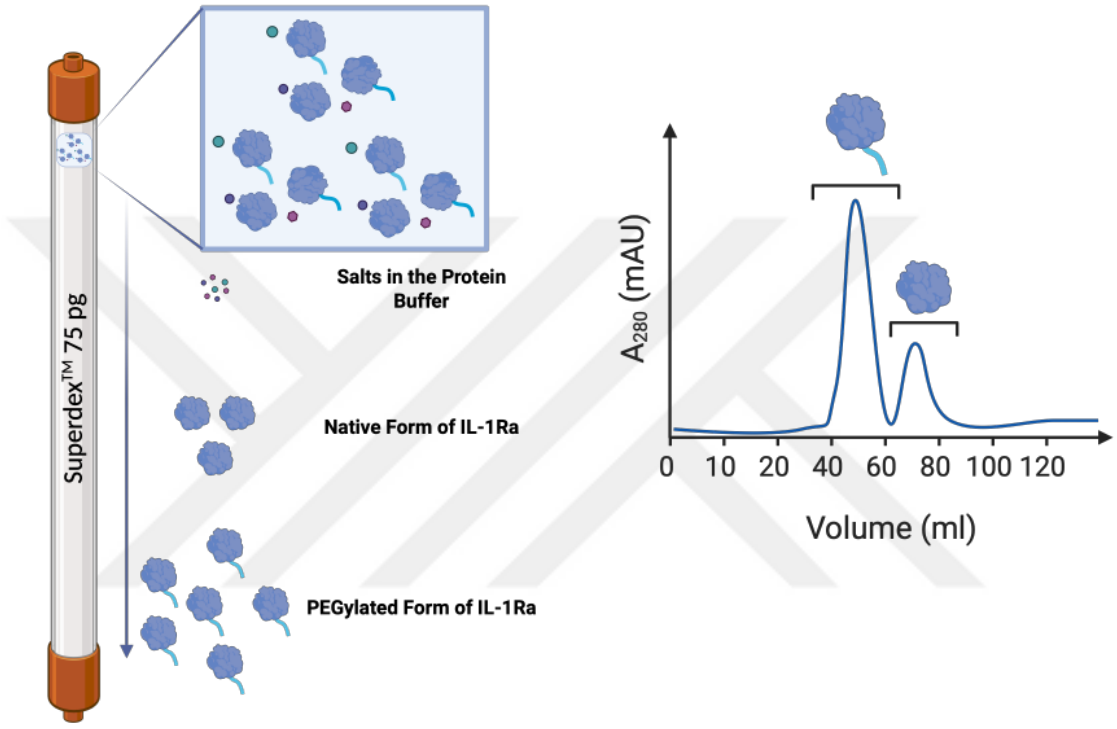

Figure 3.3: SEC workflow and elution behavior for IL-1Ra on Superdex™ 75 pg.

PEGylation increases hydrodynamic size, causing the conjugate to elute earlier than native IL-1Ra, while buffer salts elute near the total volume. The schematic trace (A280 vs. volume) illustrates the expected peak order and baseline separation.

3.5. Gel Electrophoresis (SDS-PAGE)

SDS-PAGE was employed to evaluate the purity of collected fractions and to confirm the identity of peaks obtained from SEC. Protein aliquots were mixed with Laemmli sample buffer at a 1:4 ratio, and samples were subsequently heated at 90 °C for 5 min prior to loading.

Proteins were resolved on pre-cast gradient gels (4–15%) to improve the separation of PEGylated conjugates from unmodified protein. Electrophoresis was carried out in Tris–Glycine–SDS running buffer at a constant voltage ranging from 120 to 200 V until the

dye front reached the bottom of the gel. A molecular weight marker was loaded in parallel with all samples to allow for calibration of apparent molecular mass.

Following electrophoresis, gels were stained with Coomassie Brilliant Blue and destained using a 40% methanol/10% acetic acid solution. Gels were imaged under standardized conditions to ensure comparability across experiments. PEGylated proteins consistently exhibited an upward shift in apparent molecular weight compared with the unmodified protein, thereby providing a clear confirmation of conjugation.

3.6. Stoichiometric Ratio Optimization of PEG10 Thiolation

In addition to the chain length comparisons, a separate set of thiolation reactions was carried out using PEG10 to examine the effect of varying protein-to-PEG stoichiometry. All reactions were conducted under the same buffer and incubation conditions as described above, with protein adjusted to 5 mg/mL and PEG10 added at defined molar ratios of 0.5, 1.5, 3, 6, and 9 (PEG : Protein). After quenching with DTT and filtration, samples were purified by SEC and analyzed by SDS-PAGE to evaluate the conjugation profiles. These ratio-variation experiments formed the methodological basis for the subsequent structural and functional characterization studies.

After establishing the PEGylation conditions and purifying the conjugates by SEC and SDS-PAGE, subsequent experiments were designed to evaluate their biological activity *in vitro*. For these studies, HEK-Blue™ IL-1β reporter cells (Invivogen) were used as a model system to quantify IL-1β signaling and its inhibition by PEGylated IL-1Ra variants. An initial viability assessment was performed to decide on the stimulation regimen that was well tolerated by the cells.

3.7. Cell Culture on HEK-Blue IL1 β Cells: IL-1β Dose–Response (EC_{50}, EC_{80}, and EC_{90})

For IL-1β dose–response assays, HEK-Blue™ IL-1β cells were seeded in 96-well plates at a 25,000 cell/well density and allowed to adhere overnight. Cells were then stimulated with increasing concentrations of recombinant human IL-1β ranging from 0 to 100 ng/mL, as confirmed by the viability experiments. After 24 h of stimulation, 17 µL of culture supernatant from each well was transferred to a fresh 96-well plate containing 150 µL of QUANTI-Blue™ solution. Plates were incubated for 2 h at 37 °C, and SEAP activity was quantified spectrophotometrically at 640 nm using a microplate reader. Each IL-1β concentration was tested in technical triplicates (**Figure *3.4***).

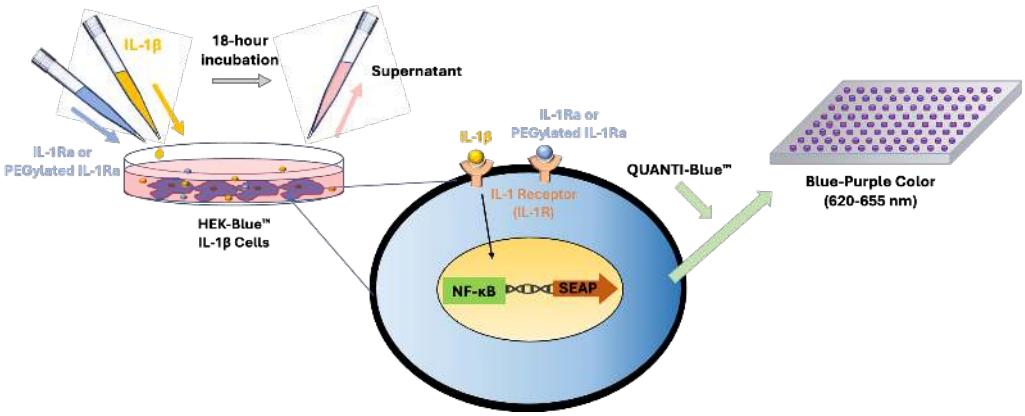

Figure 3.4: Schematic of the HEK-Blue™ IL-1β assay.

HEK-Blue IL-1β cells are co-incubated with IL-1β and IL-1Ra or PEGylated IL-1Ra; antagonism at IL-1R1 reduces NF-κB–driven secretion of SEAP. After ~18 h, supernatants are transferred to QUANTI-Blue™, and absorbance at 620–655 nm is read to generate dose–response curves (normalized to the IL-1β-only control).

Dose–response data were analyzed by nonlinear regression using a four-parameter logistic (4PL) model. Effective concentration values (EC_{50}, EC_{80}, EC_{90}) were derived from the fitted curves according to the fractional effect model:

$$EC_x = c.\left(\frac{x}{1-x}\right)^{\frac{1}{b}} \qquad (1.1)$$

where x is the fractional effect (e.g., 0.5, 0.8, 0.9), c is the fitted EC_{50} value, and b is the Hill slope. This expression is algebraically derived from the standard 4PL model under the assumption of normalized response data, as outlined in Sebaugh (2011) [Pharm. Stat., 10(2):128–134].

3.8. Cell Viability Assay for PEGylated Conjugates

After the IL-1β dose–response curve had been established, the next stage of the study was to compare the performance of different antagonists under identical assay conditions. Prior to conducting the comparative antagonist performance assays, the viability of HEK-Blue™ IL-1β cells in response to stimulation with Anakinra and its PEGylated conjugates was evaluated.

The antagonist panel included Anakinra as the reference protein together with PEGylated variants generated at a 0.5 protein-to-PEG molar ratio: lysine-directed conjugates (N20, N10, N5) and thiol-selective conjugates (T10, T5).

Cells were seeded in 96-well plates at a 25,000 cell/well and allowed to adhere overnight before stimulation. Each antagonist was tested at seven EC_{80}-scaled doses—0.02×, 0.2×,

2×, 20×, 100×, 200×, and 400× the IL-1β EC_{80} for HEK-Blue™ IL-1β cells—corresponding in this study to 0.25–5035 pM. After 24 h of stimulation, the medium was replaced with 0.5 mg/mL MTT reagent (Sigma-Aldrich) and incubated for 4 h at 37 °C. The resulting formazan crystals were solubilized overnight in 100 µL DMSO per well, and absorbance was measured at 570 nm using a plate reader.

3.9. Cell Culture on HEK-Blue IL-1β Cells: Antagonist Performance (IC50,IC80, and IC_{90})

Once it had been confirmed that neither Anakinra nor its PEGylated conjugates compromised HEK-Blue™ IL-1β cell viability under the assay conditions, the same panel of antagonists was evaluated for their inhibitory performance against IL-1β signaling. The comparative inhibitory activity of Anakinra and its PEGylated conjugates was assessed using the HEK-Blue™ IL-1β reporter system (**Figure *3.4***). The antagonist panel comprised Anakinra together with lysine-directed PEGylated variants (N20, N10, N5) and thiol-selective PEGylated variants (T10, T5), all synthesized at a 0.5 protein-to-PEG molar ratio.

Cells were seeded in 96-well plates at a 25,000 cell/well and allowed to adhere overnight before stimulation. For each experiment, a fixed concentration of recombinant human IL-1β corresponding to the EC_{80} value determined from the dose–response curve was used to activate NF-κB/AP-1 signaling.

Antagonists were administered concurrently with IL-1β at seven EC_{80}-scaled doses—0.02×, 0.2×, 2×, 20×, 100×, 200×, and 400×—corresponding in this study to 0.25–5035 pM. After 24 h of incubation, 17 µL of culture supernatant from each well was transferred to a fresh 96-well plate containing 150 µL QUANTI-Blue™ solution. Plates were incubated for 2 h at 37 °C, and SEAP activity was quantified spectrophotometrically at 640 nm using a plate reader. All conditions were tested in technical triplicates.

Inhibition data were analyzed by nonlinear regression using a four-parameter logistic (4PL) model. Half-maximal inhibitory concentration values (IC_{50}), together with IC_{80} and IC_{90} values where applicable, were calculated from the fitted curves. These experiments enabled direct comparison of the antagonistic potency of Anakinra and its PEGylated conjugates under standardized assay conditions.

3.10. Labeled Synthesis of Mutant IL-1Ra (M143V) and its Biopyhsical Characterizations

In addition to experiments performed with commercially available IL-1Ra, this study also employed a recombinant IL-1Ra variant carrying a single amino acid substitution at

position 143 (M143V). The principal motivation for introducing this mutant was to establish a recombinant construct distinct from the marketed therapeutic form, thereby avoiding potential intellectual property conflicts while enabling in-house expression and modification.

The M143V substitution was chosen based on prior project design work combining in silico analyses and naturally occurring human polymorphisms. Computational studies suggested that substitutions in regions not directly involved in IL-1 receptor binding could serve as candidates for PEGylation without affecting functional activity. Among several naturally observed polymorphisms in IL1Ra, the M143V variant was identified as a change unlikely to disrupt protein folding or receptor interactions, while still maintaining functional integrity and providing a molecularly distinct backbone for downstream engineering.

Importantly, the M143V substitution does not alter the cysteine residues that serve as the primary PEGylation sites of IL-1Ra, and structural considerations further suggest that the mutation does not perturb the overall fold of the protein. This supports its suitability for site-specific PEGylation, conjugation optimization, and subsequent functional analyses.

To illustrate the difference between the native recombinant IL-1Ra and the variant used in this work, a sequence alignment is provided (*Figure 3.5*). The alignment highlights that the two proteins share 99.3% identity across 153 amino acids, with only a single substitution at position 143 where methionine (M) is replaced by valine (V). This change does not involve any of the cysteine residues that serve as PEGylation sites, and it is not expected to perturb the overall fold of the protein.

```
99.3% identity in 153 residues overlap; Score: 805.0; Gap frequency: 0.0%

Rec. IL1-Ra    1 MRPSGRKSSKMQAFRIWDVNQKTFYLRNNQLVAGYLQGPNVNLEEKIDVVPIEPHALFLG
      M143V    1 MRPSGRKSSKMQAFRIWDVNQKTFYLRNNQLVAGYLQGPNVNLEEKIDVVPIEPHALFLG
                 ************************************************************

Rec. IL1-Ra   61 IHGGKMCLSCVKSGDETRLQLEAVNITDLSENRKQDKRFAFIRSDSGPTTSFESAACPGW
      M143V   61 IHGGKMCLSCVKSGDETRLQLEAVNITDLSENRKQDKRFAFIRSDSGPTTSFESAACPGW
                 ************************************************************

Rec. IL1-Ra  121 FLCTAMEADQPVSLTNMPDEGVMVTKFYFQEDE
      M143V  121 FLCTAMEADQPVSLTNMPDEGVVVTKFYFQEDE
                 ********************* **********
```

Figure 3.5: Sequence alignment of recombinant IL-1Ra and the M143V variant used in this study.

The two sequences share 99.3% identity across 153 residues, with a single amino acid substitution (M → V) at position 143.

3.11. Plasmid Construction and Transformation

The E. coli BL21-AI strain harboring the pDEST14-IL1RA-M143V-histag plasmid was kindly provided by collaborators at İstanbul University and subsequently used for all protein expression and purification experiments described in this thesis.

For heterologous expression of M143V-IL-1Ra, a pDEST14-based plasmid encoding the M143V variant with a C-terminal 6×His tag (pDEST14-IL1RA-M143V-histag) was employed. This plasmid carries an ampicillin resistance gene for bacterial selection and is driven by a T7 promoter with transcription termination under the control of a T7 terminator. The principal features of the plasmid, including the gene of interest, His-tag, promoter, and selection markers, are illustrated in **Figure *3.6***.

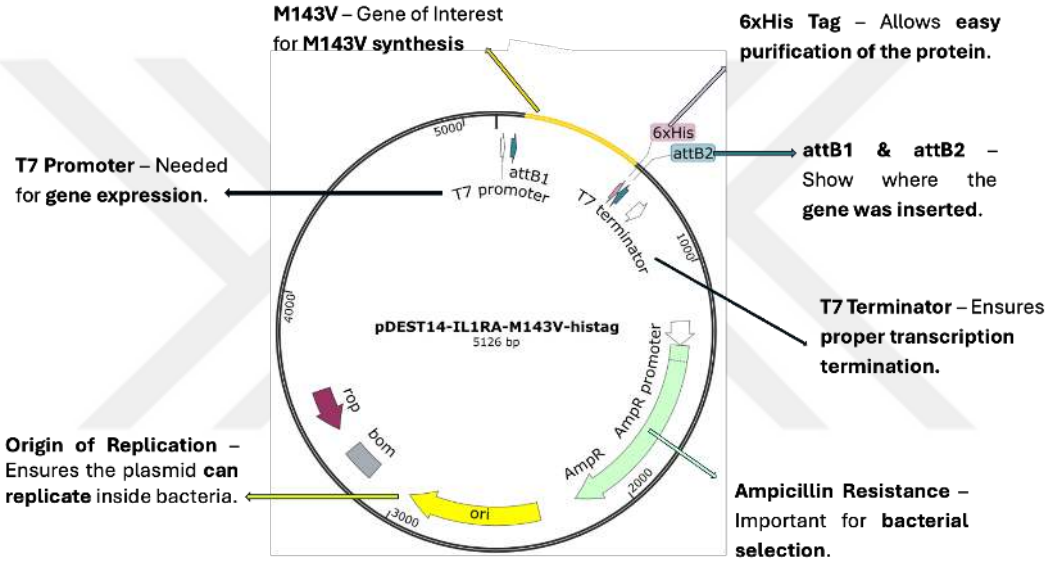

Figure 3.6: Plasmid map of pDEST14-IL1RA-M143V-histag used for recombinant expression in E. coli BL21-AI cells.

The site-directed mutagenesis and subsequent transformation of the plasmid into E. coli BL21-AI cells were performed externally by collaborators at İstanbul University. Mutagenesis was carried out using a Q5 Site-Directed Mutagenesis Kit (New England Biolabs, Ipswich, MA, USA), and transformation was achieved by heat-shock of chemically competent E. coli cells, followed by recovery in SOC medium and plating on LB–agar supplemented with ampicillin. Colonies were screened by miniprep, restriction analysis, and sequencing to confirm the presence of the M143V mutation. BL21-AI cells were selected for expression because they carry a chromosomally integrated T7 RNA polymerase under the control of the arabinose-inducible PBAD promoter, enabling tightly regulated protein expression.

3.12. Structural Modeling of M143V Using AlphaFold2

The three-dimensional structure of the M143V mutant of IL-1Ra was predicted using AlphaFold2 (v2.1.0). The full-length amino acid sequence of the M143V variant was used as input, and structure prediction was carried out with default parameters. For each run, five structural models were generated and ranked according to AlphaFold's internal confidence metrics.

Structural reliability was assessed using the predicted local-distance difference test (pLDDT) scores, which provide per-residue confidence estimates, and the predicted aligned error (PAE), which reports the expected positional error between aligned residues. Model confidence was further examined through visual inspection of regions with lower pLDDT values to identify potentially flexible or uncertain segments.

To evaluate the impact of the M143V substitution, the top-ranked AlphaFold2 model was superimposed on the experimental NMR structure of wild-type IL-1Ra (PDB: 1IRP) using PyMOL (v2.5). The local environment of residue 143 was analyzed in detail to determine whether the substitution introduced steric clashes or altered the spatial arrangement of nearby residues.

3.13. Protein Expression in LB Medium

Initial expression trials of M143V-IL-1Ra were performed in LB medium to establish optimal induction and growth conditions. E. coli BL21-AI cells harboring the pDEST14-IL1RA-M143V-histag plasmid were first inoculated at 50 mL of LB broth containing 150 μg/mL ampicillin and grown overnight at 37 °C while shaking at 200 rpm.

The following day, each overnight starter was used to inoculate 1 L of LB medium supplemented with ampicillin. Cultures were incubated at 37 °C with shaking until reaching mid-logarithmic phase ($OD_{595} \approx 0.6$). Protein expression was induced with L-arabinose at a final concentration of 0.2% (w/v), exploiting the arabinose-inducible PBAD promoter controlling T7 RNA polymerase expression in BL21-AI cells. Immediately after induction, cultures were shifted to 22 °C to favor correct folding and solubility of the expressed protein. Incubation was continued overnight (18–20 h), after which cells were harvested by centrifugation at 4,200 × g for 45 min at 4 °C.

The LB-based expression protocol served as a foundation for optimizing induction timing, temperature, and growth phase. Once consistent yields were obtained, the same strategy was adapted to M9 minimal medium supplemented with $^{15}NH_4Cl$ as the nitrogen source, enabling the production of uniformly isotope-labeled protein for two-dimensional HSQC NMR analysis.

3.14. Isotope-Labeled Protein Expression in M9 Medium

For NMR spectroscopy, uniformly ^{15}N-labeled M143V-IL-1Ra was produced in M9 minimal medium using a three-phase cultivation scheme. E. coli BL21-AI cells harboring the pDEST14-IL1RA-M143V-histag plasmid were first inoculated into 50 mL of LB broth supplemented with 150 µg/mL ampicillin and incubated at 37 °C while shaking (200 rpm) for approximately 12 h.

From this LB starter, 0.5 mL was used to inoculate a 50 mL M9 ^{15}N starter culture containing $^{15}NH_4Cl$ (1 g/L) as the sole nitrogen source, glucose as the carbon source, $MgSO_4$, $CaCl_2$, trace metals, vitamins, and ampicillin. This M9 starter was incubated overnight, at 37 °C while shaking at 200 rpm (**Figure *3.7***).

On the following day, the production cultures (1.0 L per 2 L Erlenmeyer flask) were inoculated with the M9 ^{15}N starter and grown at 37 °C until $OD_{595} \approx 0.5$. Cultures were then cooled to 22 °C, and protein expression was induced with L-arabinose at a final concentration of 0.2% (w/v) once OD_{595} reached ~0.6. Induction proceeded overnight (~18–20 h) at 22 °C to favor soluble expression (**Figure *3.7***)..

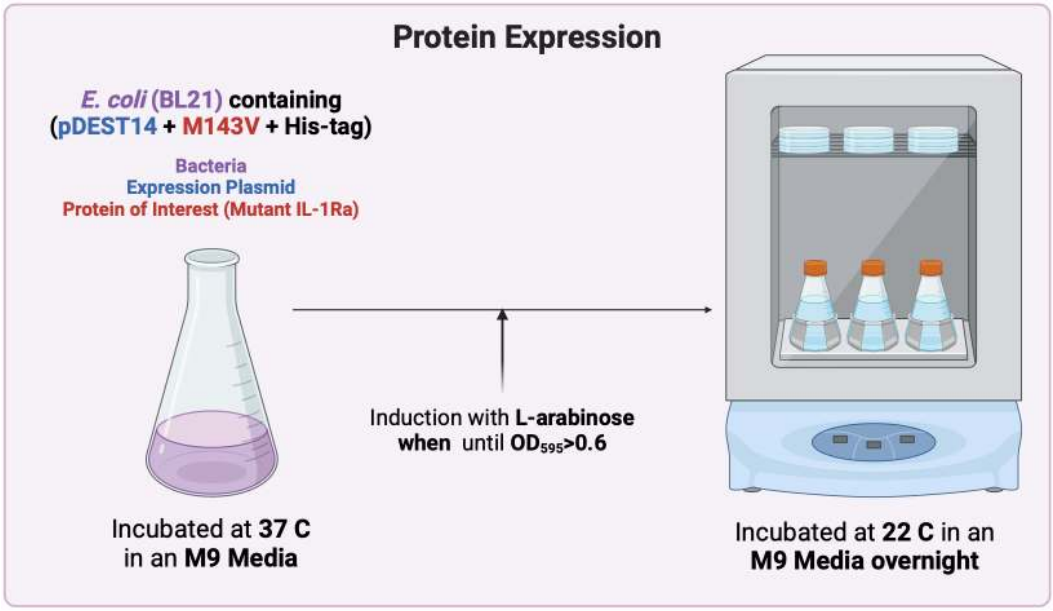

Figure 3.7: Expression workflow for M143V-IL-1Ra.

E. coli BL21 carrying pDEST14–M143V–6×His was grown in M9 medium at 37 °C to $OD_{595} > 0.6$, induced with L-arabinose, and shifted to 22 °C overnight in a shaking incubator to produce the recombinant protein.

Cells were harvested by centrifugation at 4,200 × g for 45 min at 4 °C, and the resulting pellets were immediately resuspended in lysis buffer (50 mM sodium phosphate, 500 mM

NaCl, 5% glycerol, 0.1% Triton X-100, and 2 mM β-mercaptoethanol, pH 7.5). Pellets were either processed directly for cell disruption or stored at −45 °C until purification. Protein produced by this labeling protocol was used for two-dimensional $^{1}H–^{15}N$ HSQC NMR experiments and subsequent structural analyses.

3.15. Purification of M143V-IL-1Ra

Proteins expressed in both LB and M9 media were purified using an identical two-step process consisting of Ni^{2+}-affinity chromatography followed by size-exclusion chromatography (SEC).

3.15.1. His-tag affinity chromatography

Cell pellets resuspended in lysis buffer were thawed on ice and subjected to probe sonication, performed on ice in cycles of 10 s on/10 s off to prevent overheating, until the suspension appeared visually clarified. The resulting lysate was centrifuged at 30,000 × g for 1 hour at 4 °C, and the supernatant was carefully collected to remove cell debris and insoluble material.

The clarified lysate was applied either to a manually packed Ni^{2+}-NTA gravity column or to a pre-packed HisTrap™ FF column (Cytiva) on an ÄKTA FPLC system. Prior to application, the resin was first flushed with distilled water and then equilibrated with HisA buffer. After loading the clarified supernatant, the column was washed with HisA until the absorbance returned to baseline. Additional stepwise washes were performed using HisA supplemented with increasing concentrations of imidazole (10, 20, 40, and 250 mM) to remove nonspecifically bound proteins. Elution of His-tagged M143V-IL-1Ra was achieved with the elution buffer, which contains 500 mM imidazole. Fractions were collected on ice and analyzed by SDS-PAGE for protein content and purity. The exact compositions of the buffers used for equilibration, washing, and elution are summarized in **Table 3.2**, while the purification workflow is illustrated schematically in **Figure 3.8**.

Table 3.2: Composition of His-tag purification buffers (HisA and HisB) and imidazole wash buffers used for Ni^{2+}-affinity chromatography of M143V-IL-1Ra.

	HisA	10 mM	20 mM	40 mM	250 mM	Elution (E)
KH_2PO_4	11.61 mM	11.61 mM	11.61 mM	11.61 mM	11.61 mM	11.61 mM
Na_2HPO_4	38.39 mM	38.39 mM	38.39 mM	38.39 mM	38.39 mM	38.39 mM
NaCl	100 mM	100 mM	100 mM	100 mM	100 mM	100 mM
BME	2 mM	2 mM	2 mM	2 mM	2 mM	2 mM
Imidazole	0	10 mM	20 mM	40 mM	250 mM	500 mM

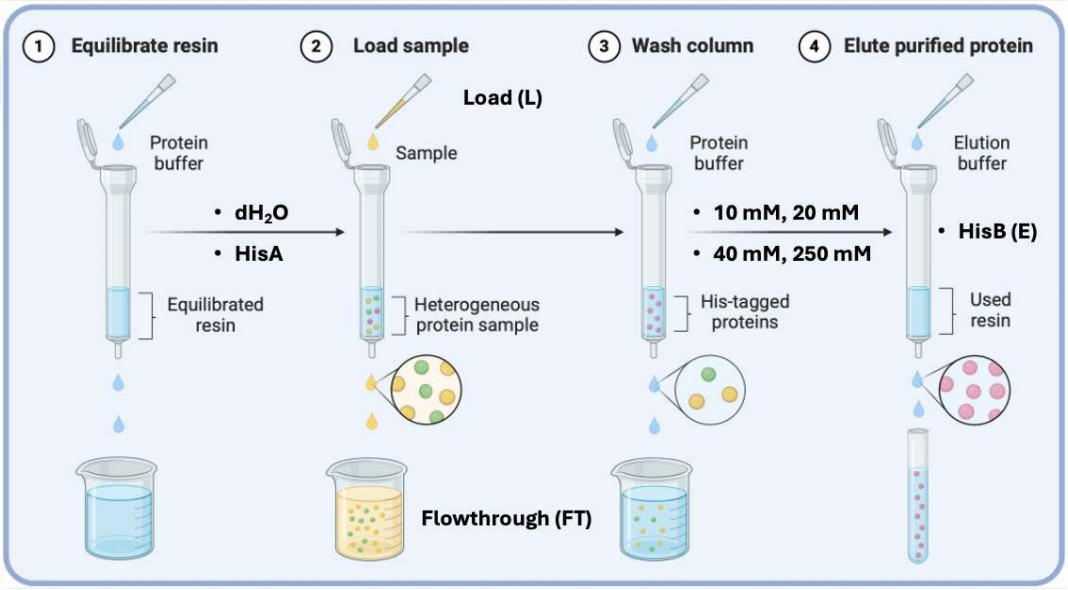

Figure 3.8: Workflow of Ni^{2+}-affinity purification of His-tagged M143V-IL-1Ra.

Resin was flushed with dH_2O, equilibrated with HisA, loaded with clarified lysate, washed with HisA and increasing imidazole concentrations, and eluted with HisB.

Elution fractions containing the target protein were combined based on UV absorbance profiles and verification by SDS-PAGE. The pooled fractions were concentrated using centrifugal ultrafiltration devices with a 10 kDa molecular weight cutoff and subjected to size-exclusion chromatography (SEC) for polishing. SEC was performed on a Superdex 75 pg 16/600 column equilibrated with the buffer described earlier in the methodology. The concentrated protein solution was carefully applied to the column, and elution was monitored at 280 nm. Fractions corresponding to the monomeric form of M143V-IL-1Ra were identified by their elution profile, collected on ice, and confirmed by SDS-PAGE. Selected fractions were pooled and stored at 4 °C until downstream use.

3.16. PEGylation of ^{15}N-Labeled M143V for NMR Analysis

For structural analysis by two-dimensional HSQC NMR, purified ^{15}N-labeled M143V-IL-1Ra was subjected to thiol-selective PEGylation. Following SEC purification, the protein was initially present in a buffer containing 2 mM DTT as a reducing agent, which would otherwise inhibit thiolation. To remove DTT, the protein was exchanged into thiolation buffer (50 mM sodium phosphate, pH 6.5) by repeated centrifugal concentration and dilution. After buffer exchange, the protein was stored at 4 °C for 24 h to allow residual reducing equivalents to dissipate and ensure that thiols were no longer maintained in a reduced state. The final protein concentration was adjusted to ~5 mg/mL prior to conjugation.

PEGylation of ^{15}N -labeled M143V-IL-1Ra was performed using the thiol-selective protocol described above with mPEG-maleimide (10 kDa) at a PEG:protein molar ratio of 0.5. Following conjugation and quenching, the reactions were subjected to size-exclusion chromatography (SEC) and SDS-PAGE, as described previously, to ensure a homogeneous PEGylated conjugate profile.

3.17. HSQC NMR of Labeled IL-1Ra Variants for Structural Characterization and PEGylation Site Mapping

Two-dimensional ^{1}H-^{15}N HSQC spectra were acquired on a Bruker 500 MHz Ascend NMR spectrometer operating at room temperature. For each sample, 500 µL of purified protein solution (either non-PEGylated or PEGylated ^{15}N-labeled M143V-IL-1Ra) was prepared, filtered through 0.22 µm PES syringe filters, and mixed with 50 µL of D_2O to provide the deuterium lock signal. Data were collected using standard Bruker pulse programs for HSQC, with acquisition parameters optimized for backbone amide detection.

Spectral processing and preliminary inspection were carried out on the NMRbox platform, which provides virtual machine access to specialized NMR software. Raw datasets were processed using Bruker TopSpin, and contour plots of the two-dimensional spectra were visualized and manually inspected in Sparky. This step allowed quality control of the acquired data, verification of expected signal dispersion, and preliminary peak picking before proceeding to residue-level analysis.

For chemical shift assignment, experimental peak positions were compared against reference values in the previously published assignments for IL-1Ra. To assist in this process, a custom Python workflow was developed (**Appendix 9.1**). The algorithm

calculated weighted chemical shift distances between experimental and reference peaks using the following formula[141]:

$$\delta = \sqrt{(5\ x\ \Delta\delta^{1H})^2 + (\Delta\delta^{15N})^2} \quad (1.2)$$

Here, $\Delta\delta^{1H}$ and $\Delta\delta^{15N}$ represent the differences in chemical shift values for ^{1}H and ^{15}N dimensions, respectively, with the proton contribution weighted by a factor of 5 to account for its narrower chemical shift dispersion. The workflow performed bidirectional comparisons: for each reference residue, the nearest experimental peak was identified, and reciprocally, for each experimental peak, the closest reference residue was determined. Only those assignments consistent in both directions were retained, with a tolerance threshold of 8.0 applied to exclude mismatches.

An iterative, tiered matching approach was implemented in which matched residues and experimental peaks from each round were removed before repeating the procedure. This cycle was continued until no further matches could be identified. At each tier, assignment tables were generated and saved, allowing stepwise refinement of residue identification. This approach ensured a systematic reduction of ambiguity in the peak-to-residue matching process and provided a reproducible framework for evaluating the correspondence between experimental and reference data.

Both the non-PEGylated and PEGylated ^{15}N-labeled samples were processed using this pipeline. The resulting assignments formed the basis for subsequent analyses of chemical shift perturbations and facilitated direct comparison of the structural fingerprints of M143V-IL-1Ra before and after PEGylation.

To quantify these perturbations, residue-wise values were plotted and color-coded according to three thresholds: 0.25, 0.40, and 1.00 ppm, representing mild, moderate, and high perturbations, respectively. This classification provided a systematic framework for distinguishing background variation from meaningful chemical shift changes associated with PEGylation.

Importantly, by mapping the residues that displayed the most pronounced perturbations or disappeared from the spectra after conjugation, this approach also enabled identification of the **PEGylation site** within the protein.

3.18. Biological Analysis of M143V in Comparison to Commercially Available IL-1Ra (Anakinra)

Following structural and biophysical characterization of M143V and its PEGylated derivatives, we next evaluated functional activity in a standardized IL-1β signaling assay.

Whereas the preceding chapter established PEGylation profiles and physicochemical integrity, the goal here was to test whether these modifications altered antagonism of IL-1β–driven pathways under matched conditions. To that end, comparative inhibition assays were performed with Anakinra, M143V, and their 10 kDa PEG conjugates (T10-Anakinra, T10-M143V) using HEK-Blue™ IL-1β cells and QUANTI-Blue™ readout.
HEK-Blue™ IL-1β cells were chosen because they provide a sensitive, pathway-specific, and highly reproducible reporter of IL-1R–NF-κB/AP-1 activation. The built-in SEAP reporter enables precise EC/IC curve fitting from the same assay plate, minimizing inter-experiment variability and allowing direct potency comparisons across all antagonists. This platform also mirrors the conditions used widely for IL-1 biology benchmarking, facilitating interpretation alongside the literature and ensuring that observed differences reflect antagonist performance rather than model-to-model variability.

3.19. Cell Viability on HEK-Blue™ IL-1β Cells (Antagonist-Only)

Before the comparative inhibition assays, we verified that the test antagonists did not compromise HEK-Blue™ IL-1β cell viability under the assay conditions. Cells were seeded in 96-well plates and allowed to adhere overnight. The M143V mutant was tested at 0.25, 2.52, 25.17, 125.87, 629.37, 2,517.50, and 5,034.99 pM. After 24 h exposure, 0.5 mg mL^{-1} MTT in complete medium was added for 4 h at 37 °C; formazan was dissolved in 100 µL DMSO (overnight, RT) and absorbance read at 570 nm. These measurements confirmed that the concentrations used in the subsequent inhibition assays did not reduce cell viability.

3.20. HEK-Blue™ IL-1β Antagonist Performance (QUANTI-Blue; IC_{50}/IC_{80}/IC_{90})

Inhibition of IL-1β signaling was then quantified for the same six antagonists using the HEK-Blue™ IL-1β reporter system. Cells were seeded in 96-well plates and allowed to adhere overnight. A fixed IL-1β concentration equal to the assay EC_{80} (established previously) was added to all wells. Antagonists were co-applied at 0.25, 2.52, 25.17, 125.87, 629.37, 2,517.50, and 5,034.99 pM, which correspond to 0.02×, 0.2×, 2×, 10×, 50×, 200×, and 400× the IL-1β EC_{80} on a molar basis. After 24 h, 17 µL supernatant was transferred to 150 µL QUANTI-Blue™ solution, incubated for 2 h at 37 °C, and SEAP activity was read at 640 nm. All conditions were run in technical duplicates.Percent inhibition was calculated relative to IL-1β-only controls and fit by nonlinear regression to a four-parameter logistic (4PL) model. IC_{50} values (and, where appropriate, IC_{80}/IC_{90})

were extracted from the fits, enabling direct comparison of Anakinra versus M143V and the impact of 10 kDa PEGylation (maleimide vs NHS) under matched conditions.

4. RESULTS

The primary objective of this study was to evaluate two distinct PEGylation strategies for IL-1Ra—site-specific thiol-selective conjugation using mPEG-maleimide and non-specific lysine-directed conjugation using mPEG-succinimidyl valerate (mPEG-SVA). These two chemistries were investigated in parallel to compare their efficiency, product homogeneity, and overall impact on protein stability and function. The study focused on both the commercially available form of IL-1Ra (Anakinra) and the engineered M143V variant, thereby enabling a direct comparison of their structural and functional properties under identical experimental conditions.

Results are presented in a sequence that follows the experimental design. First, the optimization of PEGylation conditions and comparative evaluation of PEG sizes (5, 10, and 20 kDa) are described. This is followed by structural characterization of conjugates through SEC, SDS-PAGE, and spectroscopic analyses. Finally, the biological activity of PEGylated and non-PEGylated proteins is examined in cell-based assays, including dose–response, and antagonist efficacy.

4.1. Thiol-selective PEGylation (Thiolation)

Thiol-selective PEGylation was employed to conjugate methoxy-PEG-maleimide (mPEG-mal) polymers to the free cysteine residues of IL-1Ra. This chemistry relies on the high specificity of maleimide groups for thiol moieties at near-neutral pH, resulting in covalent thioether linkages that are stable under physiological conditions. By exploiting the natural cysteine sites of IL-1Ra, thiolation enables site-specific PEGylation with reduced heterogeneity compared to lysine-directed approaches.

To visualize the potential thiol-reactive sites within IL-1Ra, structural models of the protein were analyzed and rendered using PyMOL (Schrödinger, LLC) (**Figure 4.1**). IL-1Ra contains four cysteine residues located at positions 67, 70, 117, and 123. These residues represent the potential anchoring points for thiol-selective PEGylation via methoxy-PEG-maleimide (mPEG-mal).

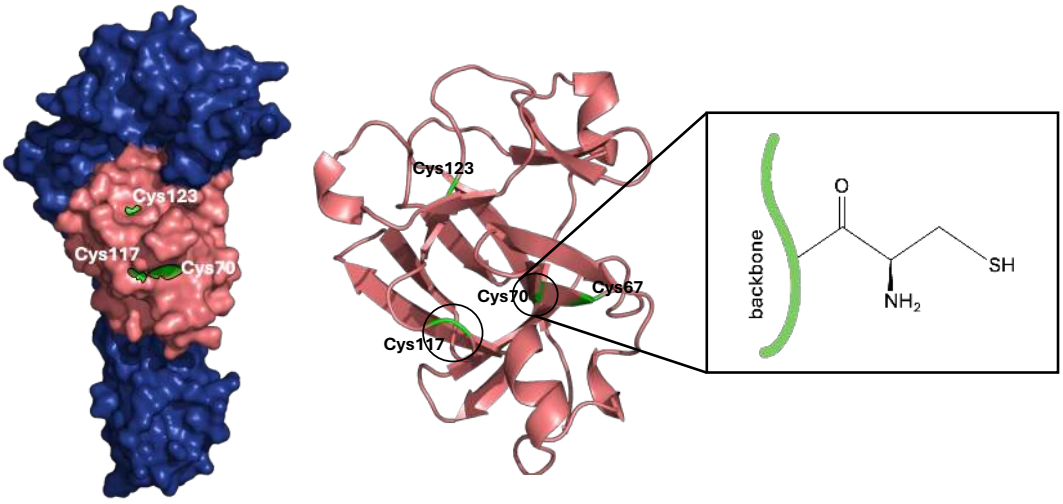

Figure 4.1: Surface and ribbon representation of IL-1Ra highlighting cysteine residues (green).

Left: IL-1Ra bound to IL-1 receptor (blue) with cysteine residues highlighted in green. Middle: Ribbon representation showing cysteines at positions 67, 70, 117, and 123. Right: schematic structure of a cysteine side chain (–SH group) as the reactive site for PEGylation.

To assess the influence of PEG chain length, 5, 10, and 20 kDa mPEG-mal reagents were tested, with reactions initially performed at a PEG:protein molar ratio of 0.5 (

Table **4.1**). **This minimum ratio was selected as a starting point under the rationale that near-stoichiometric PEG availability might favor the formation of more homogeneous conjugate species by limiting excessive multi-site modification, while still allowing efficient conjugation.** Importantly, generating a more homogeneous population of PEGylated conjugates also facilitates downstream purification and analytical characterization, as fewer species reduce overlap in chromatographic separation and simplify interpretation of biophysical and functional assays. Subsequent analyses, therefore, enabled evaluation of both polymer size and conjugation efficiency under conditions designed to maximize homogeneity.

Table 4.1: Overview of PEGylation conditions tested for IL-1Ra.

Samples were prepared using thiol-selective (mPEG-maleimide, T) chemistry with PEG polymers of 5, 10, and 20 kDa at an initial PEG:protein molar ratio of 0.5.

Sample No	Sample Key	Type of Reaction	MW of PEG (kDa)	PEG : IL-1Ra Molar Ratio
1	**T5-0.5**	Thiolation	5	0.5
2	**T10-0.5**		10	
3	**T20-0.5**		20	

Thiolation with 5 kDa mPEG-mal was analyzed by SEC to determine conjugation efficiency and product distribution (**Figure *4.2***). The chromatogram showed a major PEGylated peak accounting for 80.88% of the total protein and a smaller peak representing unmodified Anakinra at 19.12%. This indicates that conjugation with 5 kDa PEG was highly efficient and produced a relatively homogeneous profile.

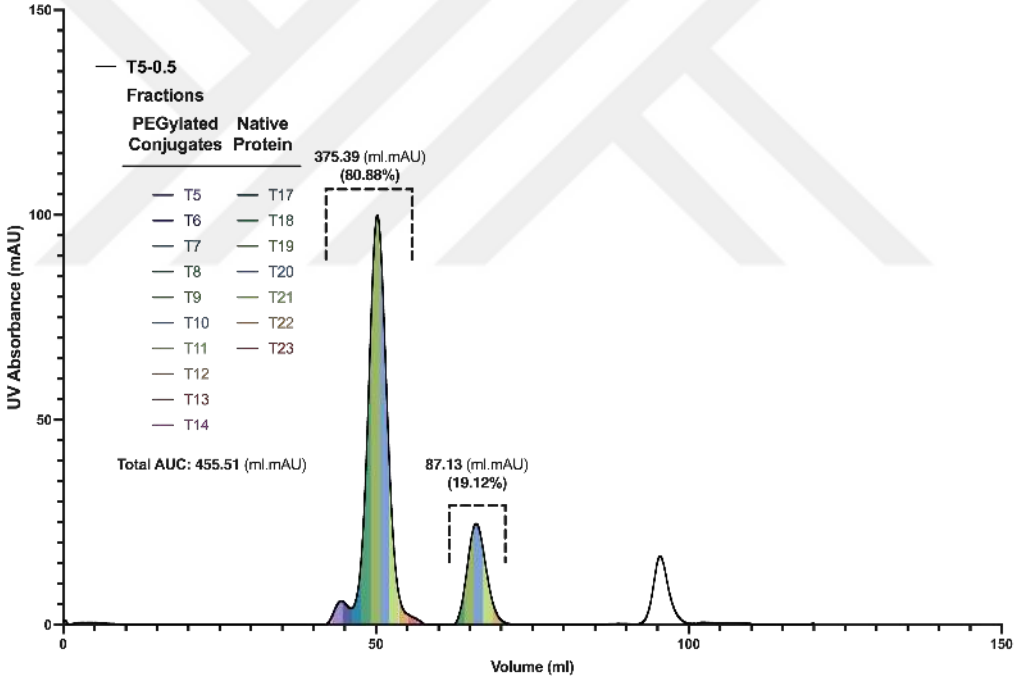

Figure 4.2: SEC profile for thiol-selective PEGylation with 5 kDa mPEG-maleimide at low feed (T5-0.5).

The earlier, broader peak corresponds to PEGylated IL-1Ra; the later, narrower peak corresponds to native protein. Colored overlays indicate collected fractions used for downstream analyses.

SDS-PAGE of the collected fractions confirmed these findings (**Figure *4.3***). PEGylated species appeared as a distinct band at ~27 kDa, consistent with the expected shift for the

addition of a 5 kDa PEG chain, while the later fractions contained only the unmodified protein at ~17 kDa. No evidence of multiple distinct PEGylated states was observed, supporting the conclusion that thiolation with 5 kDa PEG yields a single, well-defined conjugate species.

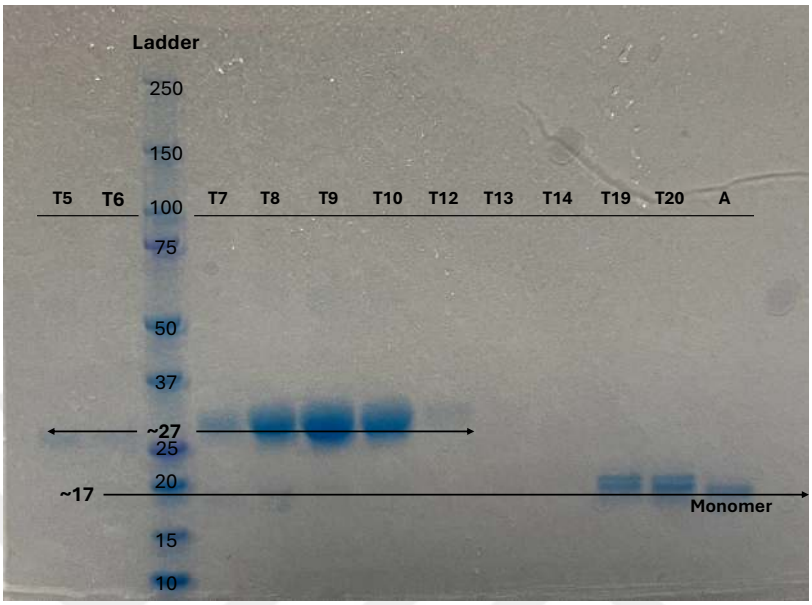

Figure 4.3: SDS–PAGE of T5–0.5 thiol-selective PEGylation fractions.

Lanes T5–T14 contain a single PEGylated IL-1Ra band at higher apparent mass than the monomer; T19–T20 and A (Anakinra as reference) show unmodified protein. The gel confirms clean enrichment of one PEGylated species, well separated from native IL-1Ra.

PEGylation with 10 kDa mPEG-mal was analyzed by SEC to assess the efficiency of conjugation and the relative distribution of modified and unmodified species (**Figure *4.4***). The chromatogram displayed a predominant PEGylated peak, representing 81.62% of the total protein, and a smaller peak corresponding to unmodified Anakinra, accounting for 18.38%. Hence, stepping from 5 to 10 kDa preserved the high level of conversion, and the PEGylated species continued to separate cleanly from the residual monomer.

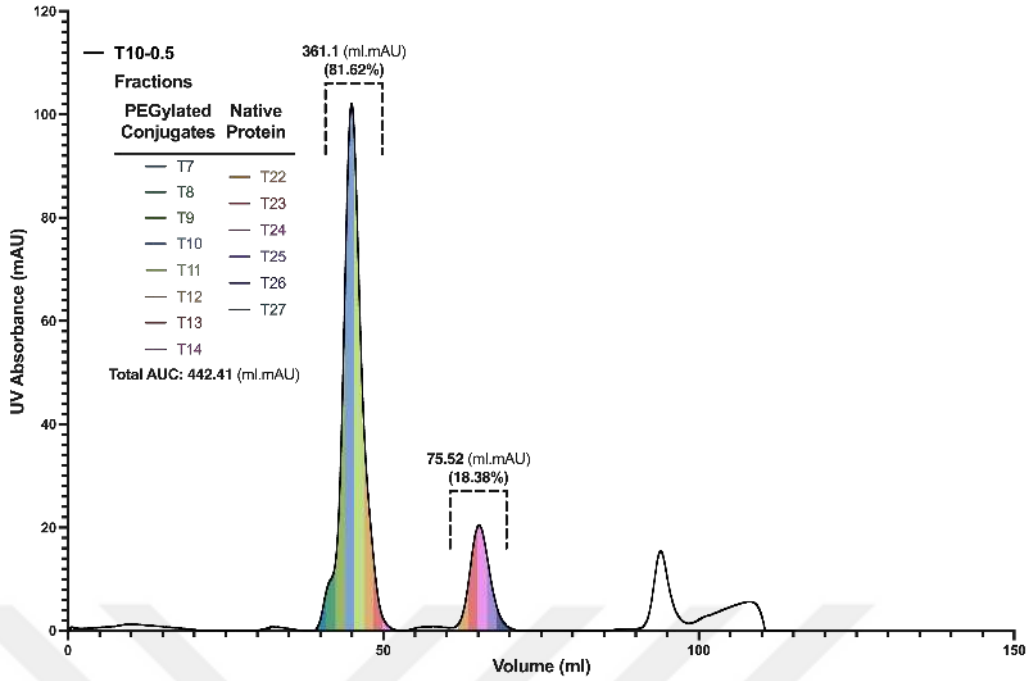

Figure 4.4: SEC profile for thiol-selective PEGylation with 10 kDa mPEG-maleimide at low feed (T10-0.5).

The earlier, broader peak corresponds to PEGylated IL-1Ra; the later, narrower peak corresponds to native protein. Colored overlays indicate collected fractions used for downstream analyses.

SDS-PAGE analysis of the collected fractions confirmed this profile (**Figure *4.5***). Earlier-eluting fractions (T7–T14) contained strong PEGylated bands migrating at ~37 kDa, in agreement with the expected shift for di-PEGylated Anakinra. Later fractions (T23–T24) showed only the unmodified protein band at ~17 kDa, consistent with the minor monomeric peak observed by SEC. The absence of multiple distinct PEGylated bands further supports the conclusion that 10 kDa thiolation favors the formation of a single, well-defined conjugate species.

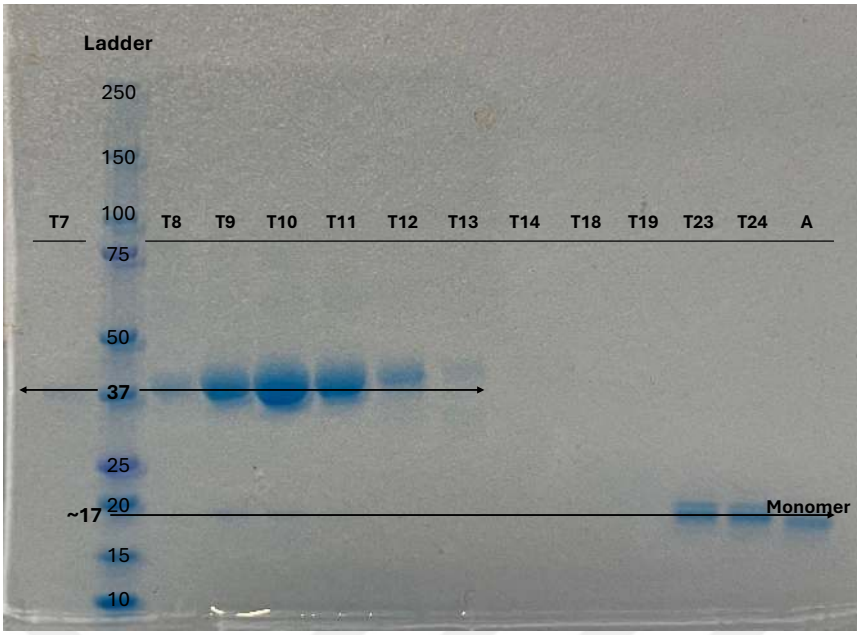

Figure 4.5: SDS–PAGE of T10–0.5 thiol-selective PEGylation fractions.

Lanes T7–T13 show a single PEGylated IL-1Ra band at higher apparent mass than the monomer; later lanes (T23, T24, A (Anakinra as reference)) contain unmodified protein. The gel indicates a clean, well-separated PEGylated species.

Thiol-selective PEGylation of Anakinra with 20 kDa mPEG-mal was assessed by SEC to evaluate conjugation efficiency and product distribution (**Figure *4.6***). The chromatogram showed two dominant peaks: an earlier-eluting PEGylated population accounting for 37.07% of the total protein and a later peak corresponding to unmodified protein at 62.93%. PEGylation was therefore successful but remained only moderately efficient, resulting in a heterogeneous mixture.

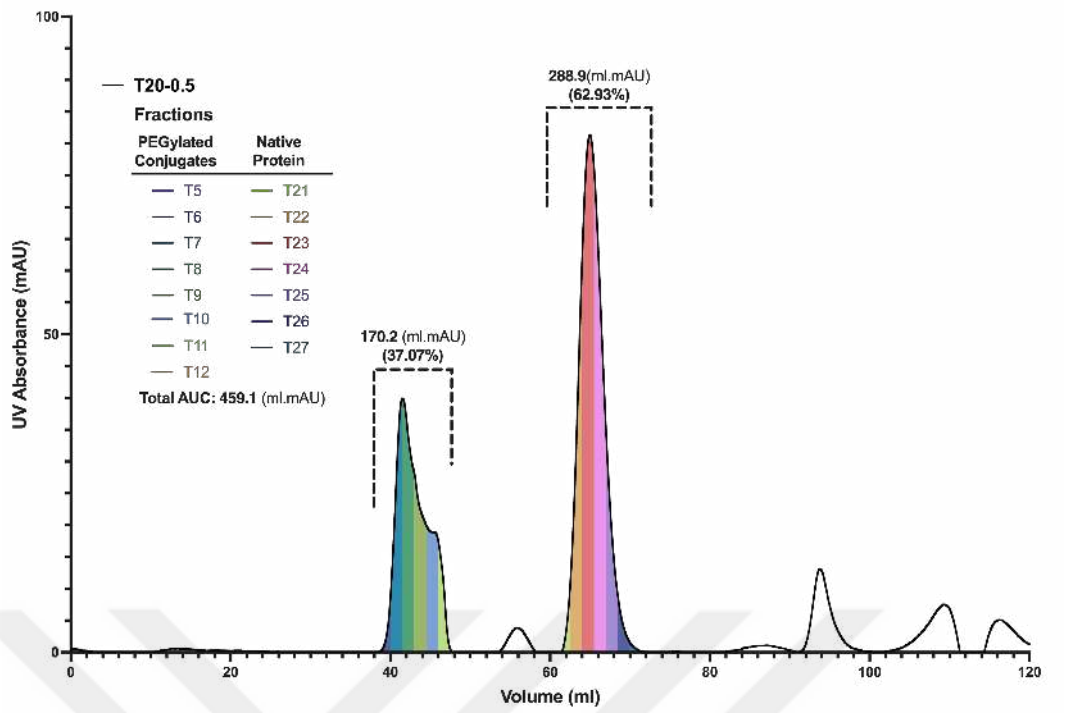

Figure 4.6: SEC profile for thiol-selective PEGylation with 20 kDa mPEG-maleimide at low feed (T20-0.5).

The earlier, broader peak corresponds to PEGylated IL-1Ra; the later, narrower peak corresponds to native protein. Colored overlays indicate collected fractions used for downstream analyses.

Fractions collected from SEC were analyzed by SDS-PAGE to confirm the molecular identity of PEGylated and unmodified species (**Figure *4.7***). The gel revealed a clear upward shift in molecular weight for PEGylated Anakinra, migrating at approximately 57 kDa, compared to the native form at ~17 kDa. Lanes corresponding to earlier-eluting SEC fractions (T6–T11) contained predominantly PEGylated protein, whereas later fractions (T22–T23) consisted almost exclusively of unmodified Anakinra.

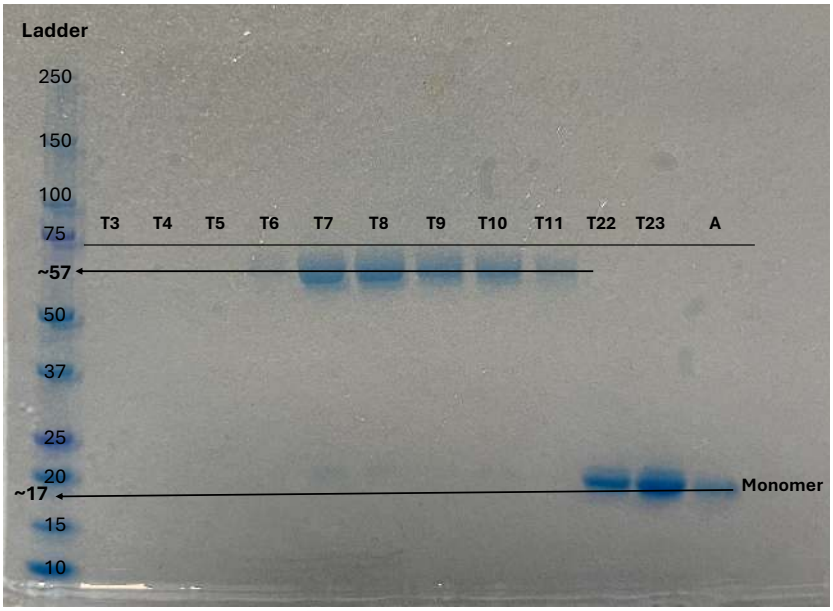

Figure 4.7: SDS–PAGE of T20–0.5 thiol-selective PEGylation fractions.

Lanes T6–T11 display a higher–apparent-mass band (PEGylated IL-1Ra), whereas T22–T23 and A (Anakinra as reference) contain unmodified protein. Compared with 5 and 10 kDa runs, the PEGylated band is weaker and broader, consistent with lower conversion at 20 kDa.

The relative efficiencies of thiolation with 5, 10, and 20 kDa mPEG-mal are summarized in **Table *4.2***. The data highlight a clear size-dependent trend: conjugation with 10 kDa and 5 kDa PEGs was highly efficient, yielding 81.62% and 80.88% PEGylated protein, respectively, whereas modification with 20 kDa PEG resulted in only 37.07% conjugation.

Table 4.2: Summary of thiol-selective PEGylation outcomes at a fixed PEG:IL-1Ra feed of 0.5 for 5, 10, and 20 kDa mPEG–maleimide.

The table reports the fraction of PEGylated conjugate recovered (from SEC integration), showing high conversion at 5–10 kDa and a marked drop at 20 kDa.

Sample No	Sample Key	Type of Reaction	MW of PEG (kDa)	PEG : IL-1Ra Molar Ratio	%PEGylated Conjugate	
1	T5-0.5	Thiolation	5	0.5	80.88	100
2	T10-0.5		10		81.62	
3	T20-0.5		20		37.07	0

4.2. Lysine-directed PEGylation (Non-specific PEGylation)

Lysine-targeted PEGylation was performed using methoxy-PEG-succinimidyl valerate (mPEG-SVA), which reacts with primary amines located on lysine side chains or the protein's N-terminus. This chemistry proceeds under mildly alkaline conditions (pH 7.5–8.5), where deprotonation of the ε-amino group increases its nucleophilicity, enabling covalent amide bond formation with the activated ester group of the PEG reagent. Unlike thiolation, which exploits a small number of cysteine residues, lysine-directed conjugation typically produces more heterogeneous mixtures due to the abundance and widespread distribution of lysines on the protein surface.

To visualize potential lysine-reactive sites within IL-1Ra, structural models were examined and rendered in PyMOL (Schrödinger, LLC) (**Figure *4.8***). IL-1Ra contains eight lysine residues (Lys10, Lys22, Lys46, Lys65, Lys72, Lys94, Lys97, Lys146). Inspection of the structure in the context of the receptor complex indicates that one lysine lies within—or immediately adjacent to—the receptor-binding interface, whereas Lys65, Lys94, Lys97, and Lys146 are solvent-exposed and thus most likely to be accessible for NHS-activated PEGylation under our conditions.

Consistent with these models, the remaining lysines are partially buried or situated near tight interdomain contacts, where steric constraints limit solvent access and are expected to reduce reactivity. This uneven accessibility provides a structural rationale for the broader conjugate distributions observed with lysine-directed PEGylation compared with thiol-selective (site-focused) chemistry.

The mapping of lysine residues therefore establishes the chemical and structural basis for non-specific PEGylation in IL-1Ra. These insights are consistent with experimental outcomes described in subsequent sections, where conjugate populations display broader distributions and reduced homogeneity relative to thiol-selective PEGylation.

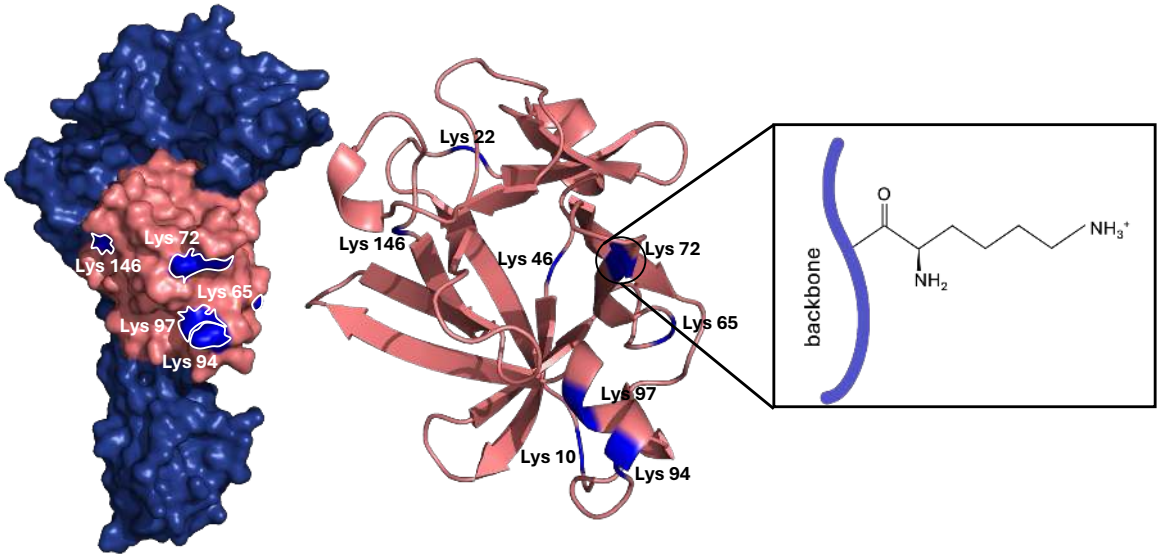

Figure 4.8: Structural map of solvent-exposed lysines on IL-1Ra.

The IL-1Ra surface/cartoon is shown with exposed lysines highlighted (Lys10, Lys22, Lys46, Lys65, Lys72, Lys94, Lys97, Lys146) on or near the receptor-facing face; IL-1R1 is rendered in dark blue for context. Inset: lysine ε-amine, the nucleophile for NHS-ester PEGylation.

To assess the effect of polymer size on lysine-directed conjugation, IL-1Ra was reacted with 5, 10, and 20 kDa mPEG-SVA reagents (**Table *4.3***). All reactions were carried out at a PEG:protein molar ratio of 0.5, chosen as a minimum condition to limit extensive multi-site modification while ensuring sufficient activated PEG for efficient reaction with surface-exposed lysine residues.

This ratio provided a consistent framework to evaluate the influence of PEG chain length on conjugation outcomes. Subsequent SEC and SDS-PAGE analyses were used to determine how the different PEG sizes affected efficiency and heterogeneity in the lysine-targeted setting, enabling direct comparison with the thiol-selective reactions.

Table 4.3: Experimental matrix for lysine-directed PEGylation.

IL-1Ra was reacted with mPEG–SVA of 5, 10, or 20 kDa at a fixed PEG:protein feed = 0.5, with products analyzed by SEC and SDS–PAGE.

Sample No	Sample Key	Type of Reaction	MW of PEG (kDa)	PEG : IL-1Ra Molar Ratio
1	**N5-0.5**	Nonspecific	5	0.5
2	**N10-0.5**		10	
3	**N20-0.5**		20	

Lysine-directed PEGylation of IL-1Ra with 5 kDa mPEG-SVA yielded a SEC profile with multiple distinct features (**Figure *4.9***). Three major PEGylated conjugate peaks were observed at earlier elution volumes, together accounting for ~36.22% of the total signal, while the later, dominant peak (63.46%) corresponded to unreacted IL-1Ra. Compared to the larger PEG conditions, the 5 kDa condition generated the broadest distribution of conjugates, reflecting the smaller steric footprint of the polymer, which allows access to a wider range of surface lysines. This broader accessibility results in a greater number of substitution states, evident from the multiple partially overlapping conjugate peaks.

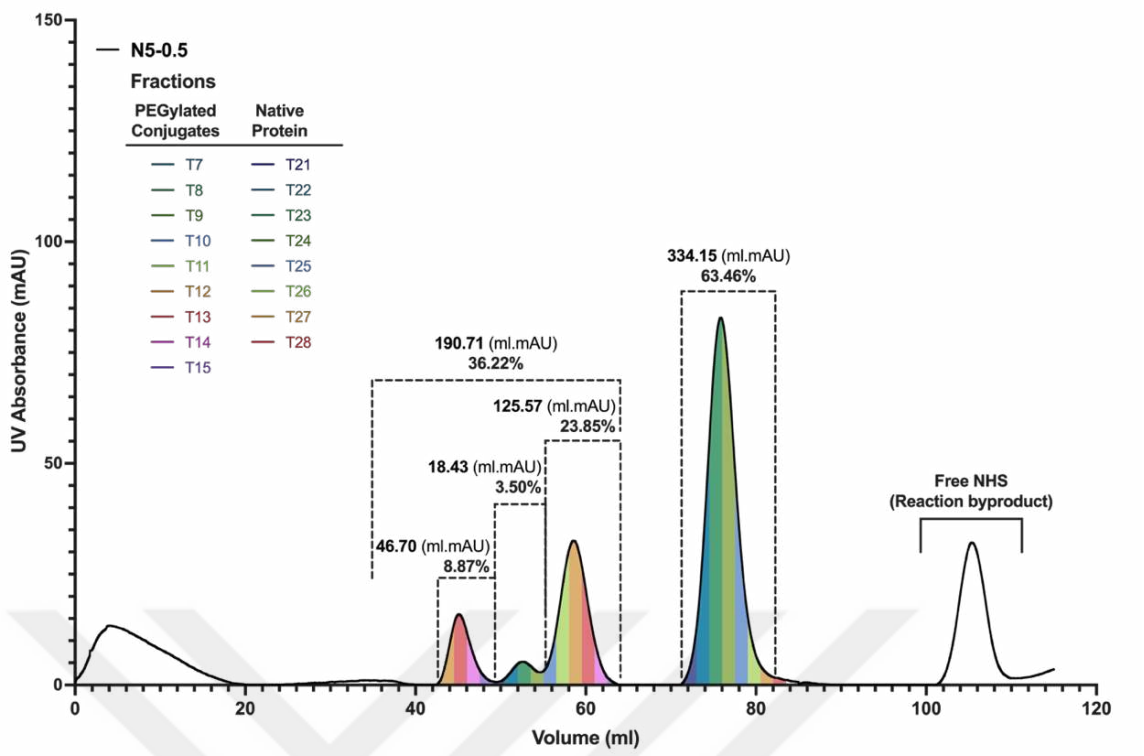

Figure 4.9: SEC profile for lysine-directed PEGylation with 5 kDa mPEG–SVA at low feed (N5–0.5).

Multiple earlier peaks indicate PEGylated IL-1Ra species with differing sites/degrees of modification; a later narrow peak corresponds to native protein, and a small peak near the total volume reflects free NHS by-product.

SDS-PAGE analysis of the collected fractions confirmed these observations (**Figure *4.10***). Fractions from the early SEC peaks resolved primarily at ~37 kDa and ~27 kDa, consistent with conjugates bearing approximately four (DoP ≈ 4) and two (DoP ≈ 2) PEG chains, respectively. The later SEC peak migrated at ~17 kDa, corresponding to unmodified IL-1Ra. Notably, the appearance of multiple well-defined conjugate bands indicates that 5 kDa PEG generates a wider spectrum of substitution states compared to the longer polymer conditions.

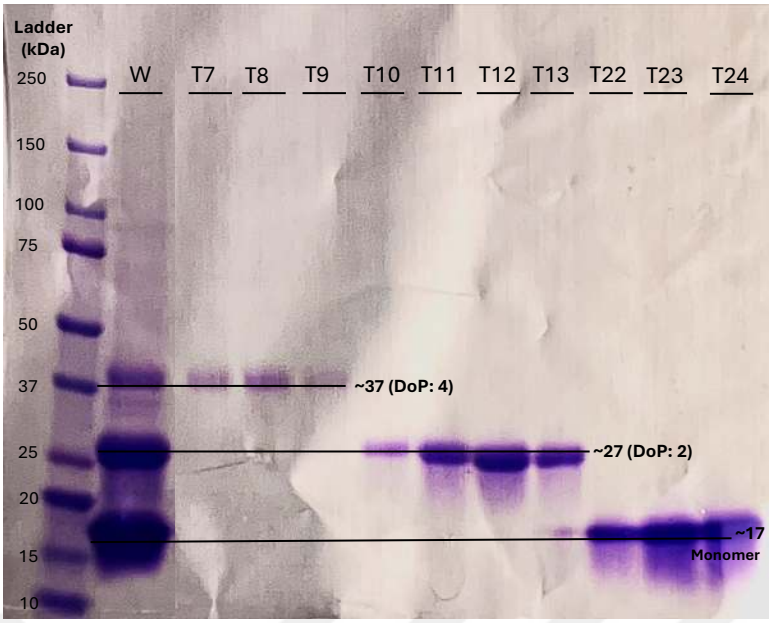

Figure 4.10: SDS–PAGE of N5–0.5 lysine-directed PEGylation fractions.

Early fractions (T7–T12) show two PEGylated bands (≈27 and ≈37 kDa), consistent with lower- and higher-DoP species; later fractions (T22–T24) contain unmodified IL-1Ra. The pattern indicates heterogeneous modification under lysine chemistry even at low feed.

Lysine-directed PEGylation of IL-1Ra with 10 kDa mPEG-SVA produced three main SEC features (**Figure *4.11***): two PEGylated conjugate peaks at earlier elution volumes (larger hydrodynamic species) followed by a later, major peak of unreacted IL-1Ra. The two PEGylated peaks were resolved from each other, indicating that 10 kDa PEG generated conjugates with different hydrodynamic radii to partially separate chromatographically—unlike the 20 kDa NHS reaction, where PEGylated species largely collapsed into a single steep SEC peak.

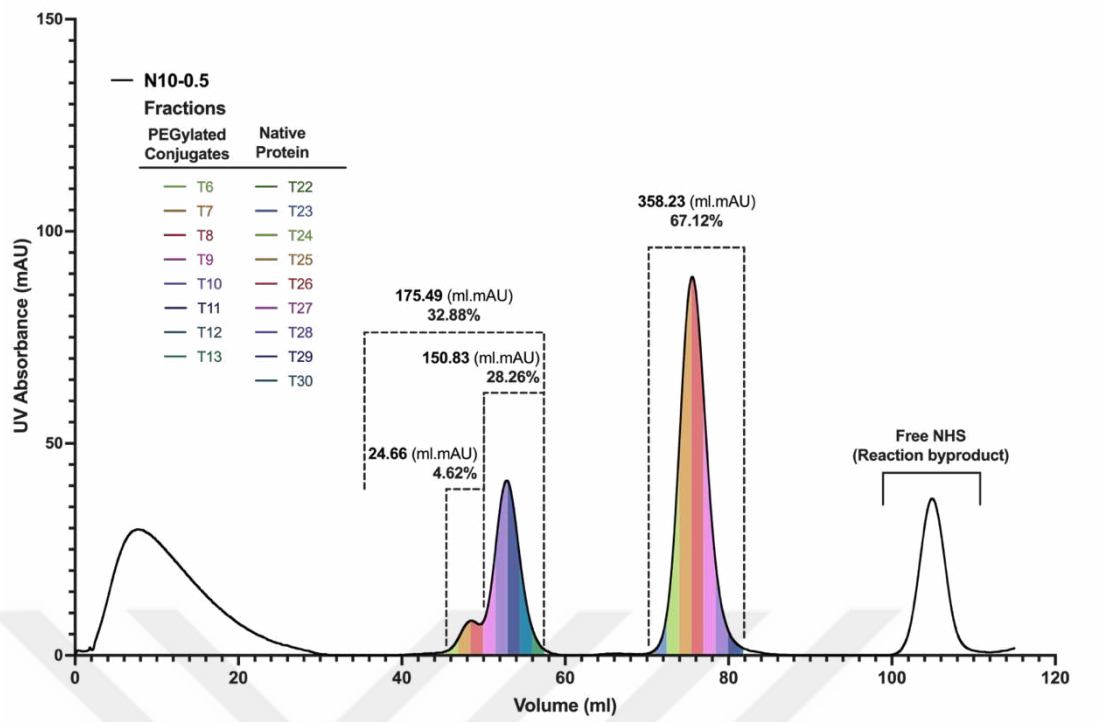

Figure 4.11: SEC profile for lysine-directed PEGylation with 10 kDa mPEG–SVA at low feed (N10–0.5).

Multiple earlier peaks indicate PEGylated IL-1Ra species with differing sites/degrees of modification; a later narrow peak corresponds to native protein, and a small peak near the total volume reflects free NHS by-product.

SDS-PAGE of the SEC fractions confirmed this assignment (**Figure *4.12***). Lanes corresponding to fractions from the first two (early) PEGylated peaks resolved at ~57 kDa and ~37 kDa, consistent with tetra-PEGylated (DoP ≈ 4) and di-PEGylated (DoP ≈ 2) conjugates, respectively. In contrast, lanes taken from the third, later SEC peak ran at ~17 kDa, matching native/unreacted IL-1Ra.

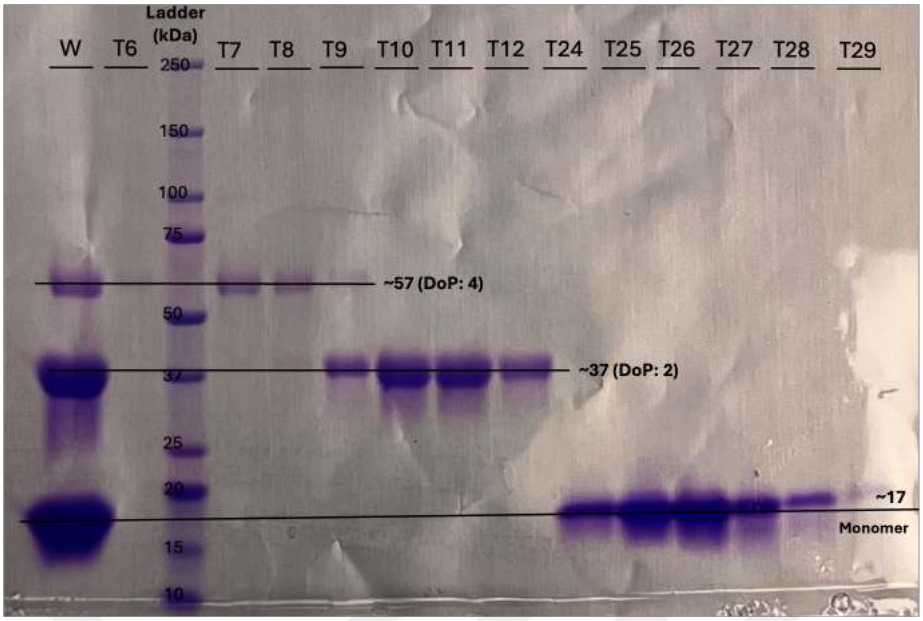

Figure 4.12: SDS–PAGE of N10–0.5 lysine-directed PEGylation fractions.

Early fractions (T7–T12) contain two PEGylated species (higher apparent masses consistent with lower- and higher-DoP conjugates), while later fractions (T24–T29) show unmodified IL-1Ra—illustrating heterogeneous modification under lysine chemistry at low feed.

Non-specific PEGylation of IL-1Ra with 20 kDa mPEG-SVA was analyzed by SEC to evaluate conjugation efficiency and product distribution (**Figure *4.13***). The chromatogram revealed two main peaks corresponding to PEGylated conjugates and unmodified protein. The PEGylated fraction accounted for 33.23% of the total area, whereas the majority of the protein (66.77%) remained unreacted. A smaller peak at later elution volumes was consistent with residual NHS ester hydrolysis byproducts. Compared to thiol-selective conjugation, the lower efficiency and broader distribution reflect the reduced selectivity of lysine-directed chemistry.

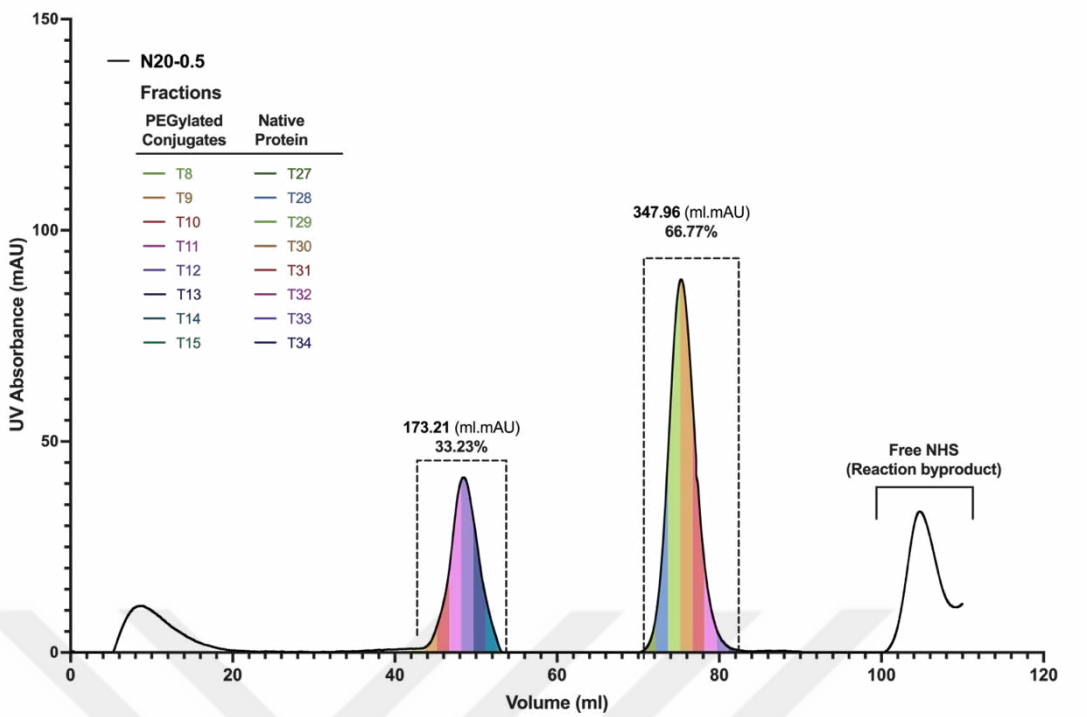

Figure 4.13: SEC profile for lysine-directed PEGylation with 20 kDa mPEG–SVA at low feed (N20–0.5).

Multiple earlier peaks indicate PEGylated IL-1Ra species with differing sites/degrees of modification; a later narrow peak corresponds to native protein, and a small peak near the total volume reflects free NHS by-product.

SDS-PAGE of the corresponding fractions further illustrated the heterogeneity (**Figure *4.14***). Multiple bands were observed at ~57 kDa and ~97 kDa, consistent with proteins carrying approximately two or four PEG chains, respectively. The presence of several distinct conjugate populations confirmed that multiple lysine residues were accessible to modification, resulting in higher degrees of substitution but with considerable variability. Unmodified protein was also evident as a strong band at ~17 kDa, consistent with the SEC profile showing a majority of the protein remaining unconjugated.

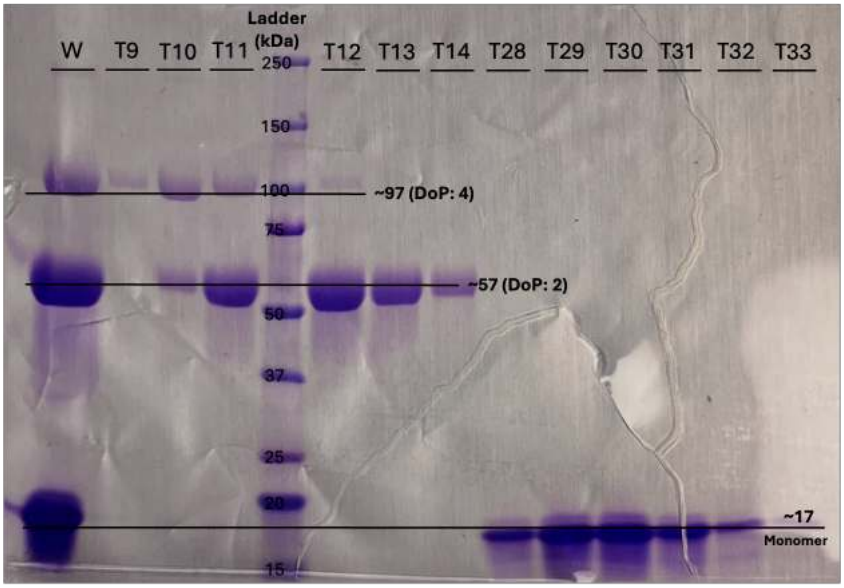

Figure 4.14: SDS–PAGE of N20–0.5 lysine-directed PEGylation fractions.

Early fractions show multiple higher–apparent-mass bands consistent with mixed degrees/sites of PEGylation, whereas later fractions contain mainly unmodified IL-1Ra. Compared with 5 and 10 kDa, the 20 kDa reaction displays weaker, broader PEGylated bands, indicating lower conversion and greater heterogeneity.

Although overall conjugation yields for 20 kDa PEG were similar between thiolation and lysine-directed reactions (37.07% vs 33.23%), the lysine-directed SEC trace presented as a single, steep PEGylated peak. SDS-PAGE, however, resolved this peak into at least two discrete conjugate bands. This apparent discrepancy reflects the different resolving principles of the two assays. SEC separates molecules by hydrodynamic radius, which at 20 kDa PEG is dominated by the polymer coil; conjugates with different degrees or positional sites of PEG attachment can therefore co-elute because their overall hydrodynamic sizes converge. By contrast, SDS-PAGE resolves proteins primarily by apparent molecular mass and thus exposes the underlying heterogeneity of the PEGylated population. Additional complexity arises from positional isomers across different lysines, both of which collapse into a single SEC peak while manifesting as multiple bands on the gel.

Together, the SEC and SDS-PAGE analyses highlight that lysine-targeted PEGylation with 20 kDa PEG proceeds with relatively low efficiency and produces heterogeneous conjugate populations. While the SEC suggested a relatively uniform PEGylated fraction, SDS-PAGE revealed the coexistence of multiple species with distinct degrees of modification, underscoring the greater complexity of non-specific conjugation pathways.

Despite the fact that the overall efficiency was comparable to the 20 kDa NHS reaction, the peak resolution of PEGylated species was greater with 10 kDa PEG. This likely reflects the smaller polymer's ability to access more lysines and to generate conjugates whose hydrodynamic sizes differ enough to separate by SEC; with 20 kDa PEG, the larger coil tends to mask positional/stoichiometric differences.

Taken together, these results suggest that while conjugation efficiency with 5 kDa PEG was comparable to the larger polymers, the heterogeneity of the resulting conjugates was markedly higher. The smaller polymer size not only enabled more lysines to be modified but also yielded multiple distinguishable populations of PEGylated species, producing a complex but resolvable distribution in both SEC and SDS-PAGE analyses.

Considering the molecular weight of PEG as a parameter, thiol-selective PEGylation (mPEG-maleimide) consistently yielded higher conjugation efficiency and cleaner, less heterogeneous products compared to lysine-directed PEGylation (mPEG-SVA) (*Table *4.4). In SEC, thiolation runs resolved into one dominant conjugate peak plus native protein, whereas lysine chemistry routinely yielded multiple, partially overlapping conjugate peaks (and corresponding multi-band patterns on SDS-PAGE at ~27 and ~37 kDa consistent with DoP ≈2 and ≈4). This lower heterogeneity with thiolation greatly simplified fraction selection and polishing, reduced material loss during SEC, and improved interpretability in downstream assays.

Table 4.4: Summary table of PEGylation outcomes at a fixed PEG:IL-1Ra feed = 0.5.

Thiol-selective reactions with 5–10 kDa mPEG gave the highest PEGylated fraction, with a drop at 20 kDa; lysine-directed reactions showed lower conversion across sizes. Percentages are from SEC peak integration.

Sample No	Type of Reaction	MW of PEG (kDa)	PEG : IL-1Ra Molar Ratio	%PEGylated Conjugate	
1	Thiolation	5	0.5	80.88	100
2		10		81.62	
3		20		37.07	
4	Nonspecific	5		36.22	
5		10		32.88	
6		20		33.23	0

4.3. Stoichiometric Ratio Optimization of PEG10 Thiolation

To further refine PEGylation conditions, a series of reactions were conducted with 10 kDa mPEG-maleimide across a range of PEG:protein molar ratios (1:2, 3:2, 6:2, 12:2, 18:2). The objective was to determine how increasing PEG availability influences conjugation efficiency, homogeneity, and the degree of PEGylation (DoP). Reactions were analyzed by size-exclusion chromatography (SEC) and SDS-PAGE (**Appendix Figure 9.1**), and the results were compiled in the summary table (**Table *4.5***).

SEC analysis revealed that near-stoichiometric ratios (0.5 and 1.5 molar folds) yielded the most favorable profiles. At 0.5, conjugation efficiency remained high (≈82%), and the elution pattern displayed a dominant, well-defined conjugate peak with minimal higher-order species. Increasing the ratio to 1.5 further improved conversion efficiency to ~88%, but the elution pattern suggested the onset of greater heterogeneity. At higher ratios (3, 6, and 9 molar folds), the efficiency plateaued (~88% at 3 molar folds) or declined markedly (to ~20% at 9 molar folds), with broadening of conjugate peaks and evidence of multiple overlapping species. These results highlight diminishing returns with excess PEG, as steric hindrance and over-modification reduce yield and complicate downstream separation.

Table 4.5: Effect of PEG:protein feed on thiol-selective PEGylation with 10 kDa mPEG–maleimide.

Near-stoichiometric feeds produce high recovery of a single, well-resolved conjugate; modest increases raise conversion but begin to blur SEC peaks; excessive feeds reduce useful yield and collapse chromatographic separability.

Sample No	Sample Key	Type of Reaction	MW of PEG (kDa)	PEG : IL-1Ra Molar Ratio	%PEGylated Conjugate	Clear Peak Separation	
1	T10-0.5	Thiolation	10	1 : 2	81.62	Yes	100
2	T10-1.5			3 : 2	88	Partial	
3	T10-3.0			6 : 2	87.84	No	
4	T10-6.0			12 : 2	30.81	No	
5	T10-9.0			18 : 2	19.61	No	0

SDS-PAGE analysis supported the SEC findings. At low ratios, discrete bands corresponding to di-PEGylated species dominated, with minimal higher-order conjugates. As the PEG excess increased, additional bands appeared at higher molecular weights (~57–77 kDa), indicative of tetra-PEGylated and higher substituted species. At extreme ratios (≥6 molar folds), conjugates became increasingly heterogeneous, and significant smearing was observed, reflecting uncontrolled multi-site PEGylation.

4.4. Stoichiometric Ratio Optimization on Nonspecific PEGylation

To refine PEGylation conditions, a series of reactions was conducted using 5, 10, and 20 kDa mPEG-SVA across a broader range of PEG:protein molar ratios (1:2, 3:2). The aim was to assess the impact of increased PEG availability on conjugation efficiency, homogeneity, and the degree of PEGylation (DoP). Reactions were analyzed using size-exclusion chromatography (SEC) and SDS-PAGE (**Appendix Figure 9.9**), with results compiled in the summary table (**Table *4.6***).

Table 4.6: Effect of PEG:protein feed on lysine-directed PEGylation with mPEG–SVA (5/10/20 kDa).

At 0.5 equivalents, conjugate recovery is modest with only partial SEC resolution; increasing to 1.5 raises overall PEGylation but collapses peak separation across sizes, consistent with broadened DoP/positional heterogeneity.

Sample No	Sample Key	Type of Reaction	MW of PEG (kDa)	PEG : IL-1Ra Molar Ratio	%PEGylated Conjugate	Clear Peak Separation
1	N5-0.5	Nonspecific	5	1 : 2	36.22	Partial
2	N10-0.5		10		32.88	Partial
3	N20-0.5		20		33.23	Yes
4	N5-1.5		5	3 : 2	68.51	No
5	N10-1.5		10		73.58	No
6	N20-1.5		20		74.38	No

100

0

At 0.5 eq (1:2), all three mPEG-SVA sizes (5, 10, 20 kDa) produced heterogeneous conjugate populations: SEC showed a single broad early-eluting "PEGylated" region and a later native-protein peak; SDS-PAGE of the conjugate fractions resolved multiple bands consistent with low degrees of PEGylation (≈DoP 2) and higher-order species (≈DoP 4 and above). Increasing the feed to 1.5 eq (3:2) raised overall conversion for each size but reduced chromatographic separability: the early SEC region broadened/merged, and gels showed enrichment of higher-DoP bands with a corresponding reduction of the lowest-DoP material. The effect was most pronounced for 20 kDa, where at 1.5 eq the conjugate distribution appeared unresolved by SEC with smeared high-mass bands on SDS-PAGE; 5 and 10 kDa remained fractionable but still exhibited co-elution of multiple DoPs. Collectively, at fixed chemistry, raising PEG:protein from 0.5 to 1.5 eq increases coupling but at the cost of homogeneity and peak resolution, with the loss of separability escalating with PEG size.

4.5. Clinical Framing of *In Vitro* Antagonism Experiments

To ground the *in vitro* analyses in physiologically meaningful conditions, reported serum ranges of IL-1β and IL-1Ra were collated across inflammatory states (**Figure *4.15***). In healthy individuals, circulating IL-1β is typically at or below 5 pg·mL^{-1} levels, while IL-1Ra resides in the low-hundreds pg·mL^{-1} range. Chronic inflammatory settings are characterized by modest elevations of IL-1β (tens to low-hundreds pg·mL^{-1}) accompanied by higher IL-1Ra (hundreds to low-thousands pg·mL^{-1}). Acute flares can

exhibit IL-1β above ~100–500 pg·mL^{-1} with IL-1Ra rising into the 2000–6000 pg·mL^{-1} interval. These strata provided the quantitative backdrop for selecting stimulus and antagonist levels in cell-based assays.

To correlate the *in vitro* measurements to clinically observed milieus, circulating concentrations of IL-1β and IL-1Ra across healthy, chronic, and acute inflammatory states are summarized in both mass (pg mL^{-1}) and molar (pM) units. Molar values were obtained by converting with the monomeric molecular masses ($MW_{IL\text{-}1\beta} \approx 17.1$ kDa and $MW_{IL\text{-}1Ra} \approx 17.3$ kDa). Use of pM is necessary for subsequent comparisons, as the antagonists evaluated—native proteins and PEGylated conjugates—differ in molecular weight; molar units therefore permit like-for-like interpretation of dose and potency.

IL1β	Healthy	Chronic	Acute		
pg/ml	5	20	100	200	500
pM	0.3	1	6	12	30
IL-1Ra	Healthy	Chronic	Acute		
pg/ml	200	500	2000	3000	6000
pM	11	29	115	173	347

Figure 4.15: Reference ranges for serum IL-1β and IL-1Ra under healthy, chronic, and acute inflammatory conditions shown in pg mL^{-1} (upper row) and the corresponding pM (lower row).

Conversions assume ~17.1 kDa for IL-1β and ~17.3 kDa for IL-1Ra and are used throughout to enable molar comparisons between native and PEGylated antagonists.

Accordingly, IL-1β challenge concentrations were chosen to span the upper healthy through acute-inflammation window, ensuring activation robust enough for comparative antagonism without inducing nonspecific toxicity. Antagonist titrations (Anakinra, M143V, and their PEGylated conjugates) were then expressed in picomolar units and tested over a wide, logarithmic range that maps onto physiological and pharmacological IL-1Ra exposures. This design enables interpretation of IC_{50}/IC_{80} shifts under clinically relevant cytokine conditions and facilitates direct comparison of native and PEG-modified constructs.

4.6. IL-1β Dose–Response in HEK-Blue™ IL-1β Cells (EC Benchmarks, pg mL^{-1} and pM)

A complete IL-1β activation series was acquired in HEK-Blue™ IL-1β cells using the QUANTI-Blue™/SEAP readout and fitted with a four-parameter logistic (4PL) model.

The resulting curve displays the expected sigmoidal form with a low, flat baseline at sub-threshold doses, a steep mid-region spanning roughly one log unit of concentration, and a well-defined plateau at high doses. Replicates clustered tightly around the fit over the dynamic range, indicating good assay precision and minimal well-to-well variability.

Potency landmarks are annotated in **Figure *4.16***. The EC_{50} value was obtained directly from the 4PL fit in the analysis software, whereas EC_{80} and EC_{90} were calculated from that fit using the fractional-effect relation described in Methods. Values are displayed in both mass (pg mL^{-1}) and molar (pM) units to preserve clinical interpretability while enabling molar comparisons across antagonists of different molecular weights. In all subsequent inhibition experiments, IL-1β was challenged at the **EC_{80}** level from this curve, which offers a high signal-to-noise plateau while preserving headroom to detect right-shifts in the presence of antagonists; this choice also stabilizes IC value estimation from 4PL fits. The derived potency landmarks were consistent with the manufacturer-provided IL-1β dose–response reference for this cell line, confirming that our assay conditions reproduced the expected activation profile.

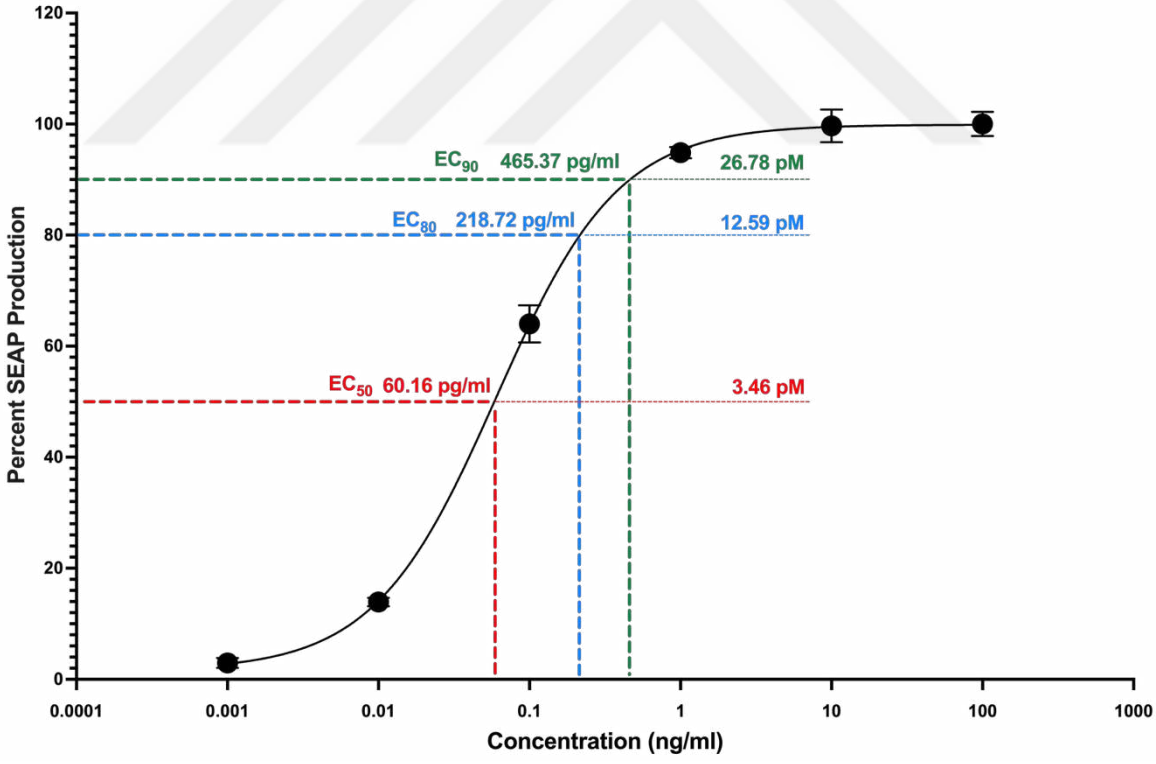

Figure 4.16: IL-1β stimulation curve in HEK-Blue™ IL-1β cells.

SEAP production was measured across an IL-1β concentration series and fit with a four-parameter logistic model to define EC_{50}/EC_{80}/EC_{90}. The EC_{80} value (dashed blue line) was used as the challenge dose for antagonist dose–response experiments.

4.7. Cell Viability Assay for PEGylated Conjugates

To ensure that the concentrations selected for comparative inhibition were not intrinsically cytotoxic, HEK-Blue™ IL-1β cells were incubated for 24 h with each antagonist in the absence of IL-1β, and metabolic activity/viability was assessed by MTT (mitochondrial reductase readout). The panel comprised Anakinra (A) and PEGylated derivatives prepared by lysine-directed coupling (N5, N10, N20) or thiol-selective coupling (T5, T10). All samples were tested over the same range used in the reporter assays (0.25–5035 pM; 0.02–400 × the IL-1β EC_{80} determined for this cell line; **Figure *4.17***). Results are shown as percent metabolic activity relative to untreated cells; a dashed line at 70% denotes the pre-specified threshold for proceeding to functional testing.

Across the full dose series, none of the antagonists produced an overt loss of viability. Thiol-selective conjugates (T5, T10) and the higher-MW lysine conjugates (N10, N20) generally maintained ≥ ~80% activity throughout. Anakinra and N5 displayed a mild downward drift at the highest concentrations, yet values remained close to or above the 70% criterion and did not follow a monotonic, concentration-dependent decline. Modest elevations at the lowest doses—seen for several conjugates—are a common feature of MTT measurements and most likely reflect subtle shifts in mitochondrial redox activity rather than proliferation.

Taken together, these data indicate that Anakinra and all PEGylated derivatives can be applied to HEK-Blue™ IL-1β cells at 0.25–5035 pM without confounding cytotoxicity. The same concentration window was therefore carried forward to the QUANTI-Blue™ assays for head-to-head comparison of inhibitory performance under viability-permissive conditions.

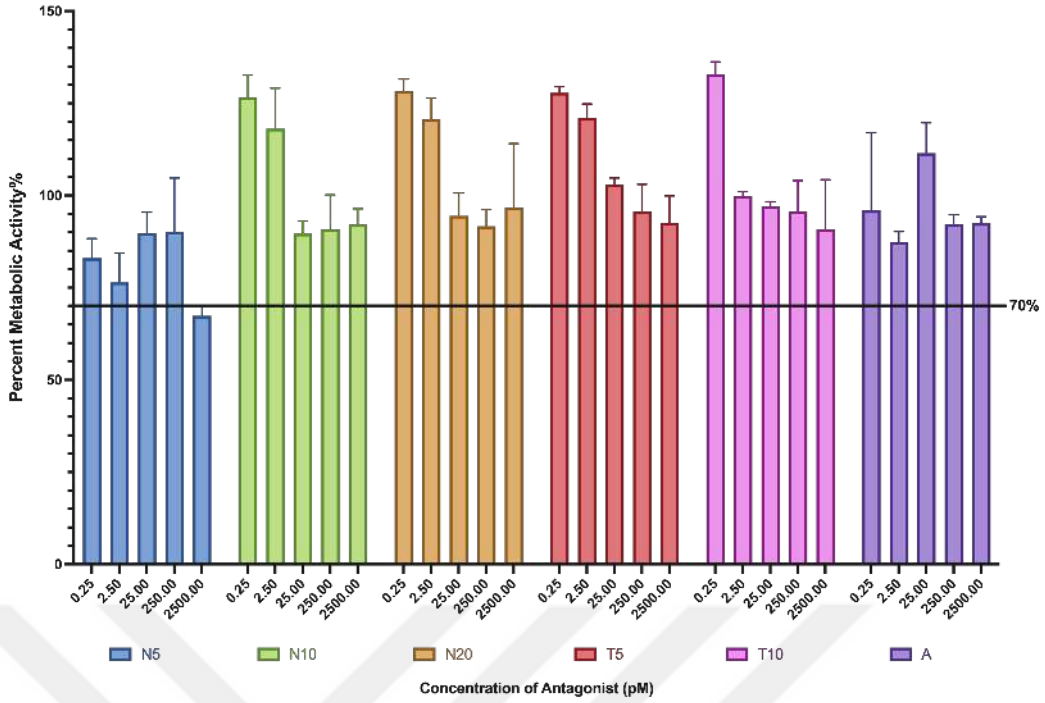

Figure 4.17: Cell viability under antagonist treatments.

MTT assay in HEK-Blue™ IL-1β cells shows no concentration-dependent cytotoxicity across native anakinra (A) and PEGylated variants (T5, T10, N5, N10, N20); the 70% line marks the standard viability threshold.

4.8. Cell Culture on HEK-Blue IL-1β Cells: Antagonist Performance (IC_{50}, IC_{80}, and IC_{90})

Dose–response curves for Anakinra (A) and thiol-PEG conjugates (T5-A, T10-A) were generated at a fixed IL-1β EC80 and fit with a 4-parameter logistic model. Top and Bottom plateaus converged for all curves, indicating full dynamic range. Native A produced a steep, left-shifted inhibition curve with $IC_{50} \approx 16$ pM (**Figure *4.18***). Both T5-A and T10-A showed right-shifted sigmoids of similar slope and unchanged maxima, with $IC_{50} \approx 4.2\times10^{2}$ pM for each. At higher effect levels, $IC_{80} \approx 1.75$ nM (T5-A) and 1.48 nM (T10-A); $IC_{90} \approx 4.06$ nM (T5-A) and 3.10 nM (T10-A).

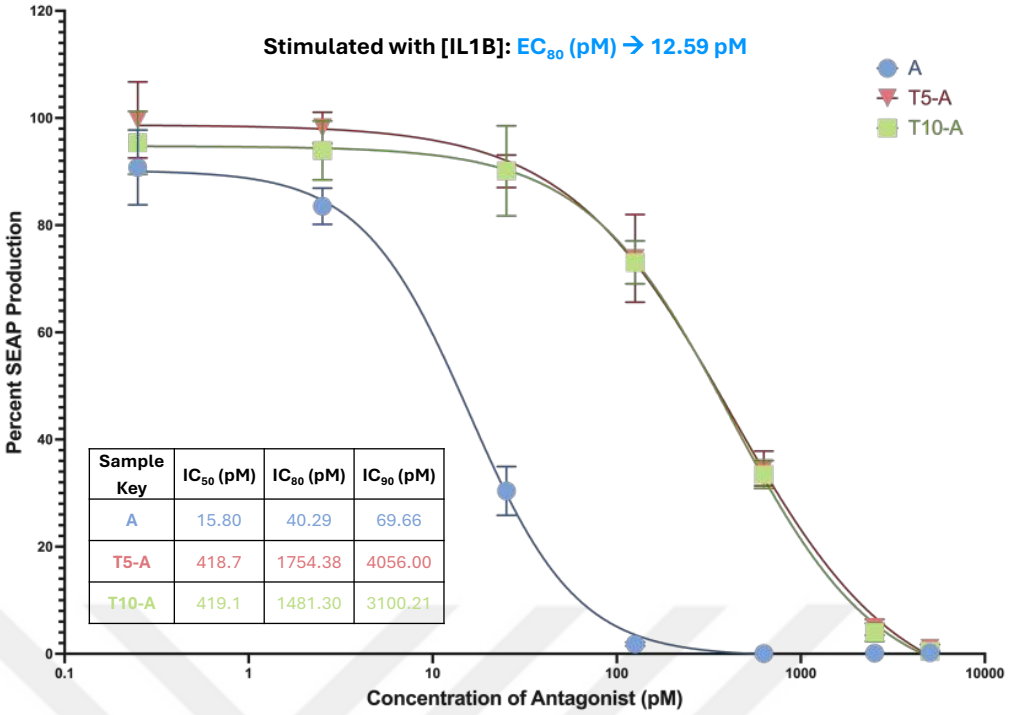

Figure 4.18: Dose–response of anakinra (A) versus thiol-PEG conjugates (T5-A, T10-A) in the HEK-Blue™ IL-1β assay.

Curves were fit with a 4-parameter logistic model at a fixed IL-1β EC80 stimulus; PEGylated variants retain full efficacy but are right-shifted relative to A. Error bars denote mean ± SD; inset lists fitted IC_{50}/IC_{80}/IC_{90}.

Using the same EC80 challenge and fitting procedure, native A again yielded a steep, left-shifted curve. All three NHS–PEG conjugates preserved maximal inhibition but were right-shifted. Estimated potencies were $IC_{50} \approx 15.8$ pM (A), 268.3 pM (N5-A), 224.0 pM (N10-A), and 744.1 pM (N20-A). At higher effect levels, IC_{80}/$IC_{90} \approx 753.8$/1379.4 pM (N5-A), 627.9/1147.4 pM (N10-A), and 2612.0/5444.8 pM (N20-A). Hill slopes were similar across curves (**Figure *4.19***).

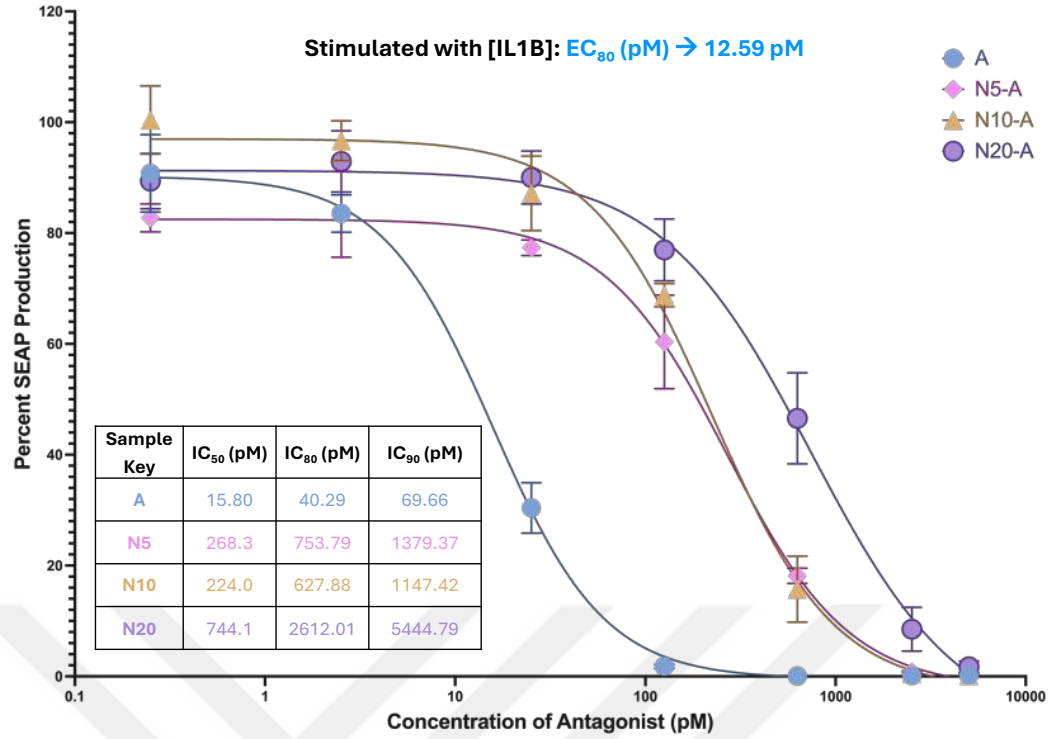

Figure 4.19: Dose–response of anakinra (A) versus NHS-PEG conjugates (N5-A, N10-A, and N20-A) in the HEK-Blue™ IL-1β assay.

Curves were fit with a 4-parameter logistic model at a fixed IL-1β EC80 stimulus; PEGylated variants retain full efficacy but are right-shifted relative to A. Error bars denote mean ± SD; inset lists fitted IC_{50}/IC_{80}/IC_{90}.

4.9. Labeled Synthesis of Mutant IL-1Ra (M143V) and its Biopyhsical Characterizations

All protein used in this chapter was expressed from the pDEST14-IL1RA-M143V-histag vector. The construct encodes the M143V variant under T7 control and carries a C-terminal 6×His tag for affinity purification together with the ampicillin-resistance cassette and bacterial origin of replication. A complete plasmid map with feature annotations is provided in the Methodology (see Methods, **Figure *3.6***). This vector served as the sole source of recombinant protein for all subsequent expression, purification, isotope labeling, and PEGylation workflows described below.

4.10. Structural Modeling of M143V Using AlphaFold2

To assess the potential structural impact of the M143V mutation introduced into IL-1Ra, the predicted three-dimensional structure of M143V was generated using AlphaFold2 (**Figure *4.20***-A). The model exhibited uniformly high confidence across the structured regions, with most residues scoring a pLDDT > 90, indicative of very high model

reliability. The residue at position 143, which was mutated from methionine to valine, is located in a highly confident region of the model, suggesting that the substitution is unlikely to destabilize the local fold.

To evaluate whether the mutation leads to any substantial structural rearrangements, a comparative structural alignment was performed between the recombinant wild-type IL-1Ra (PDB ID: 1IRP) and the predicted M143V variant (**Figure *4.20***-B). The global superimposition revealed no significant deviation in overall conformation between the two structures. The mutated residue is shown in red for the wild-type methionine and in deep blue for the substituted valine, highlighting the localized nature of the change. These results support the notion that the M143V substitution does not perturb the native fold of IL-1Ra and is structurally well tolerated.

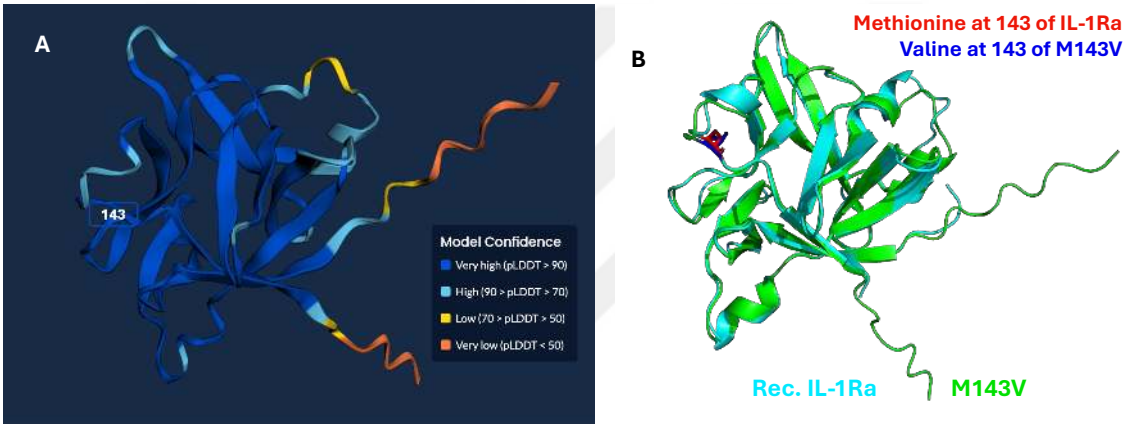

Figure 4.20: Structural context of the M143V substitution in IL-1Ra.

(A) Predicted IL-1Ra fold colored by pLDDT confidence with residue 143 indicated. (B) Superposition of recombinant IL-1Ra (teal) and M143V (green) highlights the Met→Val side-chain change with no apparent global backbone deviation.

Additional metrics from the AlphaFold2 prediction, including the Predicted Aligned Error (PAE) and the per-residue predicted IDDT (pLDDT) score, are provided in **Appendix Figure *9.17-A*** and **Figure *9.17-B***. The PAE heatmap revealed uniformly low expected position errors across the structured core of the protein, while the pLDDT plot confirmed high local confidence (pLDDT > 90) for the majority of residues, including residue 143. These data collectively support the structural reliability of the M143V model used in this study.

4.11. Isotope-Labeled Protein Expression in M9 Medium and Purification of ^{15}M143V-IL-1Ra

To enable downstream 2D-HSQC NMR studies, the M143V variant of IL-1Ra was recombinantly expressed in minimal M9 medium supplemented with ^{15}N ammonium chloride as the sole nitrogen source to obtain uniformly ^{15}N-labeled protein. Following the expression, His-tag affinity purification was performed using a stepwise imidazole gradient to isolate the labeled protein.

As shown in the SDS-PAGE gel (**Figure *4.21***), the target protein, with an expected molecular weight of ~17 kDa, was successfully enriched in the elution fraction (E), corresponding to the 500 mM imidazole step. The load (L) and flowthrough (FT) lanes display multiple bands, reflecting the presence of host proteins prior to purification. Progressive washing with increasing imidazole concentrations (10–250 mM) helped reduce non-specific binding. The distinct band in the elution lane indicates efficient isolation of the monomeric M143V protein.

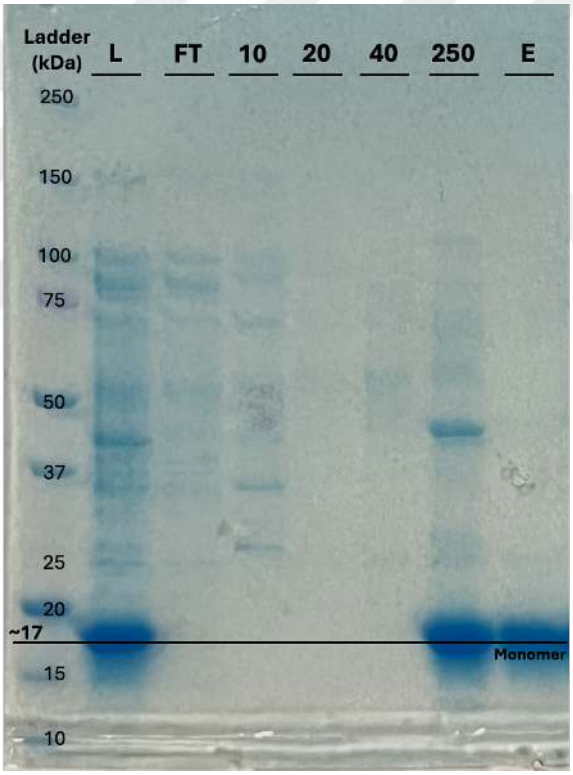

Figure 4.21: IMAC purification of ^{15}N-labeled M143V-IL-1Ra from M9 expression.

SDS–PAGE shows load (L), flow-through (FT), step imidazole elutions (10/20/40/250 mM), and the pooled eluate (E); the ~17 kDa band is enriched in the high-imidazole fraction, consistent with His-tag capture and recovery of the target protein.

To further purify the ^{15}N-labeled M143V protein obtained from His-tag affinity chromatography and ensure its suitability for structural NMR studies, the elution fraction

was subjected to size-exclusion chromatography (SEC). The separation was carried out using a Superdex 75 Increase 16/600 column equilibrated with phosphate-based buffer under reducing conditions, allowing resolution of the non-modified monomer and its potential dimeric conjugates based on their hydrodynamic radii.

The SEC chromatogram (**Figure *4.22***) revealed a dominant, symmetrical peak centered at approximately 72 mL, accounting for 98.08% of the total area under the curve (AUC), consistent with a well-behaved, monodisperse monomeric protein population (similar to Anakinra, see **Appendix Figure *9.15***). A minor earlier peak, representing 1.92% of the total AUC, was observed eluting near 58–65 mL and was tentatively assigned to a dimeric form based on elution volume (**Figure *4.22***). Notably, this minor population did not suggest significant aggregation or misfolding, but was instead likely reflective of a dynamic monomer–dimer equilibrium that can occur under native-like buffer conditions.

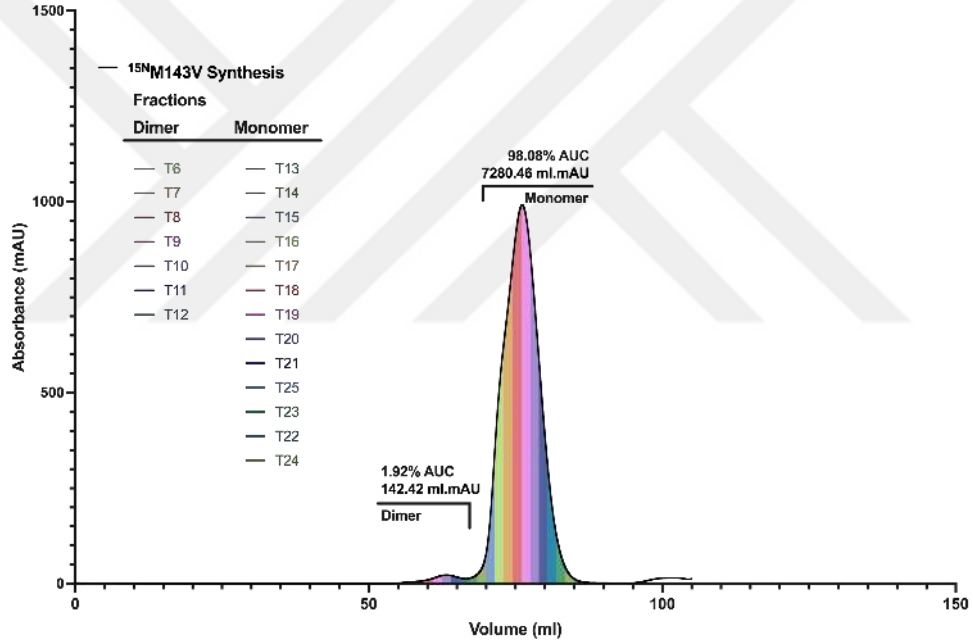

Figure 4.22: SEC of ^{15}N-labeled M143V-IL-1Ra following IMAC.

A dominant monomer peak is resolved from a small, earlier dimer peak; colored traces mark collected fractions (T6–T12, dimer; T13–T24, monomer).

To verify the molecular identity and purity of the fractions across the elution profile, SDS-PAGE analysis (**Figure *4.23***) was performed on selected SEC fractions spanning both the dimer-associated region (T10–T12) and the monomer peak (T14–T24). As shown in **Figure *4.23***, all analyzed fractions exhibited a strong and singular protein band around ~17 kDa, corresponding to the theoretical molecular weight of the M143V variant. Importantly, no additional higher- or lower-molecular-weight bands were detected in

either the monomer or dimer-associated fractions, indicating that the earlier-eluting species observed in the SEC profile do not represent stable oligomers or degradation products, but rather transient dimeric species that resolve as monomers under denaturing SDS-PAGE conditions. Monomeric fractions (T14–T24) were pooled and concentrated for downstream 2D-HSQC NMR analysis and subsequent PEGylation studies.

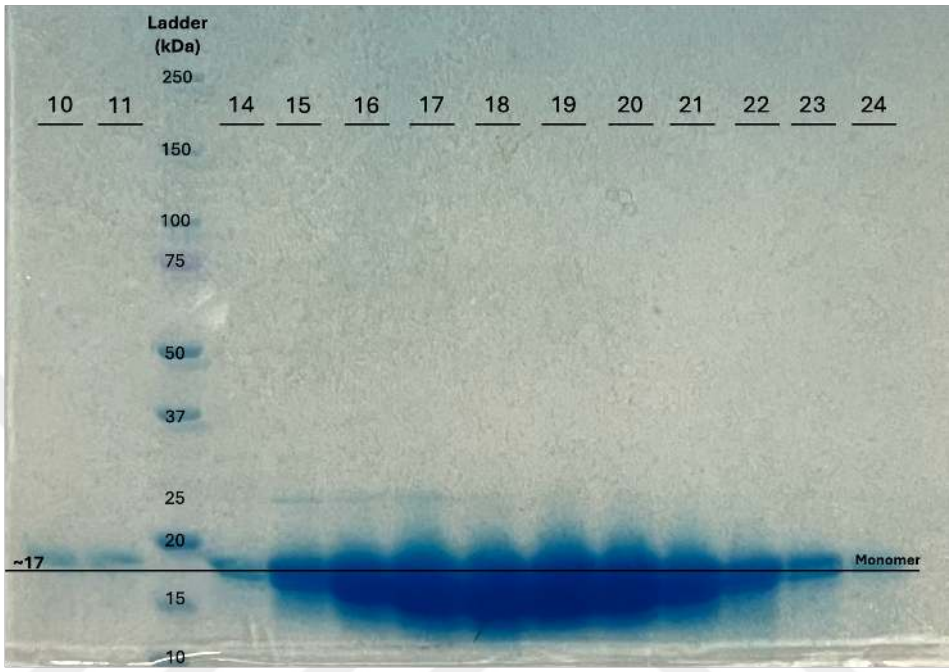

Figure 4.23: SDS–PAGE of SEC fractions from ^{15}N-M143V-IL-1Ra purification.

Fractions 10–24 show a single band at the expected monomer size, confirming the purity of the pooled monomer peak and effective separation from higher-molecular-weight species.

4.12. Thiol-selective PEGylation of ^{15}N-Labeled M143V for NMR Analysis

Following successful synthesis and purification of ^{15}N-labeled M143V, site-specific PEGylation was first performed using 10 kDa mPEG-maleimide, targeting the free thiol groups of engineered cysteine residues via thiol–maleimide conjugation chemistry. The reaction mixture was subsequently subjected to size-exclusion chromatography (SEC) to separate PEGylated conjugates from unmodified protein and reaction byproducts.

The resulting SEC profile revealed two distinct peaks (**Figure *4.24***). The first peak, eluting around 42–58 mL and constituting 81.51% of the total area under the curve (AUC), corresponded to higher molecular weight PEGylated species, while the second peak at 66–72 mL (18.49% AUC) matched the elution volume of unmodified M143V. Fractions collected across the first peak (T1–T12) were expected to contain PEG10-

M143V conjugates, whereas fractions T18–T25 were assigned to the remaining native (non-PEGylated) protein population.

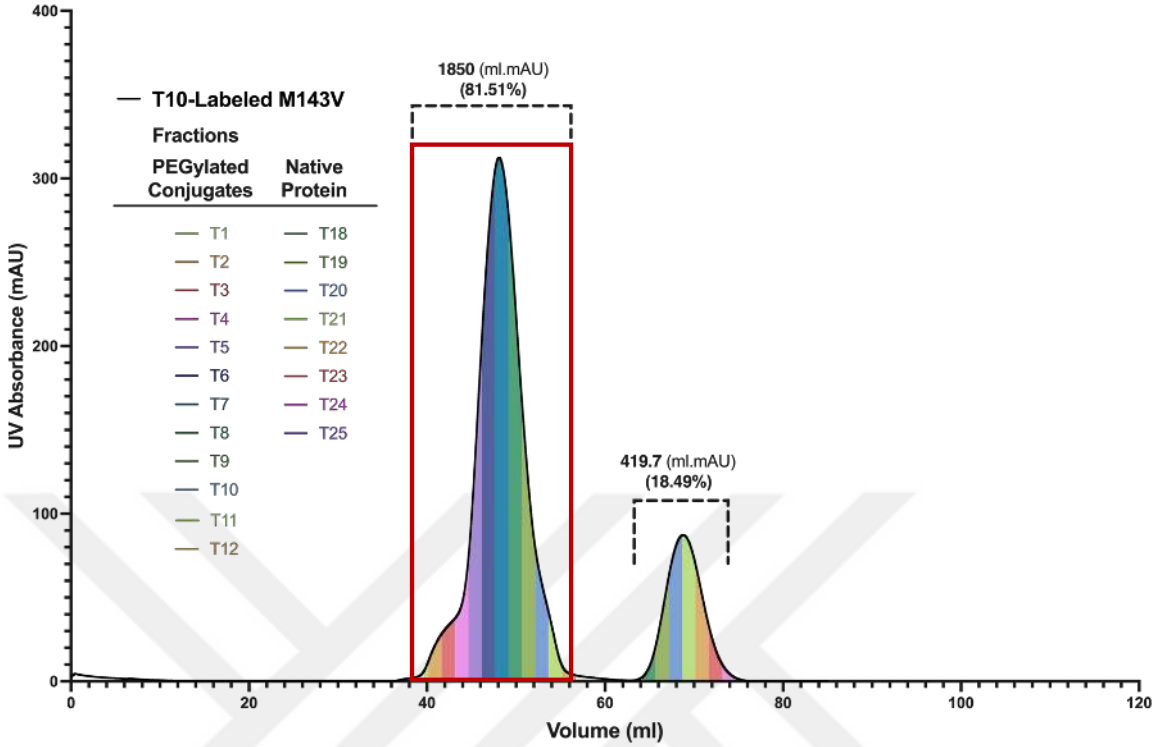

Figure 4.24: SEC profile of 10 kDa thiol-PEGylated M143V (T10–M143V).

The earlier, dominant peak corresponds to PEGylated conjugate; the later, smaller peak corresponds to unmodified protein. Colored overlays mark collected fractions (T1–T12, conjugate; T18–T25, native).

SDS-PAGE analysis of SEC fractions supported this interpretation (**Figure *4.25*Figure *4.26***). A pronounced band at approximately ~37 kDa was observed in fractions T6–T11, consistent with the expected size of di-PEGylated M143V (PEG10-M143V). This band appeared as a distinct upward shift compared to the ~17 kDa native M143V observed in both the pre-SEC and T18–T25 fractions. Importantly, no additional significant bands were visible in the PEGylated region, suggesting no side reactions or higher DoP values under the applied conditions.

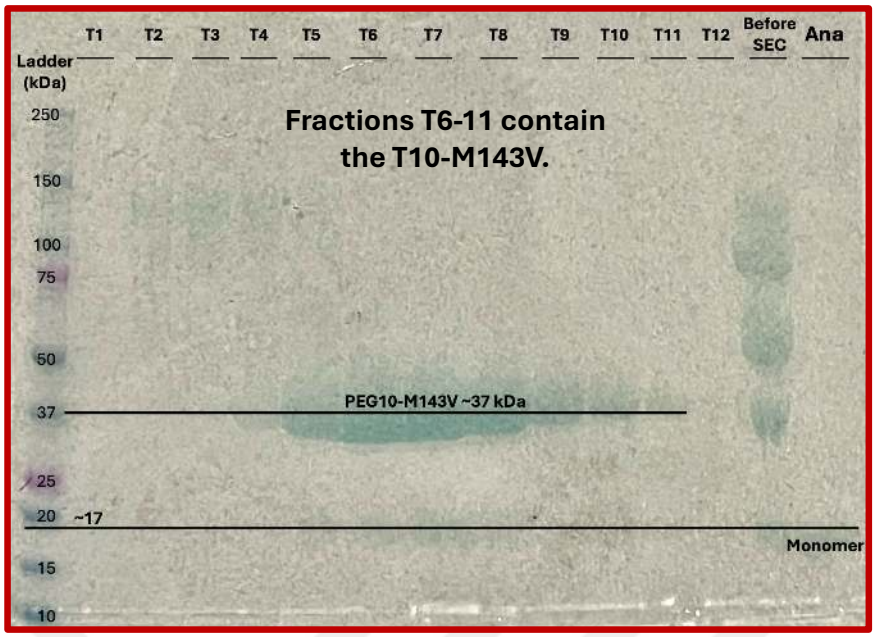

Figure 4.25: SDS–PAGE of SEC fractions from T10–M143V purification.

Fractions T6–T11 contain a single band at the expected ~37 kDa for the PEGylated conjugate, confirming isolation of a homogeneous di-PEGylated species; T1–T5 and T9–T12 contain trace or non-peak material.

In contrast, the second SEC peak (T18–T25) contained a single band at ~17 kDa, confirming the presence of unmodified M143V that remained in the reaction mixture. These results collectively demonstrate that site-specific PEGylation of ^{15}N-M143V was successful and selective, with efficient conjugate recovery and clean separation of PEGylated versus native species via SEC.

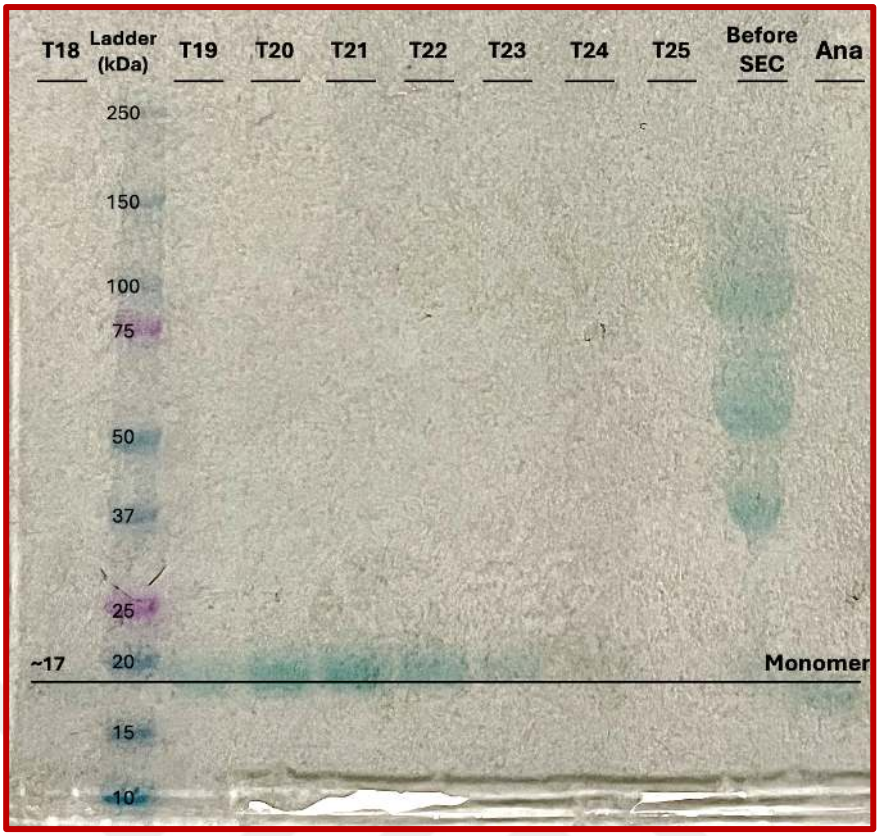

Figure 4.26: SDS–PAGE of late SEC fractions (T18–T25) from the T10–M143V run.

Lanes show a single ~17 kDa band consistent with unmodified M143V, confirming clean separation of native protein from the earlier PEGylated peak. “Before SEC” and “Ana” lanes are pre-purification and analytical controls.

Hence, fractions corresponding to PEG10-M143V (T6–T11) were pooled, concentrated, and used for subsequent NMR and functional characterization.

4.13. HSQC NMR of Labeled IL-1Ra Variants for Structural Characterization and PEGylation Site Mapping

To investigate the structural consequences of site-specific PEGylation on M143V, 2D $^{1}H–^{15}N$ HSQC NMR spectroscopy was performed using uniformly ^{15}N-labeled protein before and after conjugation with 10 kDa mPEG-maleimide.

Panel A of **Figure *4.27*** shows that the uniformly ^{15}N-labeled M143V produced a well-resolved 2D $^{1}H–^{15}N$ HSQC spectrum with cross-peaks dispersed across $\delta^{1}H \approx 6.5–10.5$ ppm and $\delta^{15}N \approx 105–135$ ppm. Peak intensities were even and signal-to-noise was high, with minimal crowding in the amide region. The number of observed resonances matched expectations for a monomeric IL-1Ra backbone amide set after excluding prolines and overlapped side-chain/solvent signals. Reference-guided assignments were obtained for

a large subset of peaks (labels shown), providing a baseline fingerprint for subsequent comparison.

Panel B of **Figure *4.27*** presents the HSQC of the SEC-purified 10 kDa-PEG conjugate (T10-M143V), which retained the same overall dispersion and peak quality seen for M143V. Most resonances appeared at positions close to the native spectrum, and no global line broadening or widespread peak loss was detected. The sample remained monodisperse under the acquisition conditions, as observed by narrow, symmetric line shapes. A small number of resonances displayed positional changes or splitting relative to ***Figure 4.27-A***.

Panel C of **Figure *4.27*** shows a direct overlay of the two spectra shows extensive coincidence of cross-peaks between M143V (red) and T10-M143V (blue), with a discrete subset exhibiting measurable chemical-shift differences. Notably, the resonance assigned to Cys70 resolved as two closely spaced peaks in the PEGylated sample, whereas a single peak was observed for the native protein. Notably, a small but significant shift in Cys117 was also observed. Aside from these localized differences, peak count and overall dispersion remained comparable between the two datasets.

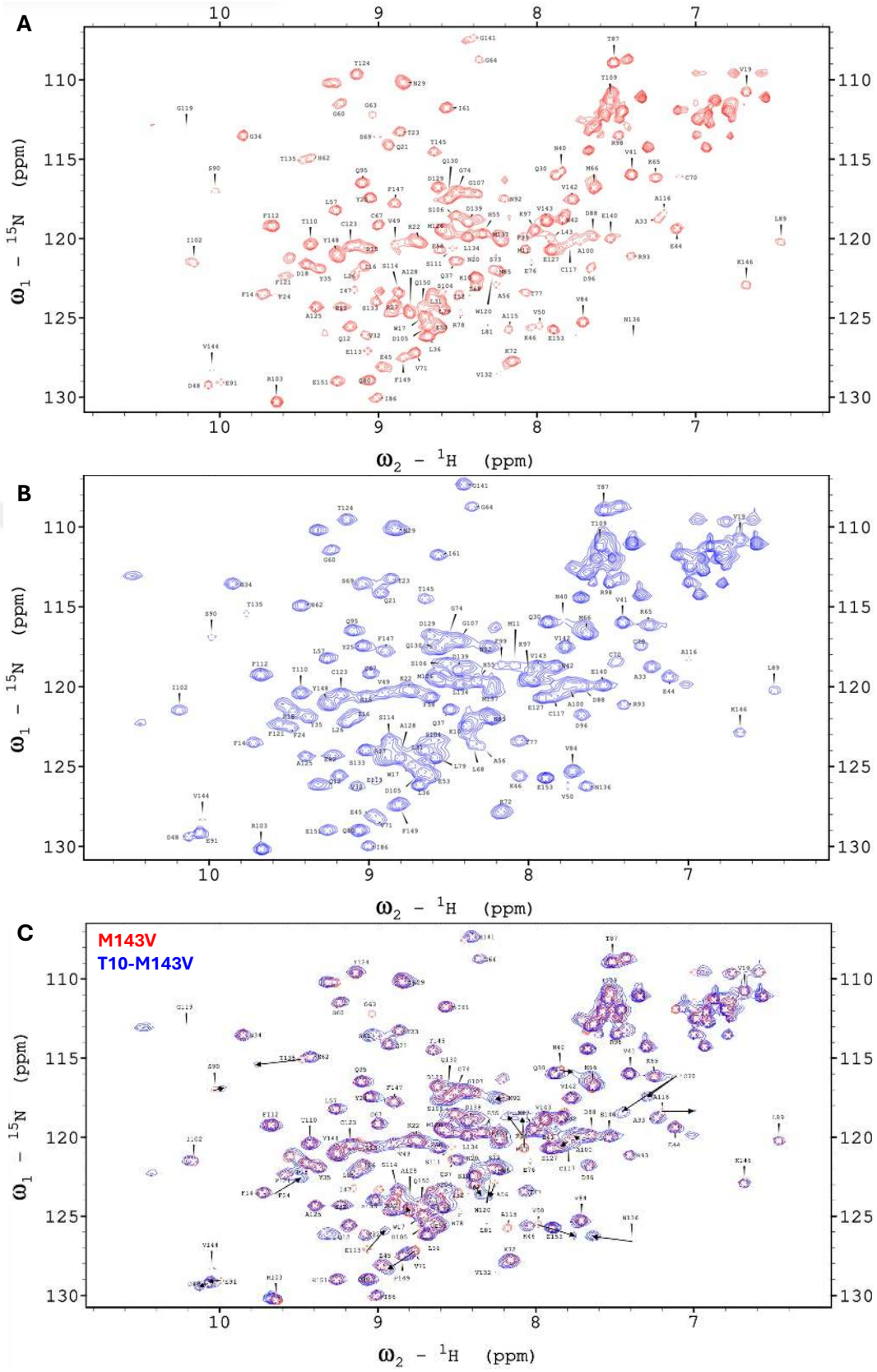

Figure 4.27: 2D $^{1}H–^{15}N$ HSQC spectra of IL-1Ra M143V and its PEG conjugate.

(A) M143V shows well-dispersed amide peaks consistent with a folded globular protein. (B) T10–M143V retains overall dispersion and peak count. (C) Overlay (M143V, red;

T10–M143V, blue); arrows mark residues with chemical-shift perturbations or peak splitting after PEGylation, indicating localized environmental changes while the global fold remains conserved.

4.14. Residue-Level Analysis of Structural Perturbation Induced by Thiol-selective PEGylation

Weighted CSP values (Δδ) were computed for assigned residues and plotted as a histogram with thresholds at 0.25, 0.40, and 1.00 ppm (**Figure *4.28***). The majority of residues fell below 0.25 ppm. A small subset exceeded the 0.40 ppm threshold, and only a few residues surpassed 1.00 ppm. The largest Δδ values included the signal assigned to Cys70; whereas the perturbation at Cys117 is calculated to be above 0.4 and considered significant.

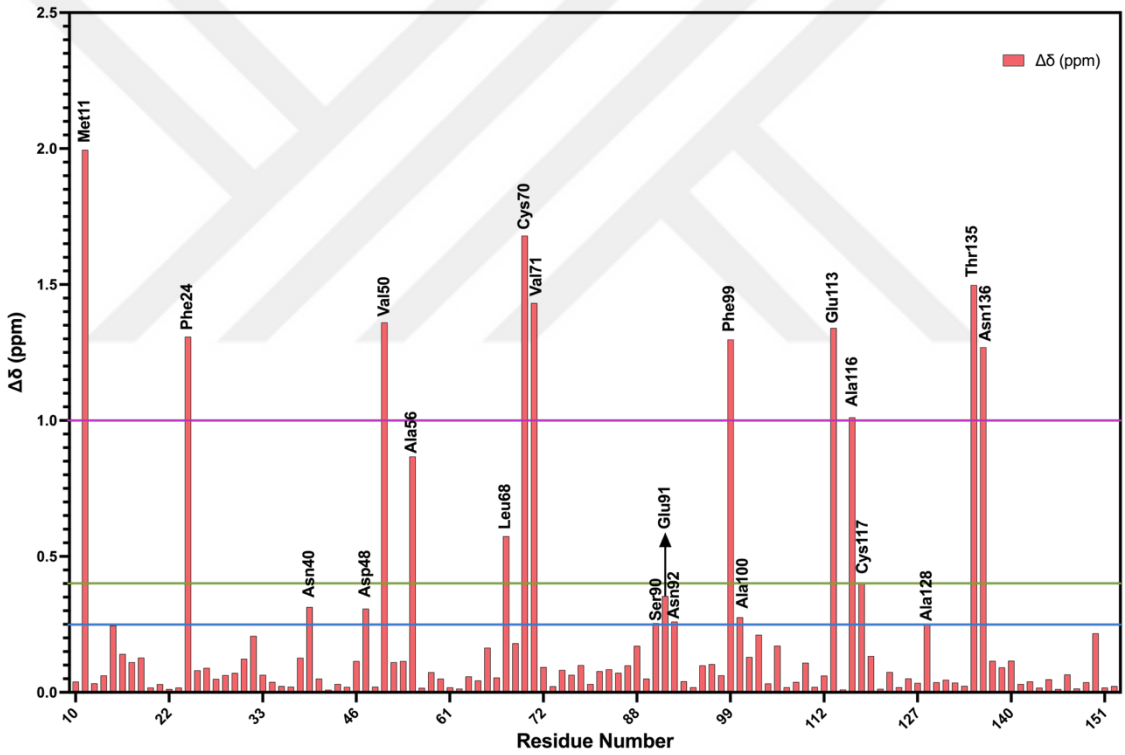

Figure 4.28: Chemical-shift perturbation (CSP) analysis of M143V before and after thiol-PEGylation.

Bars report residue-wise weighted Δδ; horizontal guides denote qualitative thresholds (mild/moderate/strong). Labeled residues exceed thresholds, and Cys70 shows peak splitting (two PEG-dependent peaks) rather than a single shift—consistent with localized effects near the modification site and preservation of the overall fold.

Residues were mapped onto the IL-1Ra structure and color-coded by CSP magnitude (**Figure *4.29***). Sites with $\Delta\delta \geq 0.25$ ppm were distributed across surface loops and selected β-strand/helix elements; strongly perturbed residues ($\Delta\delta \geq 1.00$ ppm) were limited in number and spatially discrete. No contiguous region indicative of a global rearrangement was observed in this mapping.

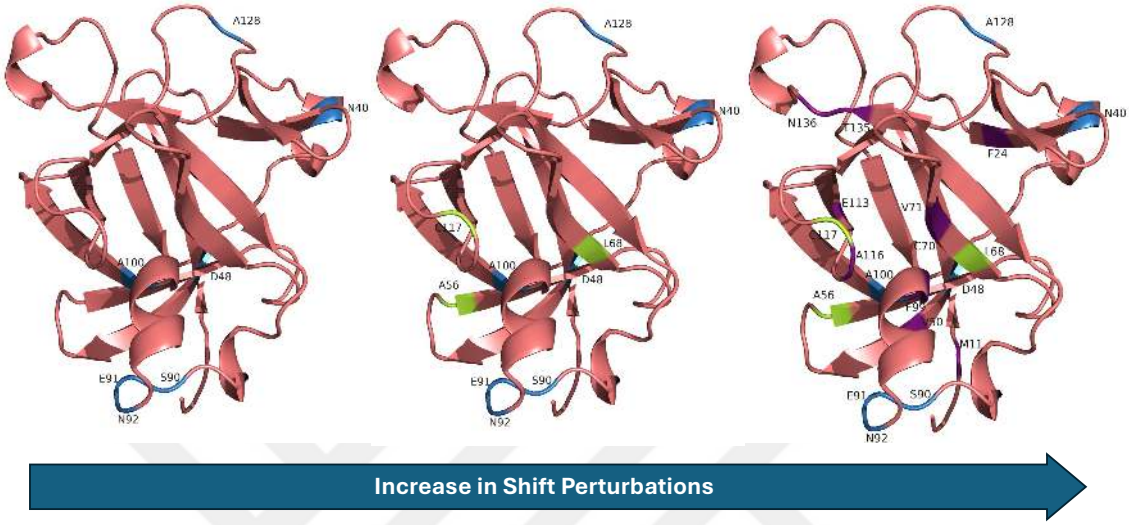

Figure 4.29: Structural mapping of CSP magnitudes on IL-1Ra after thiol-PEGylation.

Residues with mild (left, blue), moderate (middle, green), and strong (right, purple) perturbations are highlighted on the IL-1Ra fold; arrow denotes increasing shift magnitude. Perturbations cluster near the cysteine region and select distal sites, consistent with localized effects rather than global unfolding.

4.15. Cell Viability on HEK-Blue™ IL-1β Cells (M143V-Only)

To confirm that the M143V variant does not exert cytotoxic effects on HEK-Blue™ IL-1β cells in the absence of inflammatory stimulus, metabolic activity was assessed using an MTT assay across a wide range of antagonist concentrations. Cells were incubated with M143V alone, without IL-1β stimulation, for 24 hours at concentrations spanning from 0.25 pM to 2500 pM.

As shown in **Figure *4.30***, metabolic activity remained consistently above 100% across all tested concentrations, with no statistically significant decrease relative to untreated control wells. Even at the highest concentration (2500 pM), M143V treatment did not induce any measurable cytotoxicity, and all values remained well above the commonly accepted viability threshold of 70% (indicated by the horizontal line).

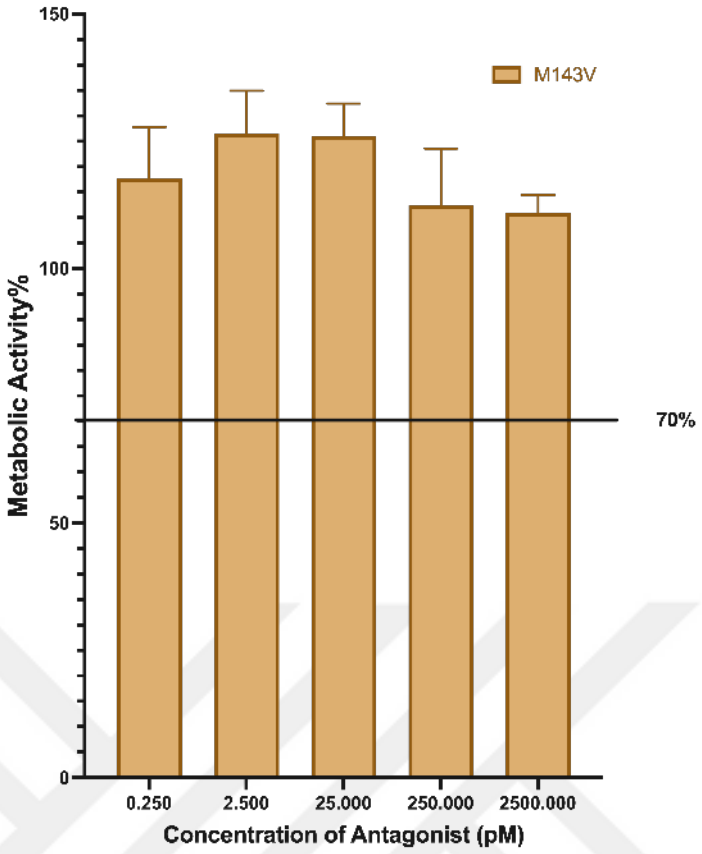

Figure 4.30: Cell viability under M143V treatment.

MTT assay in HEK-Blue™ IL-1β cells across 0.25–2500 pM shows no concentration-dependent cytotoxicity; all conditions remained above the 70% viability threshold (bars = mean ± SD).

These results confirm that M143V is non-toxic to HEK-Blue™ IL-1β cells at the doses used in subsequent bioactivity assays. The absence of cytotoxicity ensures that any observed changes in reporter activity upon IL-1β stimulation and antagonist co-treatment can be attributed to specific biological inhibition rather than off-target toxic effects.

4.16. HEK-Blue™ IL-1β Antagonist Performance (QUANTI-Blue; IC_{50}/IC_{80}/IC_{90})

M143V and reference Anakinra were profiled across 0.25–2,500 pM antagonist in HEK-Blue™ IL-1β cells at a fixed IL-1β EC_{80} = 12.59 pM. Percent SEAP production was normalized to the IL-1β-only control and curves were fit with a 4-parameter logistic (4PL) model (Top, Bottom, IC_{50}, Hill slope). Both datasets reached stable upper and lower plateaus and produced smooth sigmoids suitable for parameter estimation (**Figure *4.31***). Fitted potencies were IC_{50} = 15.80 pM (Anakinra) and 15.56 pM (M143V). Higher effect levels were IC_{80} = 40.29 pM / 48.43 pM and IC_{90} = 69.66 pM / 94.10 pM for Anakinra

and M143V, respectively (table inset in **Figure *4.31***). Hill slopes and asymptotes were comparable between curves.

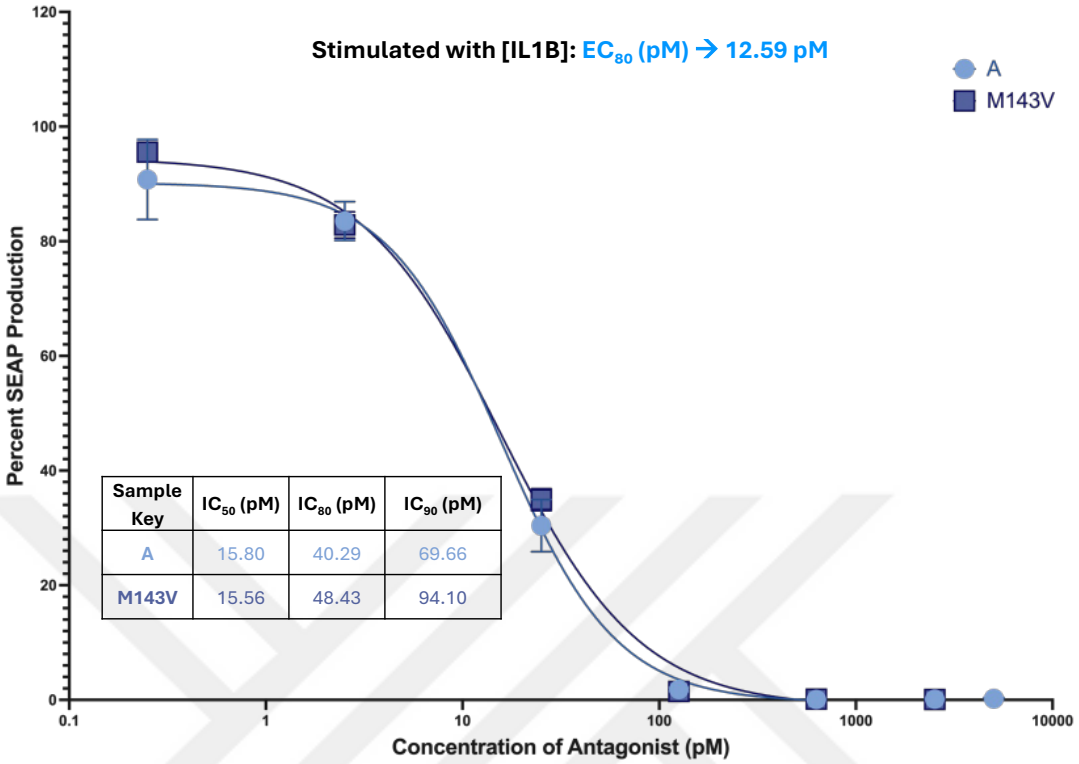

Figure 4.31: Comparative dose–response of anakinra (A) and M143V in the HEK-Blue™ IL-1β assay.

Curves were fit with a 4-parameter logistic model at a fixed IL-1β EC80 stimulus. The two profiles substantially overlap, indicating comparable inhibitory potency and full efficacy under identical conditions (points = mean ± SD).

Unmodified M143V, T10-M143V (maleimide-PEG, 10 kDa) and N10-M143V (NHS-PEG, 10 kDa) were evaluated under the same conditions (0.25–5,000 pM antagonist; IL-1β EC_{80} = 12.59 pM; 4PL fits). All constructs produced sigmoidal inhibition curves with defined Top/Bottom plateaus (**Figure *4.32***). Fitted potencies were IC_{50} = 15.56 pM (M143V), 1,078 pM (T10-M143V), and 974.5 pM (N10-M143V). Corresponding higher-effect parameters were IC_{80} / IC_{90} = 3,565.20 / 7,177.14 pM (T10-M143V) and 2,228.47 / 3,615.26 pM (N10-M143V); M143V values matched those above (48.43 / 94.10 pM). Hill slopes were of similar magnitude across the three fitted curves, and maximal inhibition was reached within the tested concentration range.

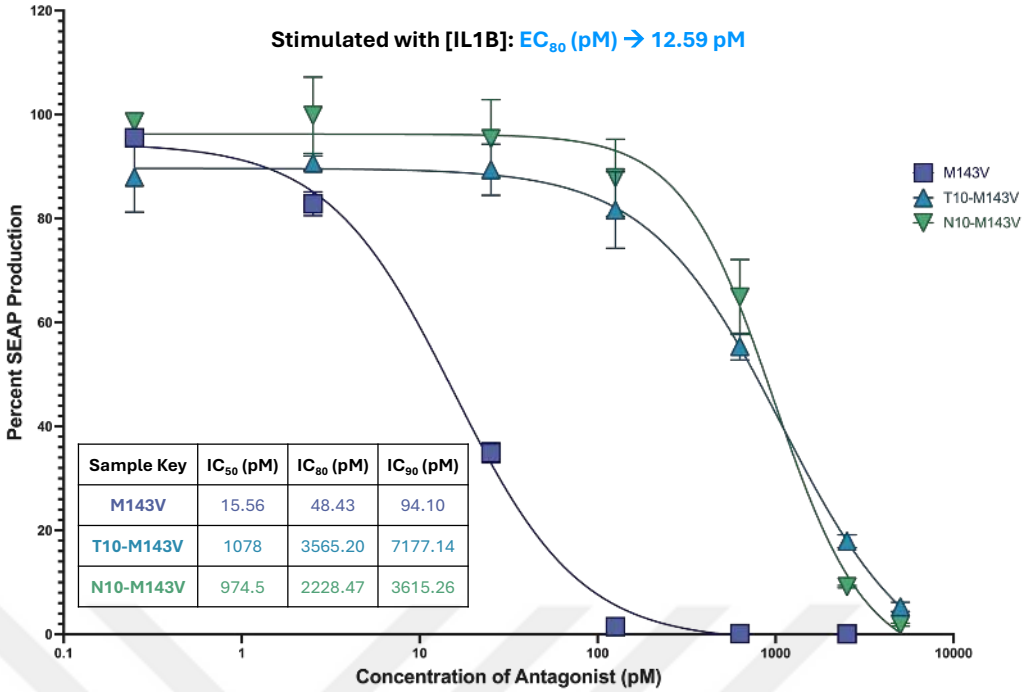

Figure 4.32: Dose–response of M143V versus its 10 kDa PEG conjugates (thiol: T10–M143V; lysine: N10–M143V) in the HEK-Blue™ IL-1β assay.

Curves were fit with a 4-parameter logistic model at a fixed IL-1β EC80 stimulus. Both conjugates retain full efficacy with a right-shifted potency relative to M143V; thiol- and lysine-derived profiles are broadly similar.

5. DISCUSSION

5.1. Comparative structural investigation of IL-1Ra: available cysteines vs lysines

Structural mapping of IL-1Ra (PyMOL) identified four cysteines—Cys67, Cys70, Cys117, Cys123—with Cys70/Cys117/Cys123 solvent-exposed and Cys67 buried. Thus, thiol-selective PEGylation is expected to occur predominantly at the accessible residues, inherently limiting positional isomers and easing downstream analytics/purification. In line with this, mPEG-maleimide, whose thiol selectivity near neutral pH yields stable thioether linkages, was used in the thiolation reactions, enabling site-specific modification at native cysteines.

Complementing the cysteine map, IL-1Ra presents multiple solvent-exposed lysines (e.g., Lys65, Lys94, Lys97, Lys146), and importantly, Lys21 and Lys145 lie at/near the receptor-binding interface. Consequently, it was proposed that nonspecific PEGylation using NHS-ester (amine-directed) can access many sites, including positions where modification may perturb binding[140].

Consistent with prior IL-1Ra work and PEGylation reviews, thiol-specific (cysteine) PEGylation typically yields more homogeneous products than lysine-targeted routes because cysteines are comparatively scarce in proteins (≈1–2% of residues), creating far fewer reactive sites. By contrast, amine (lysine) PEGylation accesses many surface lysines and often produces positional/multi-PEG isomers that are hard to separate. For studies that focus on IL-1Ra specifically, random lysine PEGylation generated multiple positional isomers with poor chromatographic separability, whereas cysteine-targeted PEGylation afforded relatively homogeneous mono-PEGylated derivatives[142,143]. Hence, the conjugation with cysteine-targeted PEGylation is expected to occur predominantly at the accessible residues, yielding fewer isomers than lysine-directed routes and therefore simpler analytics and purification.

5.2. Rationale for Screening 5/10/20 kDa (Thiolation vs. Nonspecific PEGylation)

For IL-1Ra (anakinra), polymer size drives a predictable potency–PK trade-off: as chain length grows, receptor association slows (lower k_{on}), while k_{off} change is insignificant, leading to an apparent decrease in affinity to its receptor. However, using longer-chain polymers increases the hydrodynamic size, which is required to prolong circulation. In one of the studies on IL-1Ra, this trade-off was confirmed by using surface plasmon resonance on anakinra conjugates, stating that even though the PEG (and linear

polyglycerol) conjugates retain low-nanomolar binding, their k_{on} values decline with polymer size across the 5 → 10 → 20 → 40 kDa series, consistent with growing steric screening at the IL-1Ra/IL-1R1 interface[144]. In an independent head-to-head (PEG vs HES) on anakinra, on-rates for polymer–protein conjugates were ~1 log slower than native. At the same time, off-rates remained similar, again indicating that the main penalty of larger chains is on association rather than complex stability[48].

On the PK side, simply reaching a larger hydrodynamic footprint is necessary to slow renal filtration (native anakinra ~4.4 nm; mono-polymer conjugates ~14.4–14.7 nm)[48]. However, not every 20 kDa construct clears more slowly *in vivo*: 20 kDa hyperbranched polyglycerol (hPG) at the N-terminus failed to extend half-life in mice relative to native anakinra, whereas linear 40 kDa conjugates (PEG or LPG) extended $t_{½}$ by ~4–5×—underscoring that size and architecture both matter and that the PK gains become unambiguous at larger sizes[144].

Against that backdrop, 5/10/20 kDa provides a purposeful ladder that spans the activity–exposure design space most relevant for IL-1Ra:

- **5 kDa**: serves as a high-activity anchor with the smallest k_{on} penalty. (Low-nanomolar K_D; minimal size gain.)
- **10 kDa**: typically imposes only a **modest extra binding penalty in comparison to 5 kDa** while offering a **meaningfully larger hydrodynamic size,** which provides a practical balance between potency and half-life.
- **20 kDa**: probes whether additional size brings PK upside worth the steeper association-rate penalty, and, depending on architecture and site, may **not** improve t½ without further optimization.

Additionally, practical formulation considerations nudge away from unnecessarily large PEGs due to an increase in solution viscosity (notably for PEG vs HES at matched protein concentrations), which can complicate high-dose SC delivery and manufacturing—another reason to center the screen at 5–10–20 kDa before exploring larger sizes[48].

5.3. Comparative Discussion of Thiolation vs Nonspecific PEGylation (at 0.5:1 (PEG:protein))

The cysteine-targeted PEGylation (maleimide) produced markedly cleaner, higher-converting di-PEGylated species at 5 and 10 kDa, whereas the 20 kDa run showed lower conversion and broadened profiles. Lysine-directed (NHS) reactions, in contrast, are

already resolved as mixtures at 0.5 eq, comprising conjugates with distinct DoP bands (≈2 and ≈4) on SDS-PAGE and broader SEC features, with 20 kDa again the most heterogeneous. These observations mirror the structural reality of IL-1Ra (few solvent-exposed cysteines vs. several surface lysines) and are consistent with prior reports that thiol targeting yields fewer positional isomers and better separability than random lysine PEGylation[140].

Cys70/117/123 are solvent-exposed while Cys67 is buried, so maleimide chemistry is effectively constrained to a small set of sites; near-stoichiometric dosing therefore limits multi-site events and simplifies analytics. In contrast, multiple accessible lysines (e.g., Lys65/72/94/97/146) allow positional and multi-PEG isomers even at low PEG load, explaining the broader NHS profiles. Literature on IL-1Ra confirms this outcome: thiol-targeted anakinra derivatives are relatively homogeneous (one/two sites) and retain higher binding activity, whereas random lysine conjugates form complex mixtures that could not be separated into single positional isomers and showed low apparent activity[140].

In the case of thiolation with a 0.5 PEG:protein ratio, the 20 kDa maleimide clearly under-converted and produced a more heterogeneous conjugate population, whereas 5 and 10 kDa gave similarly high, clean conversions. Thus, 20 kDa was deprioritized, and the choice was reduced to 5 vs 10 kDa. Between those, 10 kDa offers a more favorable hydrodynamic-size step while preserving the same conjugation performance: literature on anakinra conjugates shows that polymer attachment expands solution size substantially (DLS diameter ~4.4 nm for native anakinra vs ~14.4–14.7 nm after polymer conjugation)[144]. Moreover, datasets spanning 5/10/20/40 kDa confirm that the conjugate's hydrodynamic diameter increases with polymer length, and that conjugates of larger coils elute earlier by SEC, improving size-based separation from the native protein. Taken together, the conversion/heterogeneity data, along with these size relationships, support 10 kDa as the pragmatic choice for thiolation as it avoids the steric penalties seen at 20 kDa while delivering a larger and more easily separable species than 5 kDa.

Here, chain-length effects were consistent across both chemistries. The 5 and 10 kDa PEGs produced substantially higher conversions and more homogeneous conjugate populations than 20 kDa, which frequently showed poorer overall conversion and broader, less-resolved peaks by SEC—findings consistent with steric hindrance and diffusion limits during the coupling window. Mechanistically, shorter chains screen neighboring reactive sites less and access surface clefts more readily, whereas the 20 kDa

polymer imposes greater steric demand that compromises both efficiency and peak definition. Within this context, the 10 kDa PEG condition delivered the most favorable balance: it maintained the high efficiency typical of smaller chains while providing a polymer size expected to better resist rapid renal clearance than 5 kDa.

Application-wise, 10 kDa mPEG-maleimide under thiol-selective conditions achieved ~83% conjugation and typically resolved as a single, well-defined peak; even with lysine-directed chemistry it outperformed the 20 kDa counterpart, yielding two distinct yet separable species rather than a broad distribution. Relative to 5 kDa, the 10 kDa chain confers a more meaningful increase in hydrodynamic radius—directly relevant to *in vivo* exposure—without incurring the steric penalties observed at 20 kDa. Accordingly, PEGylation with 10 kDa was selected for subsequent structural and functional analyses. The 5 kDa polymer remains a viable alternative when maximizing yield is paramount despite its smaller size, whereas the 20 kDa variant consistently exhibited lower conversions and greater downstream handling challenges and is therefore less favorable under otherwise identical conditions.

5.4. Effect of PEG:protein ratio on Thiolation with 10 kDa

At near-stoichiometric feed, the reactions yielded the cleanest analytics and highest apparent di-PEGylated conjugate recovery: 0.5 eq ≈ 82% PEGylated with clear SEC peak separation, and 1.5–3 eq ≈ 88% PEGylated but with progressively poorer resolution (peaks coalescing). Pushing PEG further (6–9 eq) flipped the trend, leading to an apparent PEGylated fraction drop (~31% → ~20%) and an increased heterogeneity (no resolvable PEGylated conjugates by SEC/SDS-PAGE). Mechanistically, this is exactly what the IL-1Ra literature and PEGylation reviews would predict for cysteine-selective coupling: IL-1Ra presents only a limited set of accessible thiols (Cys70/117/123), so low PEG excess preferentially yields PEGylated conjugates, whereas higher excess leads to multi-site substitution across the same three cysteines, producing unresolved positional/degree-of-PEGylation mixtures that broaden/merge on SEC.

Overall, the results show that stoichiometric fine-tuning is critical for balancing efficiency and homogeneity. Molar fold of 0.5 provided the most practical compromise: high conversion rates with excellent homogeneity. These conditions favor consistent downstream purification and reproducible characterization, while still achieving the intended increase in hydrodynamic radius. By contrast, excessive PEG input not only

failed to improve efficiency but also generated highly heterogeneous mixtures, complicating both analysis and potential therapeutic application.

5.5. Effect of PEG:Protein ratio on lysine-PEGylation (0.5 vs 1.5; 5/10/20 kDa)

Across all three PEG sizes, moving from a 0.5 to 1.5 PEG:protein ratio increased overall conversion but also broadened the product distribution, with visibly stronger higher-DoP bands and poorer SEC resolution. This pattern is expected for NHS-ester chemistry because it can access many surface lysines, so the reaction is statistical: more reagent increases the probability of multiple attachments per protein and thus heterogeneous, multi-PEG species form. Prior IL-1Ra work explicitly reports that random lysine PEGylation "often produced a complicated mixture of positional isomers"—difficult to resolve chromatographically—whereas site-selective strategies yield more homogeneous products[140]. In the same IL-1Ra study, the lysine protocol even required a much higher PEG:protein molar ratio than thiol PEGylation (≈7.9 for NHS vs ≈2.45 for maleimide), underscoring how pushing stoichiometry on the amine route tends to drive multiple substitutions and complexity.

More generally (and consistent with the presented data), polymer-protein conjugation papers caution that using a high excess of modification reagent for amine-reactive coupling can convert a predominantly single type of conjugate product into a heterogeneous, multi-conjugate mixture. Hence, the common practice is to cap equivalents and accept lower yield to preserve a single type of DoP material[47].

In summary, in the case of nonspecific PEGylation at 5–10 kDa, keeping the PEG:protein ratio low (≈0.5) prioritizes recoverable low-DoP fractions, and raising it to 1.5 helps conversion but compromises homogeneity. For 20 kDa-NHS, the combination of size and multiplicity yields poorly resolvable mixtures, so it remains a comparatively weak candidate. These choices and trade-offs are exactly in line with prior IL-1Ra studies comparing random lysine vs site-selective approaches.

5.6. HEK-Blue™ IL-1β reporter assay-Thiol-selective conjugates (T5-A, T10-A)

Dose–response data for native Anakinra (A) and thiol-selective PEG conjugates (T5-A, T10-A) were acquired in the HEK-Blue™ IL-1β reporter assay with IL-1β fixed at its experimentally determined EC_{80}. Curves were fitted by nonlinear regression to a four-parameter logistic (4PL) model (Top, Bottom, IC_{50}, Hill slope), providing directly comparable potency estimates under identical conditions. Top and Bottom converged to

plateaus consistent with full dynamic range of the assay, **indicating that PEGylation did not diminish the maximal attainable inhibition.**

Native Anakinra yielded a steep, left-shifted inhibition profile and achieved near-complete pathway suppression at sub-nanomolar concentrations. The fitted IC_{50} was ~16 pM, consistent with high apparent potency for receptor blockade in this system. By contrast, both PEGylated analogues displayed right-shifted sigmoids of comparable slope and unchanged Emax, indicating preserved efficacy with reduced apparent potency. The fitted IC_{50} values were ~420 pM for T5-A and ~420 pM for T10-A (**Figure *4.18***), corresponding to an approximate 25–30-fold rightward shift relative to unmodified Anakinra. Notably, the IC_{50} estimates and confidence intervals for T5-A and T10-A were essentially superimposable, suggesting no measurable dependence on PEG chain length between 5 and 10 kDa at this attachment site.

Analysis at higher effect levels showed the same pattern. The IC_{80} values were ~1.75 nM (T5-A) and ~1.48 nM (T10-A), while the IC_{90} values were ~4.06 nM (T5-A) and ~3.10 nM (T10-A) (**Figure *4.18***). Thus, a small but consistent advantage for the 10 kDa conjugate emerged only at deeper pathway suppression (80–90%), whereas the mid-range potency (IC_{50}) remained indistinguishable between the two PEG sizes. Hill slopes were similar across all three curves, indicating that PEGylation altered the concentration required to achieve a given effect without changing the cooperative character of inhibition.

Collectively, the 4PL analysis indicates that thiol-directed PEGylation preserves maximal efficacy but imposes a predictable potency penalty, most plausibly through partial steric shielding of receptor-interacting surfaces and/or reduced effective association rates once a polymer coil is appended. Within this chemistry and conjugation locus, chain length in the 5–10 kDa range did not materially modulate IC_{50}, and only modestly favored the 10 kDa format at IC_{80}–IC_{90}. Accordingly, the 10 kDa maleimide conjugate was selected for subsequent studies on the basis of its physicochemical profile and overall performance, with the understanding that higher exposure is required to match the activity of the native protein.

5.7. HEK-Blue™ IL-1β reporter assay-Lysine-targeted conjugates (N5-A, N10-A, N20-A)

Antagonist performance for the lysine-directed conjugates of Anakinra was quantified in HEK-Blue™ IL-1β cells using the same EC_{80} challenge and 4PL fitting procedure described above. Native Anakinra again produced a steep, left-shifted curve, reaching

near-complete pathway blockade at sub-nanomolar doses. In contrast, all three NHS–PEG conjugates exhibited right-shifted inhibition profiles while preserving maximal efficacy: full suppression was achieved at higher concentrations, but the lower plateaus and Hill slopes were broadly comparable to the parent protein.

Estimated potencies (IC_{50}; table inset in **Figure *4.19***) ranked as follows: Anakinra 15.8 pM; N10-A 224.0 pM; N5-A 268.3 pM; N20-A 744.1 pM. Thus, 5 and 10 kDa PEGylation incurred similar ≈14–17-fold losses in apparent potency relative to the native protein, whereas the 20 kDa conjugate displayed a markedly larger ≈47-fold rightward shift. Differences between N5-A and N10-A became slightly more apparent at higher fractional inhibition: IC_{80}/IC_{90} estimates were 627.9/1147.4 pM for N10-A and 753.8/1379.4 pM for N5-A, whereas N20-A required 2612.0/5444.8 pM to reach the same effect levels. Across constructs the top and bottom asymptotes were similar, indicating that PEGylation influenced potency more than efficacy.

Overall, lysine-directed PEGylation preserved maximal efficacy but reduced apparent potency in a PEG size–dependent manner. Within the 5–10 kDa range, the IC_{50} values were of the same order (≈2–3×10^2 pM), and the data did not support a definitive advantage of one chain length over the other. The 20 kDa conjugate consistently required higher concentrations (low-nanomolar) to achieve equivalent inhibition. Accordingly, the lysine series is interpreted as active but potency-shifted relative to native Anakinra, with the magnitude of the shift increasing with polymer size.

Two complementary PEGylation strategies were evaluated side-by-side on Anakinra: thiol-selective conjugation with mPEG-maleimide (targeting the limited set of accessible cysteines) and lysine-directed conjugation with mPEG-SVA (permitting reaction at multiple surface lysines). The structural context explains much of the behavior observed experimentally. In IL-1Ra, three cysteines (Cys70, Cys117, Cys123) are solvent-exposed, whereas Cys67 is buried; by contrast, at least four lysines (Lys65, Lys94, Lys97, Lys146) are prominently surface-accessible. As a result, thiolation is constrained to a small number of sites, while lysine chemistry can access several positions with differing local environments.

At the level of conjugation outcome, thiolation produced higher conversion and markedly lower heterogeneity. With 5 and 10 kDa polymers the PEGylated peak dominated the SEC chromatograms (≈81% for both T5 and T10), and SDS-PAGE resolved a single conjugate band (≈27 kDa for T5; ≈37 kDa for T10) cleanly separated from the ~17 kDa monomer. Lysine-directed reactions, in contrast, gave

broader SEC profiles and multiple conjugate bands on SDS-PAGE that corresponded to distinct degrees of substitution (DoP≈2 at ~27 kDa and DoP≈4 at ~57 kDa). This difference is consistent with the larger set of reactive lysines and with positional isomers that collapse into single SEC features but separate by apparent mass on the gel. For both chemistries, increasing the polymer to 20 kDa reduced conversion (≈37% for T20 by thiolation; ≈33% for N20) and broadened the product distribution, reflecting steric limitations as the PEG coil grows.

Functional readouts from the HEK-Blue™ IL-1β reporter assay showed that maximal efficacy (E_{max}) was preserved across all conjugates, but the concentration required to achieve a given level of inhibition shifted rightward relative to native Anakinra. Using 4-parameter logistic fits, the thiol-PEG conjugates T5-A and T10-A exhibited IC_{50} values in the low-hundreds of picomolar (≈4.2×10^2 pM), whereas Anakinra inhibited with an IC_{50} in the mid-teens of picomolar (≈1.6×10^1 pM). Lysine-PEG conjugates of 5 and 10 kDa showed IC_{50} values of similar order (≈2.7×10^2 pM for N5-A and ≈2.2×10^2 pM for N10-A), while the 20 kDa conjugate required higher concentrations (≈7.4×10^2 pM). Thus, for 5–10 kDa PEGs the potency penalty relative to Anakinra was of the same magnitude for both chemistries (roughly one to two orders of magnitude), and chain-length effects within this window were modest. At higher effect levels (IC_{80}/IC_{90}) a similar pattern was observed: PEGylated curves were right-shifted with preserved slopes, and the 20 kDa species consistently demanded the greatest exposure.

Appending a polymer to the protein surface is expected to partially shield receptor-interacting surfaces and to slow effective association rates, increasing the apparent concentration needed to compete with IL-1β. When the coil becomes large (20 kDa), steric and diffusional effects intensify, reducing both conjugation efficiency and apparent potency. Differences between chemistries then arise from how many positions can be modified: thiolation, limited to a small set of cysteines, furnishes one dominant conjugate with uniform hydrodynamic properties; lysine chemistry samples multiple sites and degrees of substitution, producing families of isomers that are functionally competent but analytically more complex.

Taken together, the comparison highlights a clear trade-off. Thiol-selective PEGylation delivers higher conversion and a single, well-defined product that simplifies purification, structural characterization, and analytical control, at the cost of a predictable right-shift in potency. Lysine-directed PEGylation achieves

similar in-cell efficacy with a comparable potency range for 5–10 kDa PEG, but generates mixtures with multiple degrees and sites of modification. Selection between the two approaches should therefore be guided by downstream priorities: where product homogeneity and biophysical tractability are paramount, thiolation confers practical advantages; where the foremost objective is to minimize potency loss while accepting greater heterogeneity, lysine-directed 5–10 kDa conjugates remain viable.

5.8. Labeled Synthesis, Characterization and Cysteine-targeted PEGylation of M143V

To create a recombinant backbone distinct from the marketed drug while preserving function, we engineered an IL-1Ra variant carrying a single conservative substitution, M143V. This site lies outside the IL-1R1 binding interface and does not involve the surface cysteines used for thiol-selective PEGylation; structural inspection and in-silico assessments indicated no disruption of the native fold. The resulting construct differs from reference recombinant IL-1Ra at only one position (Met→Val at 143; ~99.3% identity) and serves as a sequence-distinguishable scaffold for subsequent PEGylation and biophysical studies.

The co-elution with anakinra and the single ~17 kDa band across SEC fractions indicate that the M143V substitution preserves hydrodynamic size and oligomeric state, supporting its use as a like-for-like backbone for downstream PEGylation and biophysical studies. Together with the SDS-PAGE results, it was confirmed that the purified 15N-labeled M143V protein is structurally homogeneous and free of significant contaminants or degradation products. The successful separation of dimeric content further ensures the reproducibility and reliability of structural and functional characterizations in subsequent experiments.

With a clean, monomeric ^{15}N-M143V baseline established, the behavior of the labeled protein under the pre-established thiol-selective PEGylation workflow was assessed. Because M143V lies distal to the reactive cysteines (Cys70/117/123), no change in maleimide reactivity or site accessibility was anticipated. The single early SEC peak (≈81.5% AUC) with matching SDS-PAGE of fractions T6–T11 as a single ~37 kDa band supports formation of a homogeneous, di-PEGylated M143V species (T10–M143V), consistent with selective conjugation at the exposed cysteine residue(s) and a minor later peak (~18.5% AUC) corresponding to unmodified protein.

5.9. HSQC NMR of Labeled IL-1Ra Variants for Structural Characterization and PEGylation Site Mapping

The HSQC spectra provide a sensitive fingerprint of the backbone amide environment, enabling detection of both global structural rearrangements and local conformational changes.

The high degree of dispersion in the labeled M143V spectra is indicative of a well-folded globular structure, consistent with the native fold of IL-1 receptor antagonist (IL-1Ra). A large number of cross-peaks are observed, many of which have been confidently assigned based on prior datasets[145] and sequence-specific matching. The signal intensity is strong and evenly distributed, with minimal peak overlap, further supporting high sample quality and homogeneity under the conditions used for measurement.

Analyzing the PEGylated conjugate spectra, the overall spectral quality remains high, with retained dispersion and a large fraction of peaks overlapping with the native form. This strongly suggests that the PEGylated protein remains folded and maintains the overall tertiary structure of IL-1Ra despite the covalent addition of a bulky polymer chain. Importantly, the presence of numerous shared peaks across the two spectra confirms that PEGylation did not induce global unfolding or aggregation—an essential prerequisite for maintaining biological activity. Investigating the merged two spectra, while the majority of cross-peaks overlap precisely between the two samples, a subset of residues exhibits distinct chemical shift perturbations (CSPs), as indicated by arrows. These shifts reflect alterations in the local chemical environment of the corresponding backbone amides, likely due to changes in sterics, hydrophobicity, or local dynamics near the PEGylation site. A large number of cross-peaks are observed, many of which were confidently assigned by comparing experimental chemical shifts to a published IL-1Ra reference dataset using a custom Python-based matching algorithm that applied weighted distance metrics and iterative refinement to ensure high assignment accuracy.

It is worth emphasizing that the observed CSPs are limited in number and magnitude, and no systematic broadening or disappearance of peaks was detected. This suggests that the PEG chain does not induce extensive flexibility or disorder in the protein core. The presence of well-resolved peaks and minimal signal loss further confirms that T10-M143V remains monodisperse in solution and suitable for downstream NMR-based characterization.

Together, these findings demonstrate that thiol-specific PEGylation of M143V preserves its native fold while inducing only localized, non-disruptive conformational changes.

HSQC NMR thus provides strong evidence for the structural compatibility of site-specific PEGylation, supporting its use in the development of long-acting biologics without compromising protein integrity.

To complement the spectral overlay of native and PEGylated M143V, quantitative chemical shift perturbation (CSP) analysis was conducted for each assigned residue. The weighted CSP values, calculated from differences in ^{1}H and ^{15}N chemical shifts, are shown as a bar plot in **Figure 4.28**, with thresholds of $\Delta\delta > 0.25$, 0.40, and 1.00 used to categorize the perturbations into mild, moderate, and strong. Most residues exhibited minimal shifts, indicating structural preservation upon thiol-selective PEGylation; however, a defined subset displayed more pronounced changes.

These residues were then mapped onto the 3D structure of M143V (**Figure 4.29**), color-coded according to their CSP magnitude. The spatial distribution reveals that significantly perturbed residues are not localized to a single region but span across the β-barrel core, flexible loops, and surface-exposed helices. Notably, several residues with strong CSPs are distant from the PEGylation site, suggesting that the structural impact of conjugation may extend through indirect, possibly allosteric effects rather than local steric hindrance alone.

Mildly perturbed residues tend to cluster near loop regions or exposed surfaces, which may be more sensitive to dynamic shifts or altered solvent interactions. In contrast, residues with the highest perturbation values are often located at structurally conserved or tightly packed positions, implying subtle internal rearrangements or rigidity changes in response to PEG attachment.

Altogether, these results provide residue-specific insight into the structural tolerance of M143V to thiol-specific PEGylation. The overall native fold remains intact, while a select group of residues undergoes quantifiable but localized chemical environment changes. These observations support the conclusion that PEGylation introduces only targeted structural effects and does not compromise the global stability or folding of the protein.

5.10. HEK-Blue™ IL-1β reporter assay-M143V and its PEGylated Conjugates of (T10-M143V, N10-M143V)

A side-by-side comparison of M143V and Anakinra was performed to assess whether the M143V mutation affects the inhibitory performance of the IL-1 receptor antagonist. Both antagonists were tested across a concentration range of 0.25 to 2500 pM, using the EC80 dose of IL-1β to ensure a robust induction of the SEAP reporter. Percent SEAP production

was normalized to the IL-1β-only control, and the resulting dose–response curves were fitted to calculate inhibitory parameters.

As shown in **Figure 4.31**, the response profiles of M143V and Anakinra were nearly identical. Both curves exhibited smooth, sigmoidal transitions from baseline to full inhibition, with no substantial difference in slope, maximum suppression, or sensitivity range. The calculated IC50 values were 15.80 pM for Anakinra and 15.56 pM for M143V, indicating virtually identical potencies at half-maximal inhibition. Similarly, IC80 and IC90 values remained in close agreement, further supporting comparable antagonist performance across the full dynamic range of the assay.

No significant deviation was observed in the degree of inhibition at low or high doses, suggesting that the M143V substitution does not alter the binding mode or downstream antagonistic effect. The overlap between curves is particularly important in the therapeutic context, as it confirms that the engineered variant preserves critical functional properties required for IL-1 signaling blockade.

These results, when considered alongside structural and stability data presented in previous sections, reinforce the conclusion that the M143V mutant is functionally equivalent to the reference molecule. This functional parity provides a strong foundation for the continued development of PEGylated M143V conjugates as long-acting IL-1Ra formulations.

To assess the functional impact of PEGylation on the inhibitory activity of M143V, a side-by-side comparison was performed between unmodified M143V, thiol-specific PEG10 conjugate (T10-M143V), and lysine-directed PEG10 conjugate (N10-M143V). Each construct was evaluated in a dose–response format using IL-1β-stimulated HEK-Blue™ IL-1β cells, and percent SEAP production was used as a readout of residual inflammatory signaling. Antagonist concentrations spanned from 0.25 to 5000 pM, and curves were normalized to the IL-1β-only condition to express SEAP output as a percentage of uninhibited activity.

As shown in **Figure 4.32**, PEGylation substantially reduced the inhibitory potency of M143V, with a clear rightward shift in the dose–response curves for both conjugates. The non-PEGylated form, M143V, displayed a steep sigmoidal curve with an IC50 of 15.56 pM, consistent with previous results. In contrast, T10-M143V exhibited significantly reduced potency, with an IC50 of 1078 pM, and N10-M143V showed a similarly reduced response (IC50 = 974.5 pM). These values represent approximately a 70-fold and 60-fold loss in potency, respectively, relative to native M143V.

Higher-order inhibition metrics reinforced this trend. The IC80 and IC90 values of T10-M143V (3565.20 pM and 7177.14 pM) and N10-M143V (2228.47 pM and 3615.26 pM) were elevated by more than an order of magnitude compared to the parent protein, reflecting delayed attainment of maximal inhibition. Despite these shifts, both PEGylated variants retained full inhibitory capacity at the highest concentrations tested, with SEAP suppression approaching baseline levels, confirming that PEGylation affects potency rather than efficacy.

Notably, although both conjugates demonstrated attenuated activity, T10-M143V exhibited slightly stronger inhibition than N10-M143V at equivalent concentrations, especially in the mid-response range (10–500 pM). This suggests that site-specific PEGylation via cysteines may better preserve functional binding relative to random lysine-targeted modification, which may interfere with key surface residues involved in receptor interaction.

Together, these findings underscore the trade-off between extended half-life and retained bioactivity in PEGylated biologics. While both conjugates demonstrate reduced potency, their preserved efficacy at higher doses supports their continued evaluation in pharmacokinetic contexts. Furthermore, the marginally improved performance of T10-M143V highlights the value of site-selective conjugation strategies in mitigating the functional costs of PEGylation.

6. FUTURE DIRECTIONS

This work establishes analytical and structural comparators for IL-1Ra conjugates and provides a foundation for extending these insights toward in vivo pharmacokinetics. A natural continuation will be to determine whether the PEGylated lead(s) achieve a meaningful half-life gain through single- and/or repeated-dose PK studies with appropriate native controls and sampling windows. Rather than representing a deficiency, this progression reflects the translational path anticipated for long-acting cytokine constructs.

The structural framework developed here also opens opportunities for complementary orthogonal analytics. Techniques such as SEC-MALS could be incorporated to report absolute molar mass and aggregation directly on the SEC peak, while peptide-level LC–MS/MS (with optional intact or middle-down workflows) may be employed to further substantiate degree of PEGylation and site occupancy. These additions would not replace the HSQC evidence of a preserved native-like fold, but enrich the multi-modal characterization pipeline demonstrated in this thesis.

An additional frontier involves immunogenicity to polymer conjugates. With increasing attention to pre-existing and treatment-emergent anti-PEG antibodies, a staged assessment following PK evaluation—such as baseline anti-polymer prevalence and repeat-dose monitoring—would help contextualize safety prior to clinical translation. Importantly, the systematic pipeline established here is not limited to PEG: alternative backbones such as PAS, linear polyglycerol, or HES could be benchmarked within the same head-to-head framework to balance exposure, analytical tractability, and immunological profile. In this way, the methodology developed in this thesis serves as a platform for the rational engineering of next-generation, long-acting IL-1Ra analogues and beyond.

7. CONCLUSION

This thesis established a controlled, structure-guided comparison of PEGylation strategies for IL-1Ra. Accessible residues were mapped, and thiol-selective (maleimide) and lysine-directed (NHS) coupling were evaluated across a common 5/10/20 kDa ladder at matched low stoichiometry. Chemistry—rather than size alone—was found to govern the product profile. Thiol targeting at 5–10 kDa yielded a single, well-defined conjugate, whereas lysine coupling produced heterogeneous families differing in site and degree of modification. A focused stoichiometry sweep identified a practical window for the thiol route in which conversion remained high and peaks were separable. Larger coils (20 kDa) reduced conversion and broadened distributions in both chemistries.

A like-for-like IL-1Ra variant (M143V) was engineered and produced in ^{15}N-labeled form. Its 10 kDa thiol conjugate behaved as a predominantly PEGylated species with clean SEC/SDS profiles, and ^{1}H–^{15}N HSQC confirmed a native-like fold with localized perturbations. In cell assays, maximal inhibition was preserved while dose–response curves were shifted to higher concentrations; formats with 5–10 kDa performed similarly. Overall, a reproducible analytical–structural–functional framework for selecting developable IL-1Ra conjugates is presented, supporting thiol-selective 10 kDa PEG at low equivalents as a robust lead condition.

8. BIBLIOGRAPHY

1 Morris, R., Black, Katrina A. & Stollar, Elliott J. Uncovering protein function: from classification to complexes. *Essays in Biochemistry* **66**, 255-285 (2022). https://doi.org/10.1042/ebc20200108

2 Ebrahimi, S. B. & Samanta, D. Engineering protein-based therapeutics through structural and chemical design. *Nature Communications* **14**, 2411 (2023). https://doi.org/10.1038/s41467-023-38039-x

3 Leader, B., Baca, Q. J. & Golan, D. E. Protein therapeutics: a summary and pharmacological classification. *Nature Reviews Drug Discovery* **7**, 21-39 (2008). https://doi.org/10.1038/nrd2399

4 .

5 Akbarian, M. & Chen, S.-H. Instability Challenges and Stabilization Strategies of Pharmaceutical Proteins. *Pharmaceutics* **14**, 2533 (2022).

6 Zaman, R. *et al.* Current strategies in extending half-lives of therapeutic proteins. *Journal of Controlled Release* **301**, 176-189 (2019). https://doi.org/https://doi.org/10.1016/j.jconrel.2019.02.016

7 Harris, J. M., Martin, N. E. & Modi, M. Pegylation. *Clinical Pharmacokinetics* **40**, 539-551 (2001). https://doi.org/10.2165/00003088-200140070-00005

8 Veronese, F. M. & Mero, A. The Impact of PEGylation on Biological Therapies. *BioDrugs* **22**, 315-329 (2008). https://doi.org/10.2165/00063030-200822050-00004

9 Roberts, M. J., Bentley, M. D. & Harris, J. M. Chemistry for peptide and protein PEGylation. *Advanced Drug Delivery Reviews* **64**, 116-127 (2012). https://doi.org/https://doi.org/10.1016/j.addr.2012.09.025

10 Fontana, A., Spolaore, B., Mero, A. & Veronese, F. M. in *PEGylated Protein Drugs: Basic Science and Clinical Applications* (ed Francesco M. Veronese) 89-112 (Birkhäuser Basel, 2009).

11 Veronese, F. M., Mero, A. & Pasut, G. in *PEGylated Protein Drugs: Basic Science and Clinical Applications* (ed Francesco M. Veronese) 11-31 (Birkhäuser Basel, 2009).

12 Choi, J.-W. *et al.* in *PEGylated Protein Drugs: Basic Science and Clinical Applications* (ed Francesco M. Veronese) 47-73 (Birkhäuser Basel, 2009).

13 Bonora, G. M. & Drioli, S. in *PEGylated Protein Drugs: Basic Science and Clinical Applications* (ed Francesco M. Veronese) 33-45 (Birkhäuser Basel, 2009).

14 Finn, R. F. in *PEGylated Protein Drugs: Basic Science and Clinical Applications* (ed Francesco M. Veronese) 187-203 (Birkhäuser Basel, 2009).

15 Bailon, P. & Berthold, W. Polyethylene glycol-conjugated pharmaceutical proteins. *Pharmaceutical Science & Technology Today* **1**, 352-356 (1998). https://doi.org/https://doi.org/10.1016/S1461-5347(98)00086-8

16 Alconcel, S. N. S., Baas, A. S. & Maynard, H. D. FDA-approved poly(ethylene glycol)–protein conjugate drugs. *Polymer Chemistry* **2**, 1442-1448 (2011). https://doi.org/10.1039/C1PY00034A

17 Belén, L. H. *et al.* From Synthesis to Characterization of Site-Selective PEGylated Proteins. *Frontiers in Pharmacology* **10** (2019). https://doi.org/10.3389/fphar.2019.01450

18 Carter, P. J. Introduction to current and future protein therapeutics: A protein engineering perspective. *Experimental Cell Research* **317**, 1261-1269 (2011). https://doi.org/https://doi.org/10.1016/j.yexcr.2011.02.013

19 Johnson, I. S. Human insulin from recombinant DNA technology. *Science* **219**, 632-637 (1983). https://doi.org/10.1126/science.6337396

20 Murray, J. E., Laurieri, N. & Delgoda, R. in *Pharmacognosy* (eds Simone Badal & Rupika Delgoda) 477-494 (Academic Press, 2017).

21 Dimitrov, D. S. in *Therapeutic Proteins: Methods and Protocols* (eds Vladimir Voynov & Justin A. Caravella) 1-26 (Humana Press, 2012).

22 Nguyen, T. T. K., Pham, K.-Y. & Yook, S. Engineered therapeutic proteins for sustained-release drug delivery systems. *Acta Biomaterialia* **171**, 131-154 (2023). https://doi.org/https://doi.org/10.1016/j.actbio.2023.09.018

23 Dozier, J. K. & Distefano, M. D. Site-Specific PEGylation of Therapeutic Proteins. *International Journal of Molecular Sciences* **16**, 25831-25864 (2015).

24 Kontermann, R. E. Strategies to Extend Plasma Half-Lives of Recombinant Antibodies. *BioDrugs* **23**, 93-109 (2009). https://doi.org/10.2165/00063030-200923020-00003

25 Turecek, P. L., Bossard, M. J., Schoetens, F. & Ivens, I. A. PEGylation of Biopharmaceuticals: A Review of Chemistry and Nonclinical Safety Information of Approved Drugs. *Journal of Pharmaceutical Sciences* **105**, 460-475 (2016). https://doi.org/https://doi.org/10.1016/j.xphs.2015.11.015

26 Werle, M. & Bernkop-Schnürch, A. Strategies to improve plasma half life time of peptide and protein drugs. *Amino Acids* **30**, 351-367 (2006). https://doi.org/10.1007/s00726-005-0289-3

27 Frokjaer, S. & Otzen, D. E. Protein drug stability: a formulation challenge. *Nature Reviews Drug Discovery* **4**, 298-306 (2005). https://doi.org/10.1038/nrd1695

28 Kontos, S. & Hubbell, J. A. Drug development: longer-lived proteins. *Chemical Society Reviews* **41**, 2686-2695 (2012). https://doi.org/10.1039/C2CS15289D

29 Böttger, R., Hoffmann, R. & Knappe, D. Differential stability of therapeutic peptides with different proteolytic cleavage sites in blood, plasma and serum. *PLOS ONE* **12**, e0178943 (2017). https://doi.org/10.1371/journal.pone.0178943

30 Marshall, S. A., Lazar, G. A., Chirino, A. J. & Desjarlais, J. R. Rational design and engineering of therapeutic proteins. *Drug Discov Today* **8**, 212-221 (2003). https://doi.org/10.1016/s1359-6446(03)02610-2

31 Jarosinski, M. A. *et al.* Structural principles of insulin formulation and analog design: A century of innovation. *Mol Metab* **52**, 101325 (2021). https://doi.org/10.1016/j.molmet.2021.101325

32 Pires, I. S., Hammond, P. T. & Irvine, D. J. Engineering Strategies for Immunomodulatory Cytokine Therapies - Challenges and Clinical Progress. *Adv Ther (Weinh)* **4** (2021). https://doi.org/10.1002/adtp.202100035

33 Winkelhake, J. L. & Gauny, S. S. Human recombinant interleukin-2 as an experimental therapeutic. *Pharmacological Reviews* **42**, 1-28 (1990). https://doi.org/https://doi.org/10.1016/S0031-6997(25)00040-7

34 Mark, D. F., Lu, S. D., Creasey, A. A., Yamamoto, R. & Lin, L. S. Site-specific mutagenesis of the human fibroblast interferon gene. *Proceedings of the National Academy of Sciences* **81**, 5662-5666 (1984). https://doi.org/doi:10.1073/pnas.81.18.5662

35 Capon, D. J. *et al.* Designing CD4 immunoadhesins for AIDS therapy. *Nature* **337**, 525-531 (1989). https://doi.org/10.1038/337525a0

36 Binder, U. & Skerra, A. Strategies for extending the half-life of biotherapeutics: successes and complications. *Expert Opinion on Biological Therapy* **25**, 93-118 (2025). https://doi.org/10.1080/14712598.2024.2436094

37 Peppel, K., Crawford, D. & Beutler, B. A tumor necrosis factor (TNF) receptor-IgG heavy chain chimeric protein as a bivalent antagonist of TNF activity. *Journal of Experimental Medicine* **174**, 1483-1489 (1991). https://doi.org/10.1084/jem.174.6.1483

38 Suzuki, T. *et al.* Importance of Neonatal FcR in Regulating the Serum Half-Life of Therapeutic Proteins Containing the Fc Domain of Human IgG1: A Comparative Study of the Affinity of Monoclonal Antibodies and Fc-Fusion Proteins to Human Neonatal FcR. *The Journal of Immunology* **184**, 1968-1976 (2010). https://doi.org/10.4049/jimmunol.0903296

39 Suzuki, T., Hashii, N., Tada, M. & Ishii-Watabe, A. The influence of antibody engineering on Fc conformation and Fc receptor binding properties: Analysis of FcRn-binding engineered antibodies and an Fc fusion protein. *mAbs* **13**, 1923366 (2021). https://doi.org/10.1080/19420862.2021.1923366

40 Kratz, F. Albumin as a drug carrier: Design of prodrugs, drug conjugates and nanoparticles. *Journal of Controlled Release* **132**, 171-183 (2008). https://doi.org/https://doi.org/10.1016/j.jconrel.2008.05.010

41 Nauck, M. A. *et al.* Efficacy and safety of once-weekly GLP-1 receptor agonist albiglutide (HARMONY 2): 52 week primary endpoint results from a randomised, placebo-controlled trial in patients with type 2 diabetes mellitus inadequately controlled with diet and exercise. *Diabetologia* **59**, 266-274 (2016). https://doi.org/10.1007/s00125-015-3795-1

42 Poole, R. M. & Nowlan, M. L. Albiglutide: First Global Approval. *Drugs* **74**, 929-938 (2014). https://doi.org/10.1007/s40265-014-0228-2

43 Escobar, M. *et al.* IDELVION: A Comprehensive Review of Clinical Trial and Real-World Data. *Journal of Clinical Medicine* **11**, 1071 (2022).

44 Chandra, K., Dutta, S., Kolya, H. & Kang, C.-W. Structural Aspect of Hydroxyethyl-Starch–Anticancer-Drug-Conjugates as State-of-the-Art Drug Carriers. *Scientia Pharmaceutica* **91**, 32 (2023).

45 Besheer, A., Hertel, T. C., Kressler, J., Mäder, K. & Pietzsch, M. in *Bioconjugation Protocols: Strategies and Methods* (ed Sonny S. Mark) 17-27 (Humana Press, 2011).

46 Hey, T., Knoller, H. & Vorstheim, P. in *Therapeutic Proteins* 117-140 (2012).

47 Liebner, R. *et al.* Protein HESylation for half-life extension: synthesis, characterization and pharmacokinetics of HESylated anakinra. *Eur J Pharm Biopharm* **87**, 378-385 (2014). https://doi.org/10.1016/j.ejpb.2014.03.010

48 Liebner, R., Meyer, M., Hey, T., Winter, G. & Besheer, A. Head to Head Comparison of the Formulation and Stability of Concentrated Solutions of HESylated versus PEGylated Anakinra. *Journal of Pharmaceutical Sciences* **104**, 515-526 (2015). https://doi.org/https://doi.org/10.1002/jps.24253

49 Liebner, R., Bergmann, S., Hey, T., Winter, G. & Besheer, A. Freeze-drying of HESylated IFNα-2b: Effect of HESylation on storage stability in comparison to PEGylation. *International Journal of Pharmaceutics* **495**, 608-611 (2015). https://doi.org/https://doi.org/10.1016/j.ijpharm.2015.09.031

50 Zarychanski, R. *et al.* Association of Hydroxyethyl Starch Administration With Mortality and Acute Kidney Injury in Critically Ill Patients Requiring Volume Resuscitation: A Systematic Review and Meta-analysis. *JAMA* **309**, 678-688 (2013). https://doi.org/10.1001/jama.2013.430

51 Christidis, C. *et al.* Worsening of hepatic dysfunction as a consequence of repeated hydroxyethylstarch infusions. *Journal of Hepatology* **35**, 726-732 (2001). https://doi.org/https://doi.org/10.1016/S0168-8278(01)00200-8

52 van Witteloostuijn, S. B., Pedersen, S. L. & Jensen, K. J. Half-Life Extension of Biopharmaceuticals using Chemical Methods: Alternatives to PEGylation. *ChemMedChem* **11**, 2474-2495 (2016). https://doi.org/https://doi.org/10.1002/cmdc.201600374

53 Toole, B. P. Hyaluronan: from extracellular glue to pericellular cue. *Nature Reviews Cancer* **4**, 528-539 (2004). https://doi.org/10.1038/nrc1391

54 Elder, A. N., Hannes, S. K., Atoyebi, S. F. & Washburn, N. R. Effects on peptide binding affinity for TNFα by PEGylation and conjugation to hyaluronic acid. *European Polymer Journal* **49**, 2968-2975 (2013). https://doi.org/https://doi.org/10.1016/j.eurpolymj.2013.06.037

55 Fallacara, A., Baldini, E., Manfredini, S. & Vertuani, S. Hyaluronic Acid in the Third Millennium. *Polymers* **10**, 701 (2018).

56 Trombino, S., Servidio, C., Curcio, F. & Cassano, R. Strategies for Hyaluronic Acid-Based Hydrogel Design in Drug Delivery. *Pharmaceutics* **11**, 407 (2019).

57 Harris, J. M. & Chess, R. B. Effect of pegylation on pharmaceuticals. *Nature Reviews Drug Discovery* **2**, 214-221 (2003). https://doi.org/10.1038/nrd1033

58 Smirnov, I. V. *et al.* Chemical Polysialylation of Recombinant Human Proteins. *Methods Mol Biol* **1321**, 389-404 (2015). https://doi.org/10.1007/978-1-4939-2760-9_26

59 Gregoriadis, G., McCormack, B., Wang, Z. & Lifely, R. Polysialic acids: potential in drug delivery. *FEBS Letters* **315**, 271-276 (1993). https://doi.org/https://doi.org/10.1016/0014-5793(93)81177-2

60 Constantinou, A. *et al.* Site-Specific Polysialylation of an Antitumor Single-Chain Fv Fragment. *Bioconjugate Chemistry* **20**, 924-931 (2009). https://doi.org/10.1021/bc8005122

61 Gregoriadis*, G., Fernandes**, A., Mital, M. & McCormack, B. Polysialic acids: potential in improving the stability and pharmacokinetics of proteins and other therapeutics. *Cellular and Molecular Life Sciences CMLS* **57**, 1964-1969 (2000). https://doi.org/10.1007/PL00000676

62 Shi, D. *et al.* To PEGylate or not to PEGylate: Immunological properties of nanomedicine's most popular component, polyethylene glycol and its alternatives. *Advanced Drug Delivery Reviews* **180**, 114079 (2022). https://doi.org/https://doi.org/10.1016/j.addr.2021.114079

63 Gebauer, M. & Skerra, A. Prospects of PASylation® for the design of protein and peptide therapeutics with extended half-life and enhanced action. *Bioorganic & Medicinal Chemistry* **26**, 2882-2887 (2018). https://doi.org/https://doi.org/10.1016/j.bmc.2017.09.016

64 Anand, R. & Vallooran, J. in *Engineering of Biomaterials for Drug Delivery Systems* (ed Anilkumar Parambath) 299-315 (Woodhead Publishing, 2018).

65 Schlapschy, M. *et al.* PASylation: a biological alternative to PEGylation for extending the plasma half-life of pharmaceutically active proteins. *Protein Engineering, Design and Selection* **26**, 489-501 (2013). https://doi.org/10.1093/protein/gzt023

66 Schellenberger, V. *et al.* A recombinant polypeptide extends the in vivo half-life of peptides and proteins in a tunable manner. *Nature Biotechnology* **27**, 1186-1190 (2009). https://doi.org/10.1038/nbt.1588

67 Cleland, J. L. *et al.* A Novel Long-Acting Human Growth Hormone Fusion Protein (VRS-317): Enhanced In vivo Potency and Half-Life. *Journal of Pharmaceutical Sciences* **101**, 2744-2754 (2012). https://doi.org/https://doi.org/10.1002/jps.23229

68 Yuen, K. C. J. *et al.* A Long-Acting Human Growth Hormone With Delayed Clearance (VRS-317): Results of a Double-Blind, Placebo-Controlled, Single Ascending Dose Study in Growth Hormone–Deficient Adults. *The Journal of Clinical Endocrinology & Metabolism* **98**, 2595-2603 (2013). https://doi.org/10.1210/jc.2013-1437

69 Abuchowski, A., van Es, T., Palczuk, N. C. & Davis, F. F. Alteration of immunological properties of bovine serum albumin by covalent attachment of polyethylene glycol. *J Biol Chem* **252**, 3578-3581 (1977).

70 Hershfield, M. S., Chaffee, S. & Sorensen, R. U. Enzyme Replacement Therapy with Polyethylene Glycol-Adenosine Deaminase in Adenosine Deaminase Deficiency: Overview and Case Reports of Three Patients, Including Two Now Receiving Gene Therapy. *Pediatric Research* **33**, S42-S48 (1993). https://doi.org/10.1203/00006450-199333011-00009

71 Fu, C. H. & Sakamoto, K. M. PEG-asparaginase. *Expert Opinion on Pharmacotherapy* **8**, 1977-1984 (2007). https://doi.org/10.1517/14656566.8.12.1977

72 Pasut, G. & Veronese, F. M. State of the art in PEGylation: The great versatility achieved after forty years of research. *Journal of Controlled Release* **161**, 461-472 (2012). https://doi.org/https://doi.org/10.1016/j.jconrel.2011.10.037

73 Jevsevar, S., Kunstelj, M. & Porekar, V. G. PEGylation of therapeutic proteins. *Biotechnol J* **5**, 113-128 (2010). https://doi.org/10.1002/biot.200900218

74 Hu, Y. *et al.* An urchin-like helical polypeptide-asparaginase conjugate with mitigated immunogenicity. *Biomaterials* **268**, 120606 (2021). https://doi.org/https://doi.org/10.1016/j.biomaterials.2020.120606

75 Rouhani, M., Khodabakhsh, F., Norouzian, D., Cohan, R. A. & Valizadeh, V. Molecular dynamics simulation for rational protein engineering: Present and future prospectus. *Journal of Molecular Graphics and Modelling* **84**, 43-53 (2018). https://doi.org/https://doi.org/10.1016/j.jmgm.2018.06.009

76 Hamad, I., Hunter, A. C., Szebeni, J. & Moghimi, S. M. Poly(ethylene glycol)s generate complement activation products in human serum through increased alternative pathway turnover and a MASP-2-dependent process. *Molecular Immunology* **46**, 225-232 (2008). https://doi.org/https://doi.org/10.1016/j.molimm.2008.08.276

77 Armstrong, J. K. *et al.* Antibody against poly(ethylene glycol) adversely affects PEG-asparaginase therapy in acute lymphoblastic leukemia patients. *Cancer* **110**, 103-111 (2007). https://doi.org/https://doi.org/10.1002/cncr.22739

78 Gao, Y., Joshi, M., Zhao, Z. & Mitragotri, S. PEGylated therapeutics in the clinic. *Bioengineering & Translational Medicine* **9**, e10600 (2024). https://doi.org/https://doi.org/10.1002/btm2.10600

79 Kubo, K. *et al.* A randomized, double-blind trial of pegfilgrastim versus filgrastim for the management of neutropenia during CHASE(R) chemotherapy for malignant lymphoma. *Br J Haematol* **174**, 563-570 (2016). https://doi.org/10.1111/bjh.14088

80 Pinto, L. *et al.* Comparison of pegfilgrastim with filgrastim on febrile neutropenia, grade IV neutropenia and bone pain: a meta-analysis of randomized controlled trials. *Curr Med Res Opin* **23**, 2283-2295 (2007). https://doi.org/10.1185/030079907x219599

81 Fleischmann, R. *et al.* Efficacy and safety of certolizumab pegol monotherapy every 4 weeks in patients with rheumatoid arthritis failing previous disease-

modifying antirheumatic therapy: the FAST4WARD study. *Ann Rheum Dis* **68**, 805-811 (2009). https://doi.org/10.1136/ard.2008.099291

82 Smolen, J. *et al.* Efficacy and safety of certolizumab pegol plus methotrexate in active rheumatoid arthritis: the RAPID 2 study. A randomised controlled trial. *Annals of the Rheumatic Diseases* **68**, 797 (2009). https://doi.org/10.1136/ard.2008.101659

83 Avramis, V. I. *et al.* A randomized comparison of nativeEscherichia coli asparaginase and polyethylene glycol conjugated asparaginase for treatment of children with newly diagnosed standard-risk acute lymphoblastic leukemia: a Children's Cancer Group study. *Blood* **99**, 1986-1994 (2002). https://doi.org/10.1182/blood.V99.6.1986

84 Fu, S., Zhu, X., Huang, F. & Chen, X. Anti-PEG Antibodies and Their Biological Impact on PEGylated Drugs: Challenges and Strategies for Optimization. *Pharmaceutics* **17** (2025). https://doi.org/10.3390/pharmaceutics17081074

85 Simberg, D. *et al.* PEGylation technology: addressing concerns, moving forward. *Drug Deliv* **32**, 2494775 (2025). https://doi.org/10.1080/10717544.2025.2494775

86 Administration, U. S. F. a. D. Immunogenicity Testing of Therapeutic Protein Products—Developing and Validating Assays for Anti-Drug Antibody Detection: Guidance for Industry. (Center for Drug Evaluation and Research (CDER) and Center for Biologics Evaluation and Research (CBER), January, 2019).

87 Li, C. *et al.* Research progress on the PEGylation of therapeutic proteins and peptides (TPPs). *Front Pharmacol* **15**, 1353626 (2024). https://doi.org/10.3389/fphar.2024.1353626

88 Lee, B. & Richards, F. M. The interpretation of protein structures: Estimation of static accessibility. *Journal of Molecular Biology* **55**, 379-IN374 (1971). https://doi.org/https://doi.org/10.1016/0022-2836(71)90324-X

89 Cline, G. W. & Hanna, S. B. The aminolysis of N-hydroxysuccinimide esters. A structure-reactivity study. *Journal of the American Chemical Society* **109**, 3087-3091 (1987). https://doi.org/10.1021/ja00244a035

90 Pfister, D. & Morbidelli, M. Process for protein PEGylation. *Journal of Controlled Release* **180**, 134-149 (2014). https://doi.org/https://doi.org/10.1016/j.jconrel.2014.02.002

91 Kinstler, O., Molineux, G., Treuheit, M., Ladd, D. & Gegg, C. Mono-N-terminal poly(ethylene glycol)-protein conjugates. *Adv Drug Deliv Rev* **54**, 477-485 (2002). https://doi.org/10.1016/s0169-409x(02)00023-6

92 Yamamoto, Y. *et al.* Site-specific PEGylation of a lysine-deficient TNF-α with full bioactivity. *Nature Biotechnology* **21**, 546-552 (2003). https://doi.org/10.1038/nbt812

93 Kim, T. H. *et al.* Site-Specific PEGylated Exendin-4 Modified with a High Molecular Weight Trimeric PEG Reduces Steric Hindrance and Increases Type 2 Antidiabetic Therapeutic Effects. *Bioconjugate Chemistry* **23**, 2214-2220 (2012). https://doi.org/10.1021/bc300265n

94 Foser, S. *et al.* Isolation, structural characterization, and antiviral activity of positional isomers of monopegylated interferon alpha-2a (PEGASYS). *Protein Expr Purif* **30**, 78-87 (2003). https://doi.org/10.1016/s1046-5928(03)00055-x

95 Ginn, C., Khalili, H., Lever, R. & Brocchini, S. Pegylation and Its Impact on the Design of New Protein-Based Medicines. *Future Medicinal Chemistry* **6**, 1829-1846 (2014). https://doi.org/10.4155/fmc.14.125

96 Goulet, D. R. & Atkins, W. M. Considerations for the Design of Antibody-Based Therapeutics. *Journal of Pharmaceutical Sciences* **109**, 74-103 (2020). https://doi.org/https://doi.org/10.1016/j.xphs.2019.05.031

97 Ramos-de-la-Peña, A. M. & Aguilar, O. Progress and Challenges in PEGylated Proteins Downstream Processing: A Review of the Last 8 Years. *International Journal of Peptide Research and Therapeutics* **26**, 333-348 (2020). https://doi.org/10.1007/s10989-019-09840-4

98 Payne, R. W., Murphy, B. M. & Manning, M. C. Product development issues for PEGylated proteins. *Pharmaceutical Development and Technology* **16**, 423-440 (2011). https://doi.org/10.3109/10837450.2010.513990

99 Krumm, B., Xiang, Y. & Deng, J. Structural biology of the IL-1 superfamily: Key cytokines in the regulation of immune and inflammatory responses. *Protein Science* **23**, 526-538 (2014). https://doi.org/https://doi.org/10.1002/pro.2441

100 Fields, J. K., Günther, S. & Sundberg, E. J. Structural Basis of IL-1 Family Cytokine Signaling. *Frontiers in Immunology* **Volume 10 - 2019** (2019). https://doi.org/10.3389/fimmu.2019.01412

101 Paik, S. *et al.* Updated insights into the molecular networks for NLRP3 inflammasome activation. *Cellular & Molecular Immunology* **22**, 563-596 (2025). https://doi.org/10.1038/s41423-025-01284-9

102 Wang, H. *et al.* NLRP3 inflammasome in health and disease (Review). *Int J Mol Med* **55** (2025). https://doi.org/10.3892/ijmm.2025.5489

103 Benveniste, E. N. in *Encyclopedia of the Neurological Sciences (Second Edition)* (eds Michael J. Aminoff & Robert B. Daroff) 921-925 (Academic Press, 2014).

104 Chung, Y. *et al.* Critical regulation of early Th17 cell differentiation by interleukin-1 signaling. *Immunity* **30**, 576-587 (2009). https://doi.org/10.1016/j.immuni.2009.02.007

105 Sha, Y. & Markovic-Plese, S. A role of IL-1R1 signaling in the differentiation of Th17 cells and the development of autoimmune diseases. *Self Nonself* **2**, 35-42 (2011). https://doi.org/10.4161/self.2.1.15639

106 Lasigliè, D. *et al.* Role of IL-1 beta in the development of human T(H)17 cells: lesson from NLPR3 mutated patients. *PLoS One* **6**, e20014 (2011). https://doi.org/10.1371/journal.pone.0020014

107 Hou, J. *et al.* Design of a superior cytokine antagonist for topical ophthalmic use. *Proceedings of the National Academy of Sciences* **110**, 3913-3918 (2013). https://doi.org/doi:10.1073/pnas.1217996110

108 Villatoro, A. *et al.* Endogenous IL-1 receptor antagonist restricts healthy and malignant myeloproliferation. *Nature Communications* **14**, 12 (2023). https://doi.org/10.1038/s41467-022-35700-9

109 Hudock, K. M. *et al.* Delayed resolution of lung inflammation in Il-1rn-/- mice reflects elevated IL-17A/granulocyte colony-stimulating factor expression. *Am J Respir Cell Mol Biol* **47**, 436-444 (2012). https://doi.org/10.1165/rcmb.2012-0104OC

110 Caiado, F. & Manz, M. G. IL-1 in aging and pathologies of hematopoietic stem cells. *Blood* **144**, 368-377 (2024). https://doi.org/10.1182/blood.2023023105

111 García-Hernández, M. H., González-Amaro, R. & Portales-Pérez, D. P. Specific Therapy to Regulate Inflammation in Rheumatoid Arthritis: Molecular Aspects. *Immunotherapy* **6**, 623-636 (2014). https://doi.org/10.2217/imt.14.26

112 Braddock, M. & Quinn, A. Targeting IL-1 in inflammatory disease: new opportunities for therapeutic intervention. *Nat Rev Drug Discov* **3**, 330-339 (2004). https://doi.org/10.1038/nrd1342

113 Zhang, F. *et al.* Deconstruction of rheumatoid arthritis synovium defines inflammatory subtypes. *Nature* **623**, 616-624 (2023). https://doi.org/10.1038/s41586-023-06708-y

114 Ganeshalingam, S., Wilson, N. J., Ciciriello, S., Antonipillai, J. & Achuthan, A. A. Cellular interactions in maintaining an inflammatory microenvironment in rheumatoid arthritis. *Molecular Immunology* **184**, 112-122 (2025). https://doi.org/https://doi.org/10.1016/j.molimm.2025.06.008

115 Achudhan, D. *et al.* Antcin K Inhibits TNF-α, IL-1β and IL-8 Expression in Synovial Fibroblasts and Ameliorates Cartilage Degradation: Implications for the Treatment of Rheumatoid Arthritis. *Frontiers in Immunology* **Volume 12 - 2021** (2021). https://doi.org/10.3389/fimmu.2021.790925

116 Firestein, G. S. *et al.* Synovial interleukin-1 receptor antagonist and interleukin-1 balance in rheumatoid arthritis. *Arthritis & Rheumatism* **37**, 644-652 (1994). https://doi.org/https://doi.org/10.1002/art.1780370507

117 Nicklin, M. J., Hughes, D. E., Barton, J. L., Ure, J. M. & Duff, G. W. Arterial inflammation in mice lacking the interleukin 1 receptor antagonist gene. *J Exp Med* **191**, 303-312 (2000). https://doi.org/10.1084/jem.191.2.303

118 Smith, R. J., Chin, J. E., Sam, L. M. & Justen, J. M. Biologic effects of an interleukin-1 receptor antagonist protein on interleukin-1-stimulated cartilage erosion and chondrocyte responsiveness. *Arthritis Rheum* **34**, 78-83 (1991). https://doi.org/10.1002/art.1780340112

119 Fujikawa, Y., Shingu, M., Torisu, T. & Masumi, S. Interleukin-1 receptor antagonist production in cultured synovial cells from patients with rheumatoid arthritis and osteoarthritis. *Ann Rheum Dis* **54**, 318-320 (1995). https://doi.org/10.1136/ard.54.4.318

120 Wang, K. *et al.* Blockade of IL-1 family cytokines in the treatment of rheumatoid arthritis. *Frontiers in Pharmacology* **Volume 16 - 2025** (2025). https://doi.org/10.3389/fphar.2025.1577628

121 Lancieri, M. *et al.* An Update on Familial Mediterranean Fever. *Int J Mol Sci* **24** (2023). https://doi.org/10.3390/ijms24119584

122 Park, Y. H., Wood, G., Kastner, D. L. & Chae, J. J. Pyrin inflammasome activation and RhoA signaling in the autoinflammatory diseases FMF and HIDS. *Nat Immunol* **17**, 914-921 (2016). https://doi.org/10.1038/ni.3457

123 Wouters, F., Bogie, J., Wullaert, A. & van der Hilst, J. Recent Insights in Pyrin Inflammasome Activation: Identifying Potential Novel Therapeutic Approaches in Pyrin-Associated Autoinflammatory Syndromes. *Journal of Clinical Immunology* **44**, 8 (2023). https://doi.org/10.1007/s10875-023-01621-5

124 Mortensen, S. B. *et al.* Pyrin Inflammasome Activation Abrogates Interleukin-1 Receptor Antagonist, Suggesting a New Mechanism Underlying Familial Mediterranean Fever Pathogenesis. *Arthritis & Rheumatology* **73**, 2116-2126 (2021). https://doi.org/https://doi.org/10.1002/art.41770

125 La Bella, S. *et al.* The pyrin inflammasome, a leading actor in pediatric autoinflammatory diseases. *Front Immunol* **14**, 1341680 (2023). https://doi.org/10.3389/fimmu.2023.1341680

126 Chaaban, A. *et al.* A narrative review on the role of cytokines in the pathogenesis and treatment of familial Mediterranean fever: an emphasis on pediatric cases. *Front Pediatr* **12**, 1421353 (2024). https://doi.org/10.3389/fped.2024.1421353

127 Chaaban, A. *et al.* A narrative review on the role of cytokines in the pathogenesis and treatment of familial Mediterranean fever: an emphasis on pediatric cases. *Frontiers in Pediatrics* **Volume 12 - 2024** (2024). https://doi.org/10.3389/fped.2024.1421353

128 Kisla Ekinci, R. M., Kilic Konte, E., Akay, N. & Gul, U. Familial Mediterranean Fever in Childhood. *Turk Arch Pediatr* **59**, 527-534 (2024). https://doi.org/10.5152/TurkArchPediatr.2024.24188

129 Mezher, N., Mroweh, O., Karam, L., Ibrahim, J.-N. & Kobeissy, P. H. Experimental models in Familial Mediterranean Fever (FMF): Insights into pathophysiology and therapeutic strategies. *Experimental and Molecular Pathology* **135**, 104883 (2024). https://doi.org/https://doi.org/10.1016/j.yexmp.2024.104883

130 Meier, D. T., de Paula Souza, J. & Donath, M. Y. Targeting the NLRP3 inflammasome-IL-1β pathway in type 2 diabetes and obesity. *Diabetologia* **68**, 3-16 (2025). https://doi.org/10.1007/s00125-024-06306-1

131 Aggeletopoulou, I., Kalafateli, M., Tsounis, E. P. & Triantos, C. Exploring the role of IL-1β in inflammatory bowel disease pathogenesis. *Frontiers in Medicine* **Volume 11 - 2024** (2024). https://doi.org/10.3389/fmed.2024.1307394

132 Lindblad, C., Rostami, E. & Helmy, A. Interleukin-1 Receptor Antagonist as Therapy for Traumatic Brain Injury. *Neurotherapeutics* **20**, 1508-1528 (2023). https://doi.org/10.1007/s13311-023-01421-0

133 Smirnova, M. I. & Quan, N. Modulation of adult hippocampal neurogenesis by interleukin 1 signaling. *Neurobiology of Sleep and Circadian Rhythms* **18**, 100123 (2025). https://doi.org/https://doi.org/10.1016/j.nbscr.2025.100123

134 Hariharan, A., Hakeem, A. R., Radhakrishnan, S., Reddy, M. S. & Rela, M. The Role and Therapeutic Potential of NF-kappa-B Pathway in Severe COVID-19 Patients. *Inflammopharmacology* **29**, 91-100 (2021). https://doi.org/10.1007/s10787-020-00773-9

135 Economides, A. N. *et al.* Cytokine traps: multi-component, high-affinity blockers of cytokine action. *Nature medicine* **9**, 47-52 (2003). https://doi.org/10.1038/nm811

136 (Sobi), S. O. B. A. Kineret (anakinra) injection, for subcutaneous use: Prescribing information. (U.S. Food and Drug Administration, Stockholm, Sweden, 2024).

137 Liu, H., Yan, W., Li, J., Yan, D. & Luo, D. Post-marketing safety of anakinra and canakinumab: a real-world pharmacovigilance study based on FDA adverse event reporting system. *Frontiers in Pharmacology* **Volume 16 - 2025** (2025). https://doi.org/10.3389/fphar.2025.1483669

138 Gallo, A. *et al.* Interleukin-1 Blockers in Recurrent and Acute Pericarditis: State of the Art and Future Directions. *Medicina* **60**, 241 (2024).

139 Yu, P. *et al.* PEGylation of rhIL-1RA increased its solution stability at room temperature. *Process Biochemistry* **44**, 1340-1345 (2009). https://doi.org/https://doi.org/10.1016/j.procbio.2009.07.010

140 Yu, P. *et al.* Investigation on PEGylation strategy of recombinant human interleukin-1 receptor antagonist. *Bioorganic & Medicinal Chemistry* (2007). https://doi.org/10.1016/j.bmc.2007.05.061

141 Kahraman, K. *et al.* Characterizing the monomer-dimer equilibrium of UbcH8/Ube2L6: A combined SAXS and NMR study. *bioRxiv* (2024). https://doi.org/10.1101/2023.04.13.536743

142 Sornay, C., Vaur, V., Wagner, A. & Chaubet, G. An overview of chemo- and site-selectivity aspects in the chemical conjugation of proteins. *Royal Society Open Science* **9**, 211563 (2022). https://doi.org/doi:10.1098/rsos.211563

143 Istrate, A. *et al.* Platform for Orthogonal N-Cysteine-Specific Protein Modification Enabled by Cyclopropenone Reagents. *Journal of the American Chemical Society* **144**, 10396-10406 (2022). https://doi.org/10.1021/jacs.2c02185

144 Tully, M. *et al.* Polyglycerol for Half-Life Extension of Proteins-Alternative to PEGylation? *Biomacromolecules* (2021). https://doi.org/10.1021/acs.biomac.0c01627

145 Stockman, B. J. *et al.* Secondary structure and topology of interleukin-1 receptor antagonist protein determined by heteronuclear three-dimensional NMR spectroscopy. *Biochemistry* **31**, 5237-5245 (1992). https://doi.org/10.1021/bi00138a001

9. APPENDIX

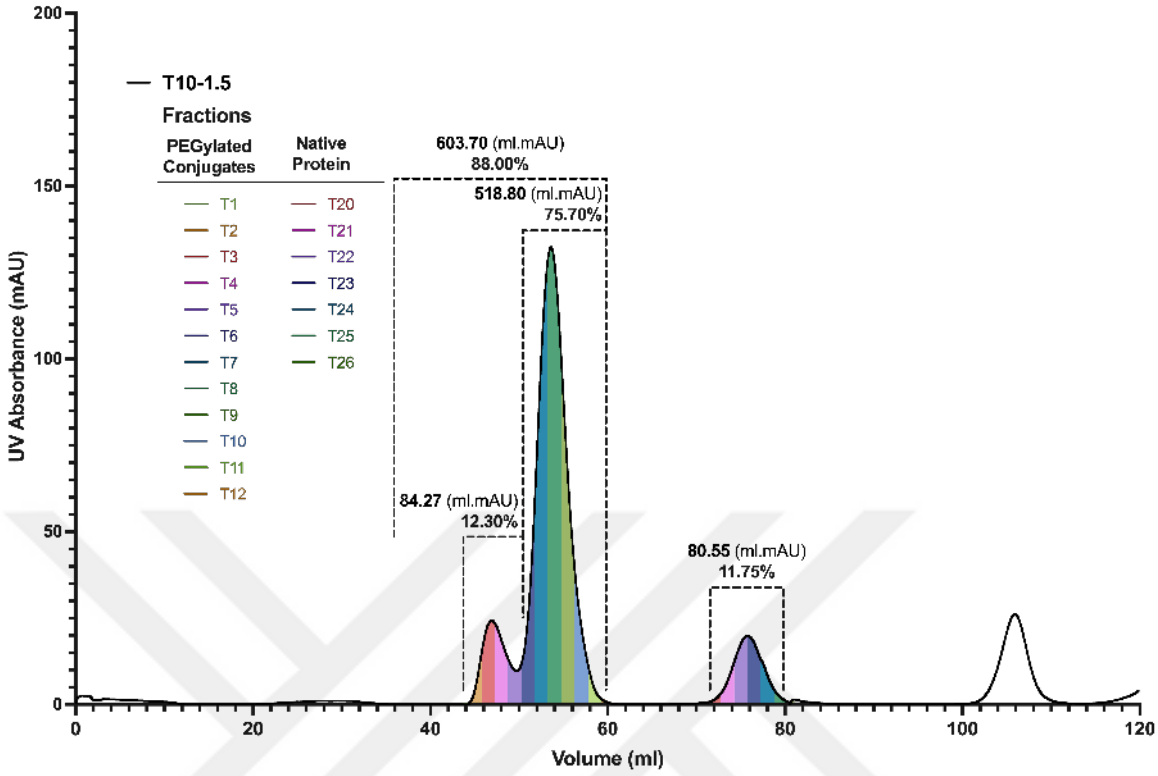

Figure 9.1: PEG:protein ratio screen at 3:2 (T10-1.5), for thiol-selective (mPEG-maleimide) PEGylation of IL-1Ra.

The earlier two peaks correspond to PEGylated IL-1Ra conjugates; the later, narrower peak corresponds to the native protein. Colored overlays indicate collected fractions used for downstream analyses.

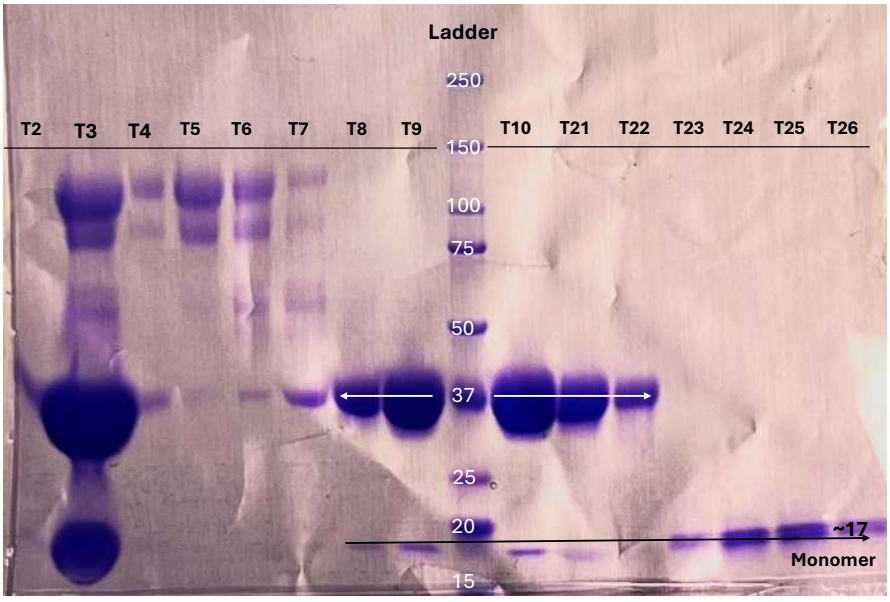

Figure 9.2: SDS–PAGE of T10-1.5.

Fractions of T6, T7, T10 yielding a mildly heterogeneous population of conjugates of various DoPs. T11-16 containing the homogeneous PEGylated conjugate, T34 unconjugated native protein.

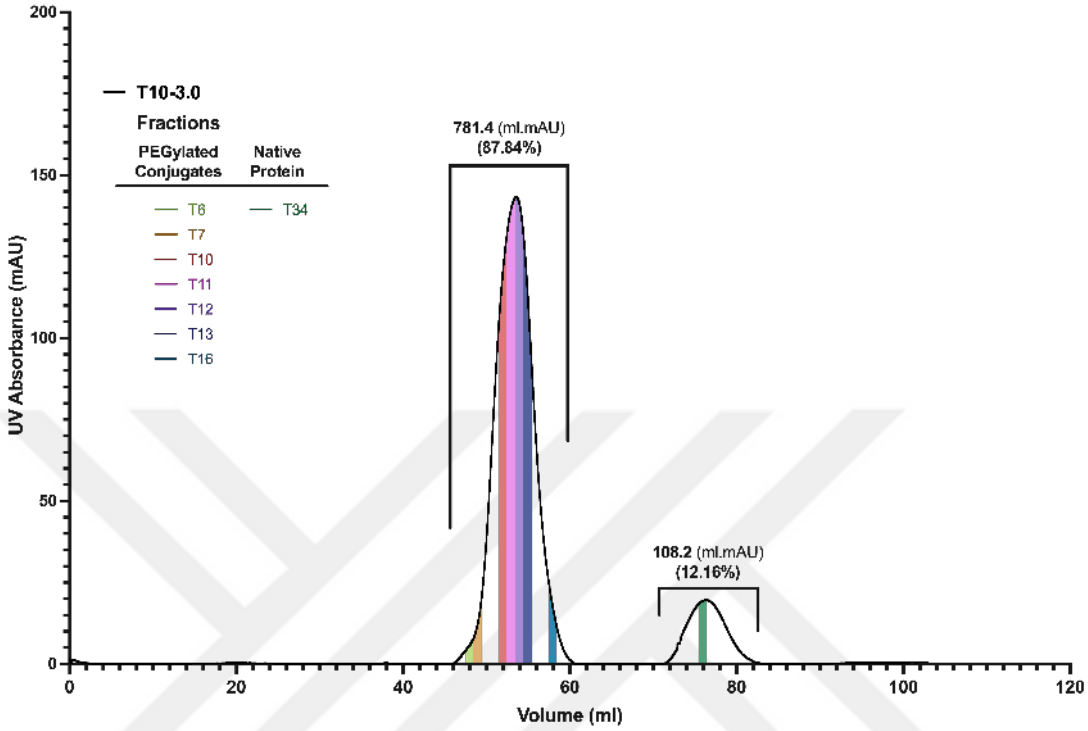

Figure 9.3: PEG:protein ratio screen at 6:2 (T10-3), for thiol-selective (mPEG-maleimide) PEGylation of IL-1Ra.

The earlier peak corresponds to a PEGylated IL-1Ra conjugate; the later, narrower peak corresponds to the native protein. Colored overlays indicate collected fractions used for downstream analyses.

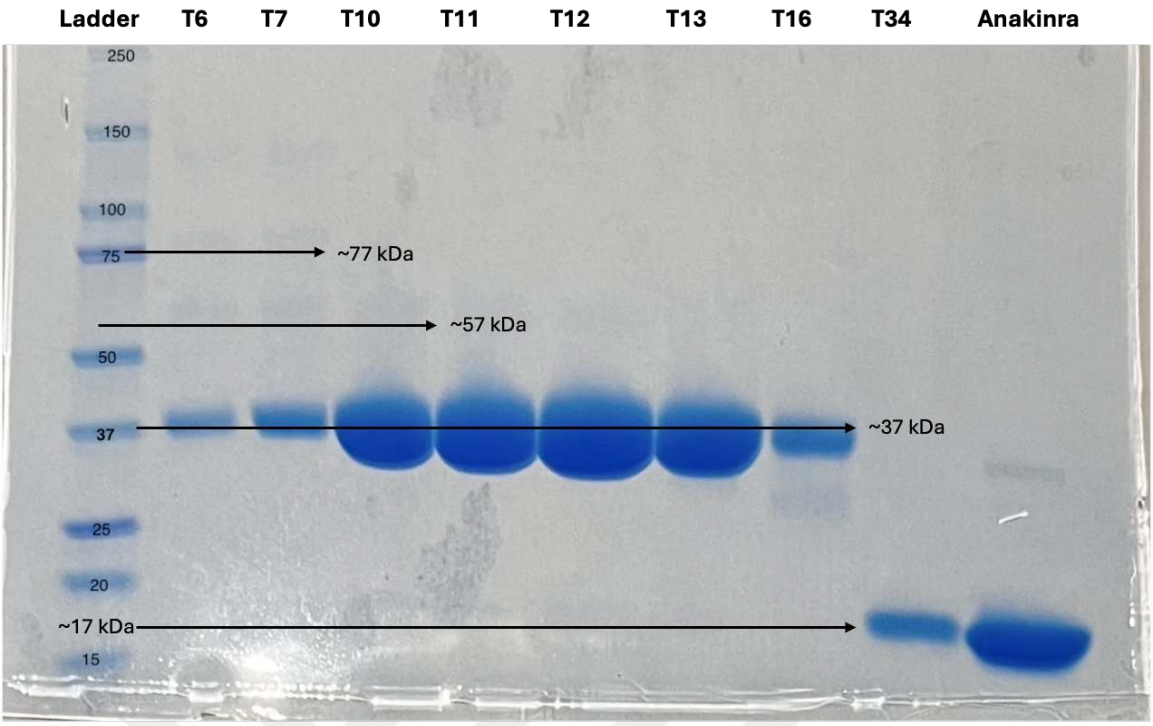

Figure 9.4: SDS–PAGE of T10-3:0.

Fractions of T6, T7, T10 yielding a mildly heterogeneous population of conjugates of various DoPs. T11-16 containing the homogeneous PEGylated conjugate, T34 unconjugated native protein.

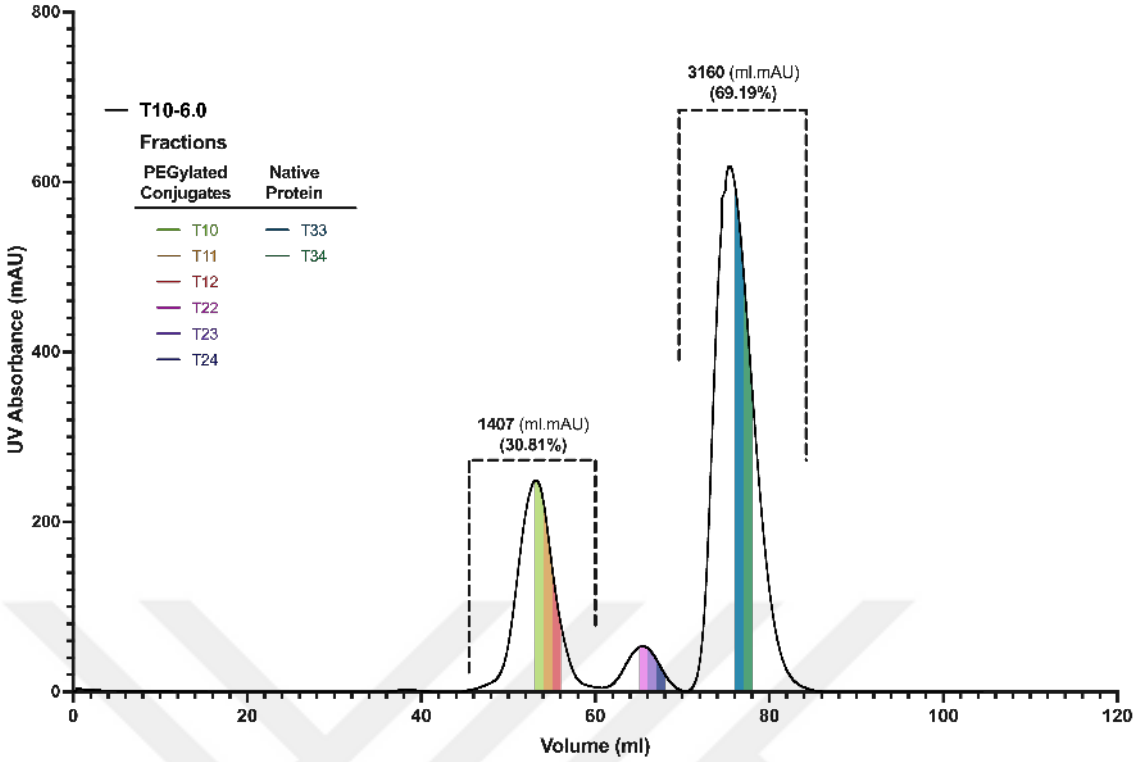

Figure 9.5: PEG:protein ratio screen at 12:2 (T10-6), for thiol-selective (mPEG-maleimide) PEGylation of IL-1Ra.

The earlier peak corresponds to a PEGylated IL-1Ra conjugate; the later, narrower peak corresponds to the native protein. Colored overlays indicate collected fractions used for downstream analyses.

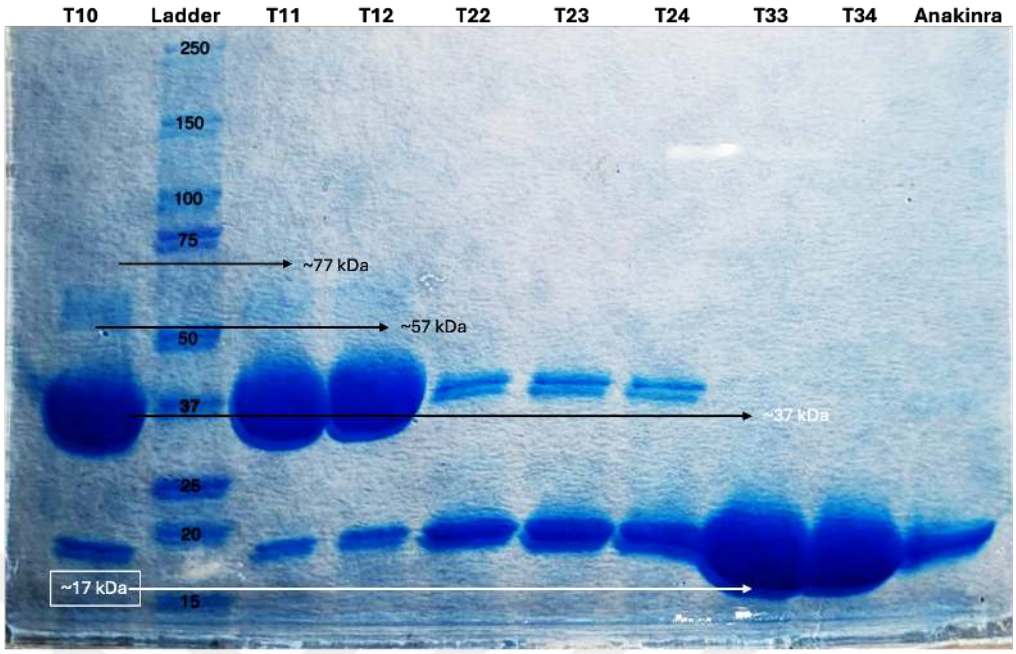

Figure 9.6: SDS–PAGE of T10-6:0.

Fractions of T10, T11, T12 yielding a highly heterogeneous population of conjugates with high DoPs. T22-24 containing a heterogeneous population of conjugates with lower DoPs. T33-34 comprising unconjugated native protein.

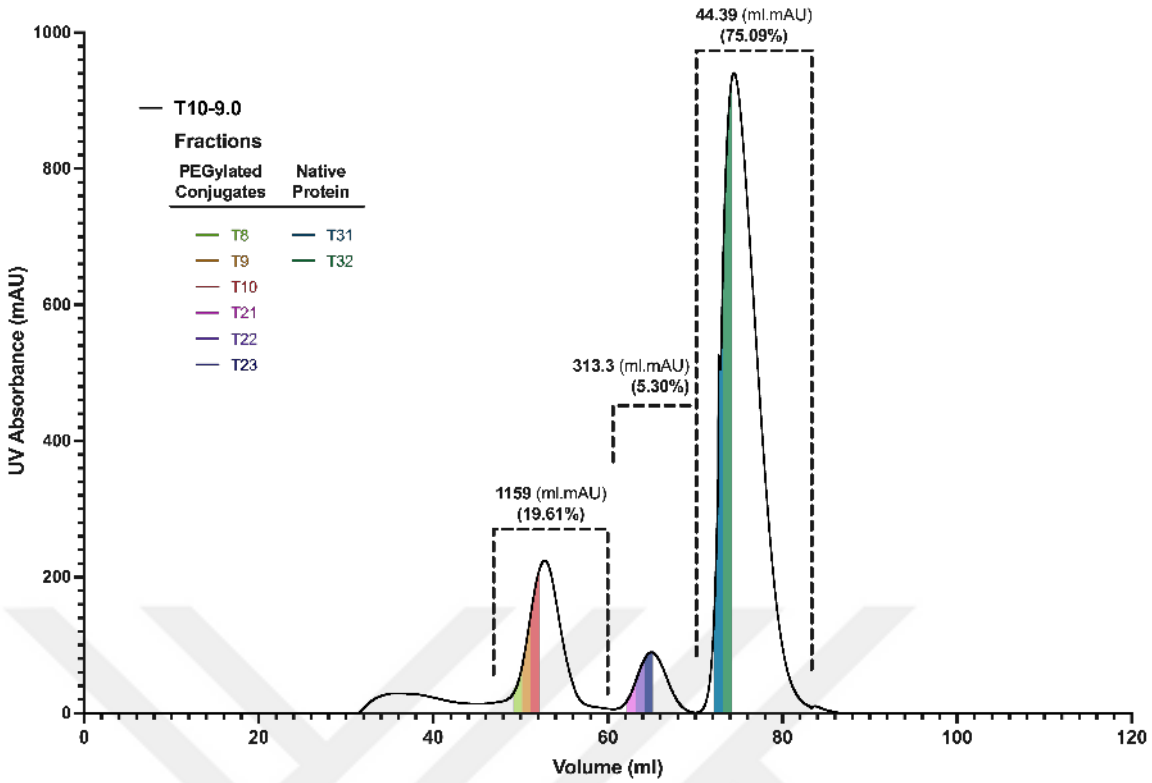

Figure 9.7: PEG:protein ratio screen at 18 : 2 (T10-9), for thiol-selective (mPEG-maleimide) PEGylation of IL-1Ra.

The earlier peak corresponds to a PEGylated IL-1Ra conjugate; the later, higher and narrower peak corresponds to the native protein. Colored overlays indicate collected fractions used for downstream analyses.

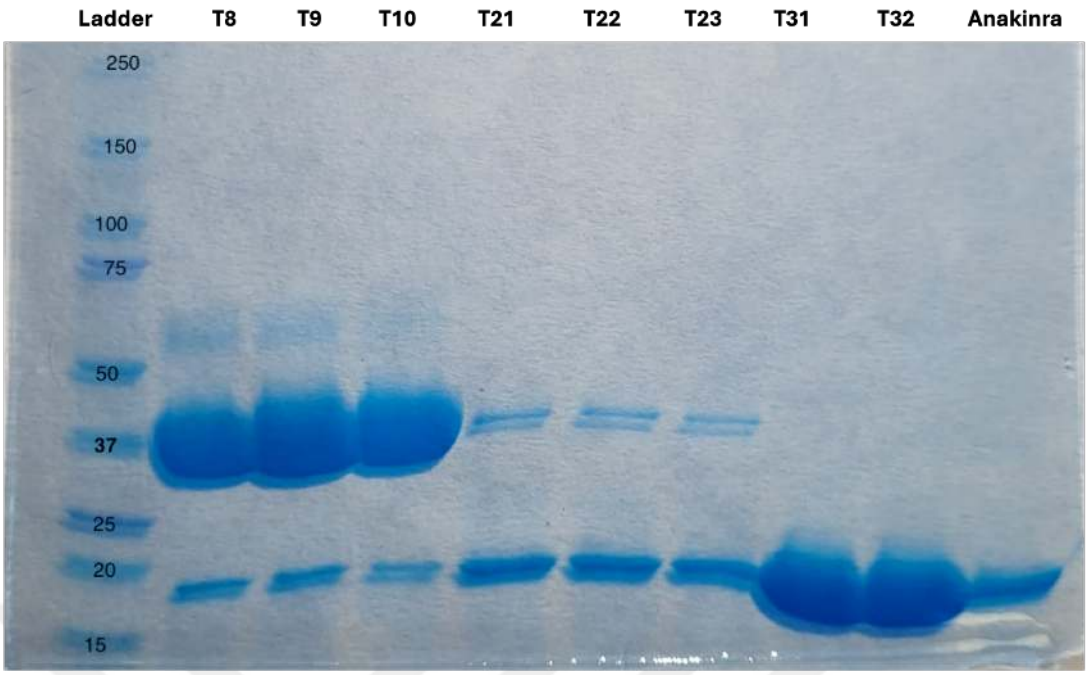

Figure 9.8: SDS–PAGE of T10-9:0.

Fractions of T8, T9, T10 yielding a highly heterogeneous population of conjugates with high DoPs. T21-23 containing a heterogeneous population of conjugates with lower DoPs. T31-32 comprising unconjugated native protein.

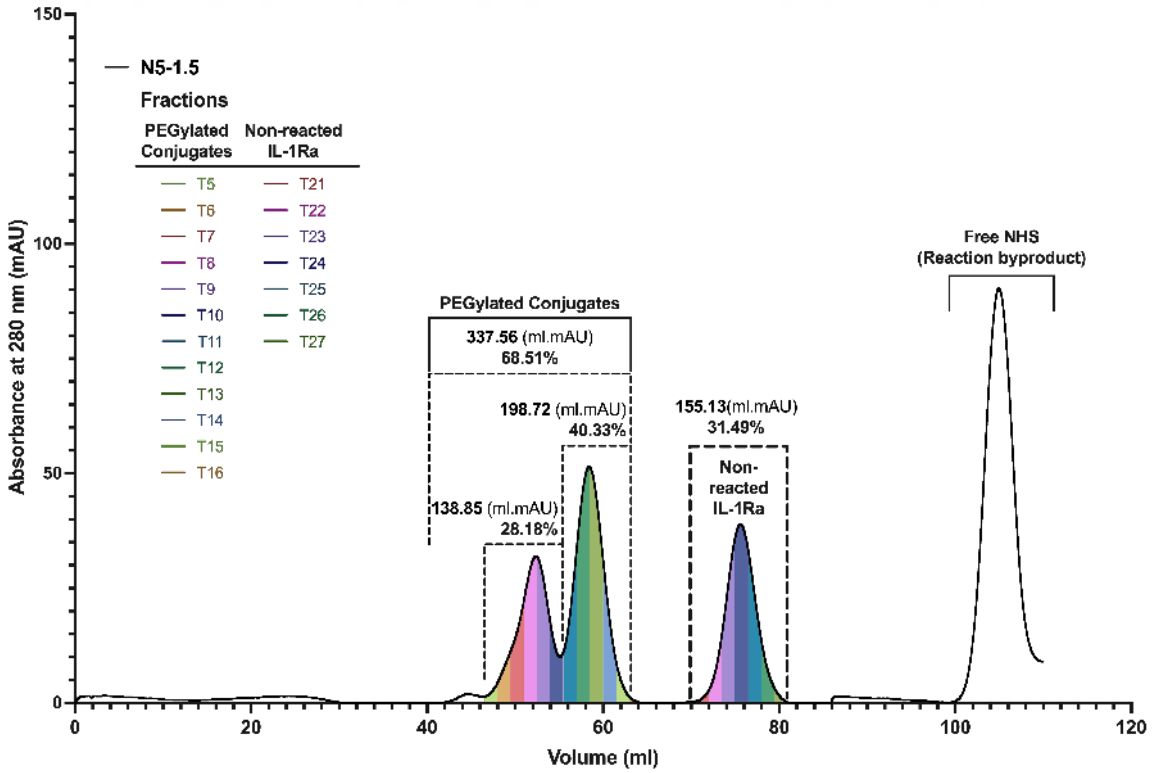

Figure 9.9: PEG:protein ratio screen at 3 : 2, for lysine-targeted PEGylation of IL-1Ra with 5 kDa mPEG-SVA.

The earlier two peaks correspond to high-order DoP PEGylated IL-1Ra conjugate; the later peak corresponds to the native protein. Colored overlays indicate collected fractions used for downstream analyses.

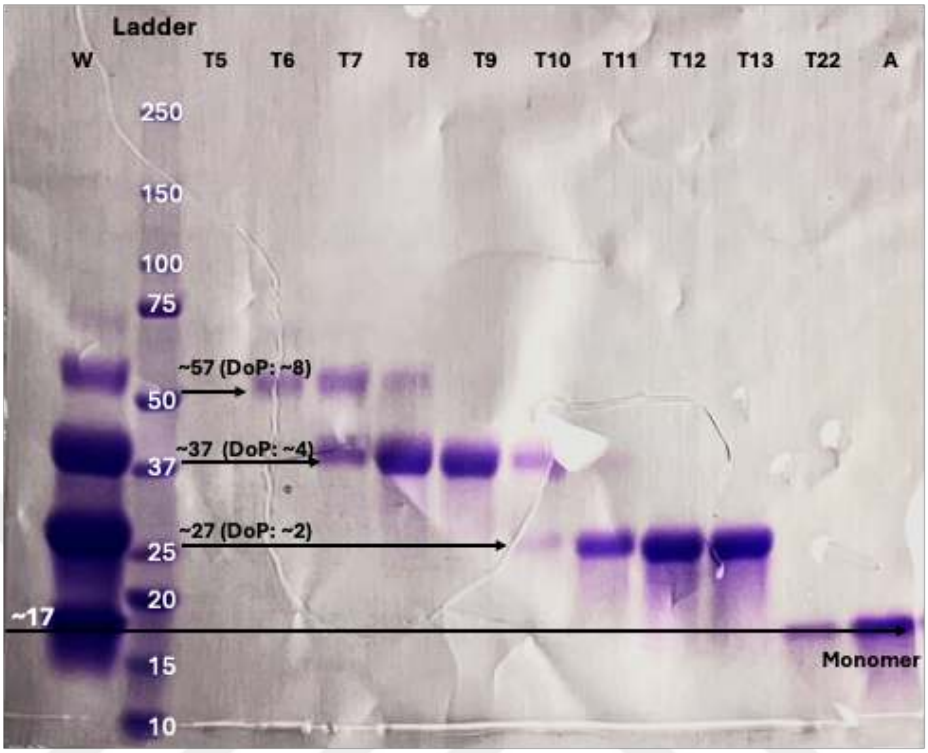

Figure 9.10: SDS–PAGE of N5-1.5

Fractions of T5-T10 yield a highly heterogeneous population of conjugates with high DoPs. T11-13 containing a more homogeneous population of conjugates with lower DoPs. T22 comprises an unconjugated native protein.

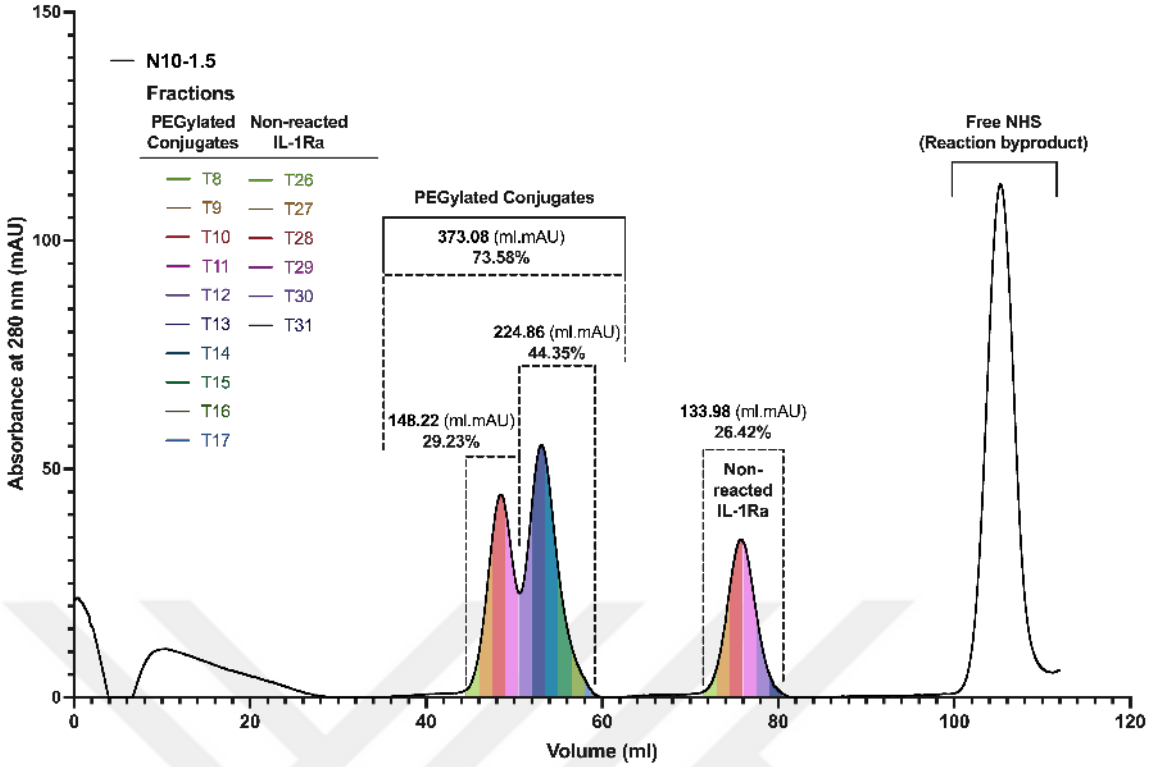

Figure 9.11: PEG:protein ratio screen at 3 : 2, for lysine-targeted PEGylation of IL-1Ra with 10 kDa mPEG-SVA.

The earlier two peaks correspond to high-order DoP PEGylated IL-1Ra conjugate; the later peak corresponds to the native protein. Colored overlays indicate collected fractions used for downstream analyses.

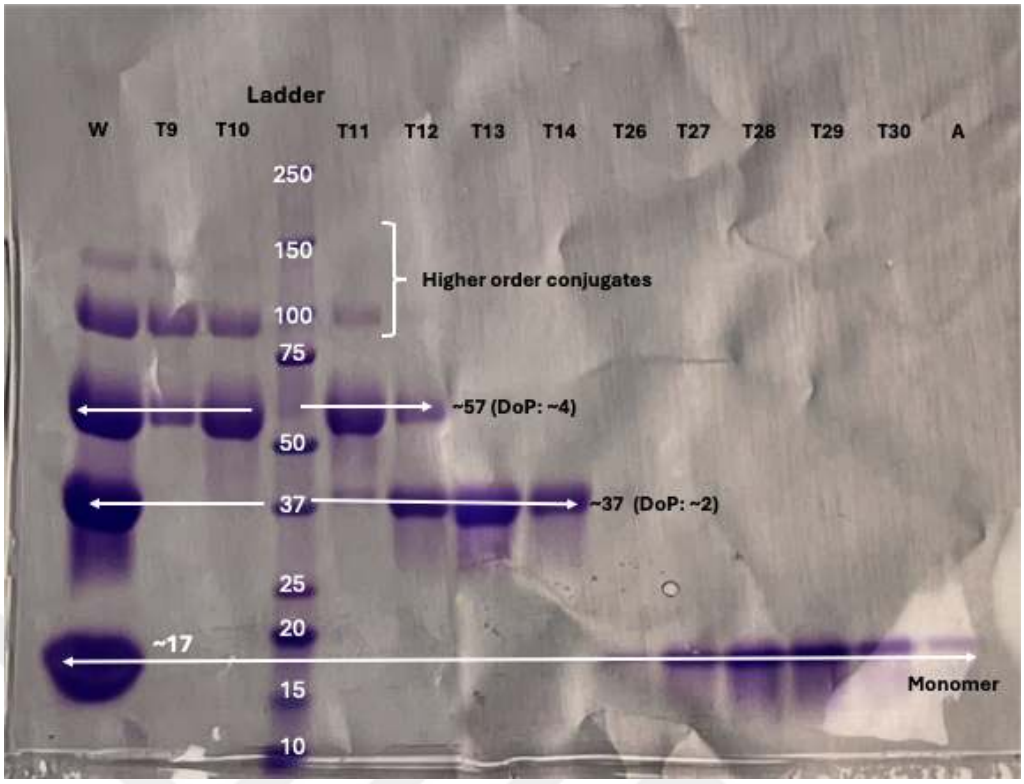

Figure 9.12: SDS–PAGE of N10-1.5

Fractions of T9-T12 yields a highly heterogeneous population of conjugates with high DoPs. T13-T14 contains a more homogeneous population of conjugates with lower DoPs. T26-30 comprises an unconjugated native protein.

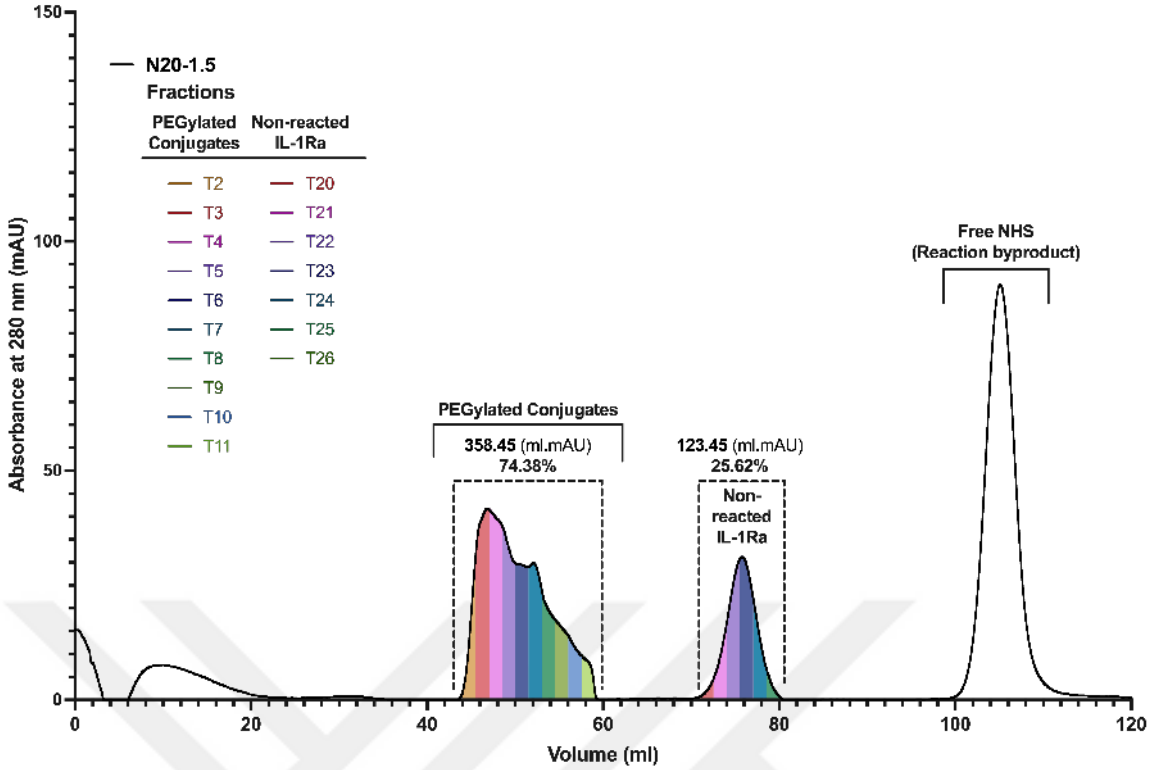

Figure 9.13: PEG:protein ratio screen at 3 : 2, for lysine-targeted PEGylation of IL-1Ra with 20 kDa mPEG-SVA.

The earlier, broad peak corresponds to a mixture of high-order DoP PEGylated IL-1Ra conjugates; the later peak corresponds to the native protein. Colored overlays indicate collected fractions used for downstream analyses.

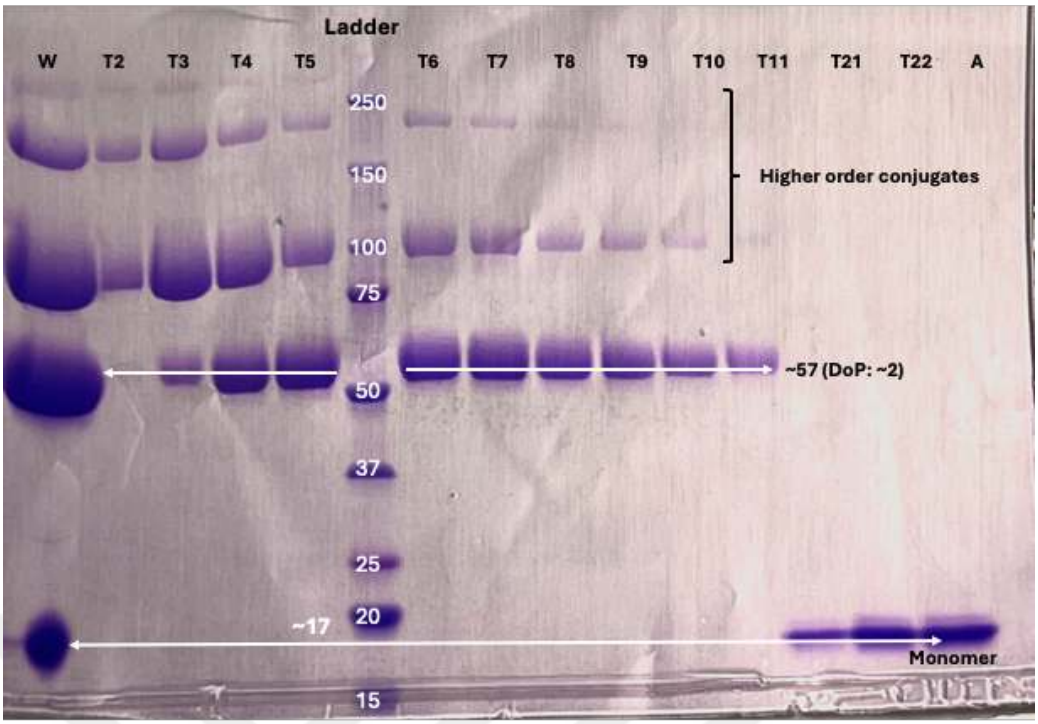

Figure 9.14: SDS–PAGE of N20-1.5

Fractions of T2-T11 yield a highly heterogeneous population of conjugates with high DoPs. T21-22 comprising unconjugated native protein.

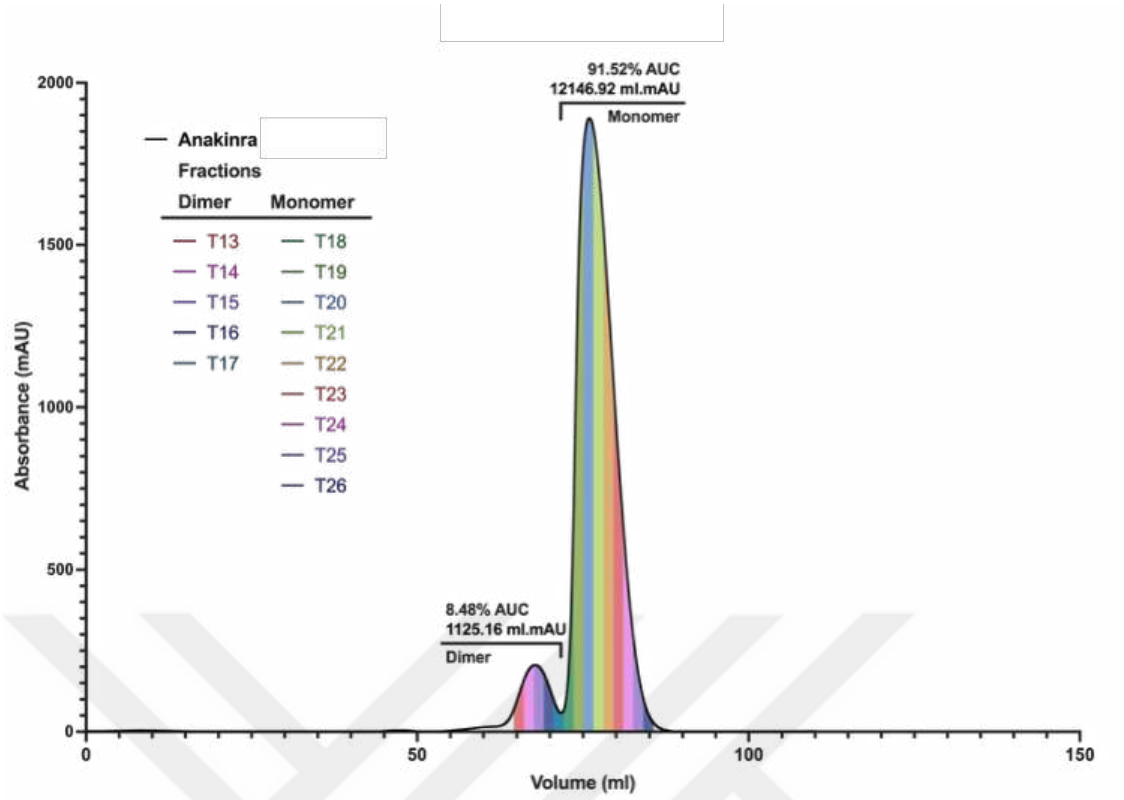

Figure 9.15: SEC of Anakinra to be used as a reference for its PEGylated counterparts.

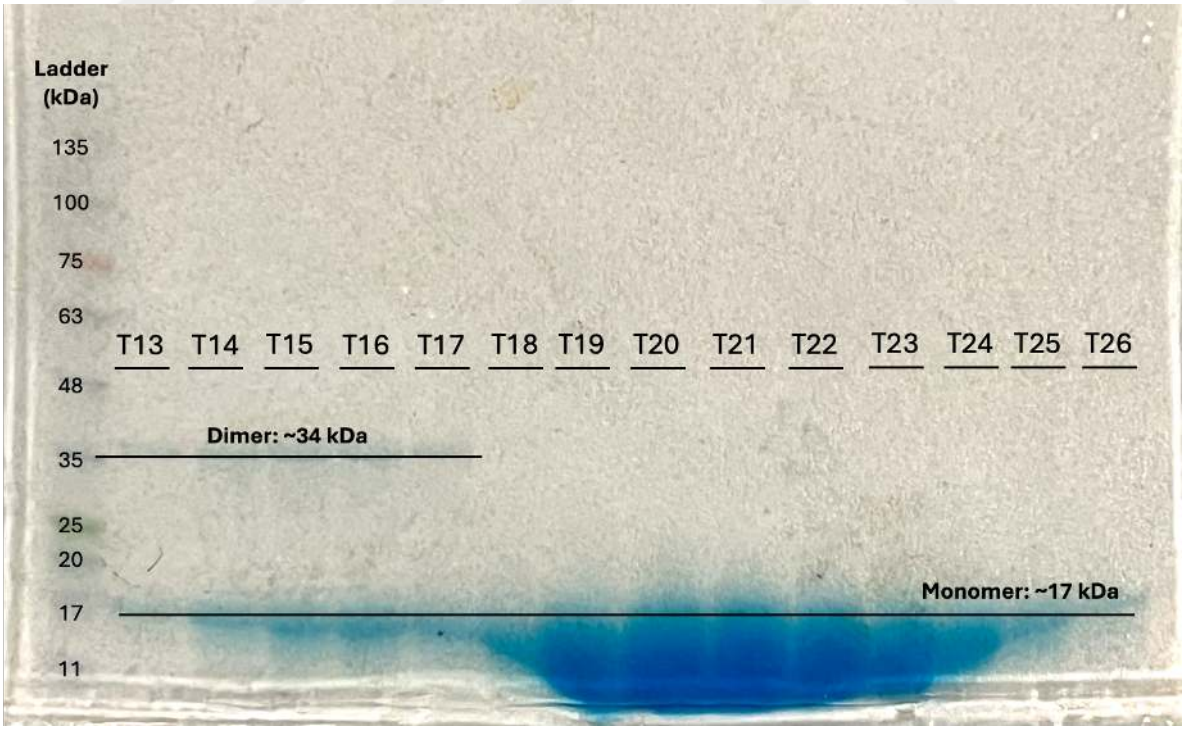

Figure 9.16: All fractions correspond to the native state of the protein at ~17 kDa.

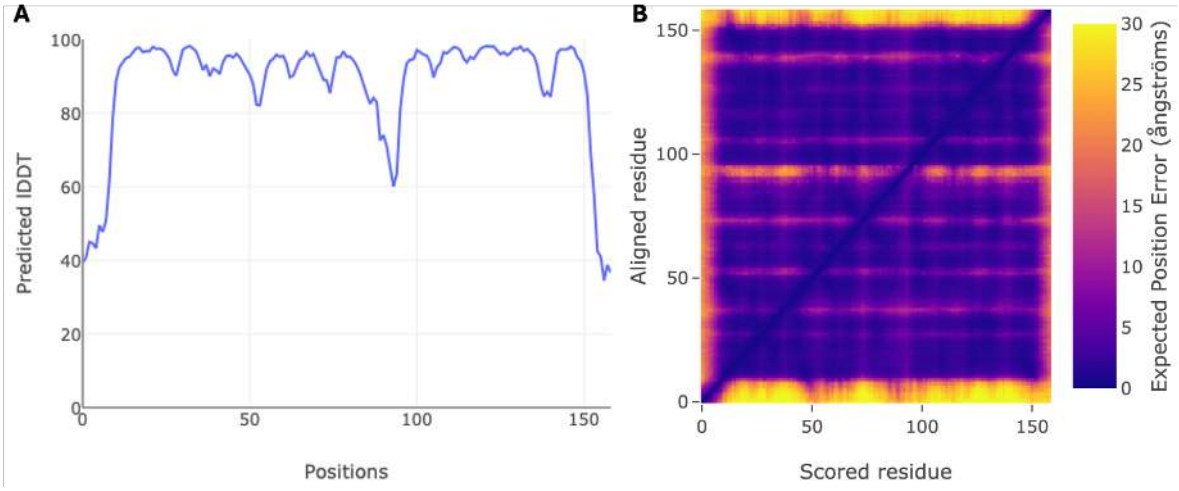

Figure 9.17: AlphaFold2 confidence metrics for M143V-IL-1Ra structural model.

(**A**) Predicted Local Distance Difference Test (pLDDT) values plotted across the residue sequence. Most regions scored above 90, indicating high model confidence.

(**B**) Predicted Aligned Error (PAE) heatmap for the full-length model. Low expected position errors (dark blue) dominate, suggesting well-defined inter-residue spatial relationships across the structure.

9.1. Appendix X: Python Code

```
!pip install openpyxl

import pandas as pd
import numpy as np

# Loading the raw full input files
paper_df_raw = pd.read_excel('/content/Paper-Raw-Data-2DNMR.xlsx')
exp_df_raw = pd.read_excel('/content/t10-m143v.xlsx')

# Removing rows with missing chemical shift values
paper_df = paper_df_raw.dropna(subset=['HN', '15N']).copy()
exp_df = exp_df_raw.dropna(subset=['HN', '15N']).copy()

# Distance function (weighted for 2D NMR)
def calc_distance(h1, n1, h2, n2, h_weight=5, n_weight=1):
    return np.sqrt(((h1 - h2)*h_weight)**2 + ((n1 -
n2)*n_weight)**2)

# Step 1: Closest experimental peak for each residue
def best_exp_for_residue(paper_df, exp_df):
    result = {}
    for _, row in paper_df.iterrows():
        res, h1, n1 = row['Residue'], row['HN'], row['15N']
```

```
        distances = exp_df.apply(lambda e: calc_distance(h1, n1,
e['HN'], e['15N']), axis=1)
        if distances.isnull().all(): continue
        idx = distances.idxmin()
        result[res] = {
            'Residue': res,
            'Ref_HN': h1,
            'Ref_15N': n1,
            'Exp_Index': idx,
            'Exp_HN': exp_df.loc[idx, 'HN'],
            'Exp_15N': exp_df.loc[idx, '15N'],
            'Distance': round(distances[idx], 2)
        }
    return result

# Step 2: Closest residue for each experimental peak
def best_residue_for_exp(exp_df, paper_df):
    result = {}
    for idx, row in exp_df.iterrows():
        h1, n1 = row['HN'], row['15N']
        distances = paper_df.apply(lambda r: calc_distance(h1, n1,
r['HN'], r['15N']), axis=1)
        if distances.isnull().all(): continue
        min_idx = distances.idxmin()
        result[idx] = {
            'Exp_Index': idx,
            'Exp_HN': h1,
            'Exp_15N': n1,
            'Residue': paper_df.loc[min_idx, 'Residue'],
            'Ref_HN': paper_df.loc[min_idx, 'HN'],
            'Ref_15N': paper_df.loc[min_idx, '15N'],
            'Distance': round(distances[min_idx], 2)
        }
    return result

# Step 3: Getting mutual matches only (both directions must agree)
def get_mutual_matches(paper_df, exp_df, tolerance=8.0):
    best_res2exp = best_exp_for_residue(paper_df, exp_df)
    best_exp2res = best_residue_for_exp(exp_df, paper_df)

    mutuals = []
    matched_residues = set()
    matched_exp_indices = set()

    for res, res_data in best_res2exp.items():
        exp_idx = res_data['Exp_Index']
        if exp_idx in best_exp2res:
            exp_data = best_exp2res[exp_idx]
```

```
            if exp_data['Residue'] == res and res_data['Distance']
<= tolerance:
                mutuals.append({
                    'Residue': res,
                    'Ref_HN': res_data['Ref_HN'],
                    'Ref_15N': res_data['Ref_15N'],
                    'Exp_HN': res_data['Exp_HN'],
                    'Exp_15N': res_data['Exp_15N'],
                    'Distance': res_data['Distance']
                })
                matched_residues.add(res)
                matched_exp_indices.add(exp_idx)

    return pd.DataFrame(mutuals), matched_residues,
matched_exp_indices

# Main loop: Repeating mutual matching in tiers until none remain
tier = 1
while True:
    mutual_df, matched_residues, matched_exp_indices =
get_mutual_matches(paper_df, exp_df, tolerance=8.0)

    if mutual_df.empty:
        print(f"No more mutual matches found at Tier {tier}.")
        break

    # Saving tier as CSV
    output_path = f"/content/MutualMatches_Tier_new{tier}.csv"
    mutual_df.to_csv(output_path, index=False)
    print(f"Tier {tier}: {len(mutual_df)} matches saved to
{output_path}")

    # Excluding matched entries for next round
    paper_df =
paper_df[~paper_df['Residue'].isin(matched_residues)].reset_index(d
rop=True)
    exp_df =
exp_df.drop(index=matched_exp_indices).reset_index(drop=True)

    tier += 1
```